Accurate Characterization of

Power Distribution Networks with Differential S-Parameters

A Thesis

Presented in Partial Fulfillment of the Requirements for the

Degree of Master of Science

with a

Major in Electrical Engineering

in the

College of Graduate Studies

University of Idaho

by

Hung Huy Tran

Major Professor: Lyudmyla Barannyk, Ph.D.

Co-major Professor: Mohsen Guizani, Ph.D.

Committee Members: Aicha Elshabini, Ph.D. and Fred Barlow, Ph.D.

Department Chair: Mohsen Guizani, Ph.D.

July 2015

Authorization to Submit Thesis

This thesis by Hung Huy Tran, submitted for the degree of Master of Science with a major in Electrical Engineering and titled "Accurate Characterization of Power Distribution Networks with Differential S-parameters", has been reviewed in final form. Permission, as indicated by the signatures and dates given below, is now granted to submit final copies to the College of Graduate Studies for approval.

Major Professor _____ Date _____

Lyudmyla Barannyk, Ph.D.

Co-major Professor _____ Date _____

Mohsen Guizani, Ph.D.

Committee

Members _____ Date _____

Aicha Elshabini, Ph.D.

_____ Date _____

Fred Barlow III, Ph.D.

Department

Chair _____ Date _____

Mohsen Guizani, Ph.D.

Abstract

Differential signaling is an important technique for low voltage high-speed digital systems to avoid electromagnetic interference. Differential networks are characterized using mixed-mode S-parameters that are typically obtained by conversion from single-ended S-parameters. We consider two test cases of broadside coupled striplines and edge coupled microstrips. We find that when strong coupling is present, the conversion matrix may be highly ill-conditioned, which affects accuracy of converted mixed-mode S-parameters.

We study causality preservation during conversion employing a causal Fourier continuation method. We extend the method to extract time delay by incorporating a linearly varying phase factor. The method is applicable to both single-ended and mixed-mode S-parameters.

We also develop a new approach for direct simulation of differential S-parameters using true excitations and apply it to characterize power distribution networks, whose electric behavior is not represented well by single-ended S-parameters due to ground bounce and a voltage drop across the network.

Acknowledgments

My graduate education and experience has been greatly enhanced through my association with many faculty and staff of different departments, for which I am truly grateful. Most specifically I would like to thank my major professor Lyudmyla Barannyk, my co-major professor Mohsen Guizani, my thesis committee members professor Aicha Elshabini, and professor Fred Barlow. Others critical in the advancement of my education and research include Sharmin Islam and Pin-Jen Wang. I would also like to thank Micron Technology, Inc. for providing the funding for this research. I am very grateful for the support, experience and opportunities I have been given by the University of Idaho and its community of faculty, staff and students.

To my family and friends, without you this work would not have been possible. Thank you for your support, past, present and future.

Table of Contents

List of Tables

List of Figures

1 Introduction

1.1 History of Electronic Packaging and DRAM

Unlike other science technology, it is hard to determine exactly the date when electronic packaging began to be engineering. Nevertheless, along with the discovery of the transistor in the 1940s, microelectronics packaging became so important and continued to grow to serve the evolution of the IC I/O counts and performance. The first transistors were packaged in plastic and were provided with little prevention from the outside environment. Until the need for military applications required higher hermeticity, those transistors were contained in a gold-plated metal base and had external leads, or headers. Their metal lids are sealed with the headers using welding. The processes are carried out in an inert atmosphere like nitrogen or argon, to provide a good isolation for electronic devices from the outside contamination.

Years later, ICs were fabricated with higher and higher number of I/Os, forcing electronic packing to be able to accommodate the need for higher pins counts. However, electronic packaging technology also set a certain standard for IC designers to adapt their new designs to a suitable package design. So we can see how electronic packaging and IC design interact with each other. Packaging has to be adequate to IC design, and IC design has to follow the existence and evolution of electronic packaging. As a result, in 1960s, people saw a numerous profiles of IC packages which have been developed rapidly. However, packaging is taken into account as a certain percentage of IC production cost. Relatively expensive packaging technology cannot be applied for simple, uninnovative, or

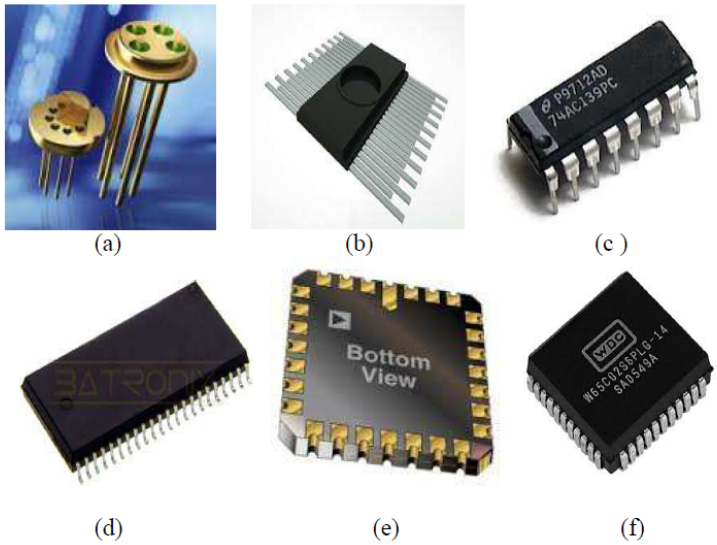

Figure 1: Early electronic packages models

(a) Transistor Outline, (b) Metal Flatpack, (c) Plastic Dual-in-line Package, (d) Small Outline Package, (e) Ceramic chip carrier, and (f) Plastic chip carrier

unpopular ICs. Also, there were also a lack of standards for package design and the need for higher density PWBs assembly. At the end of 1960s, only flatpack (Figure1b) and dual-in-line (DIP) (Figure 1c) packages could survive because PWB was very popular. Flatpack and DIP packages served well in the way that they can be mounted on PWB. At that time, plated through-hole and wave soldering techniques have been developed widely and made the DIP and flatpack packages popular.

Later, assembly market also saw the appearance of ceramic DIP which used low-melting-temperature glass. That kind of glass exhibited moisture outgasing property and later was replaced by vitreous glass which proved more reliability at a certain tolerance level. Low-cost plastic packaging is also a dominant choice for microelectronic

industry. Low hermeticity, poor adhesion to metal headers, and by-products of the plastics needed an improvement in encapsulation and plastic material which were resolved later. In 1970s, and 1980s, surface-mount-technology (SMT) made small-out-line package developed (Figure 2d). Chip carriers (Figure 2e, 2f and quadpacks (Figure 2a) were also developed in ceramic and plastic bodies with a close conformation to the size of the ICs contained in them. The quadpack usually had approximately 300 I/Os [3, 4]. In early 1990s, the quad flatpacks are replaced by Pin Grid Array and Ball Grid Array as shown from Figure 2b through 2f to satisfy the need for minimizing the circuit path length. I/O density of those PGA and BGA packages are very high as more than 250 pins. Of course, the cost for constructing those packages is also expensive. The BGA packaging techniques emerged from the flip-chip technology, referred to the controlled-collapse chip connect (C4), invented by IBM for ICs [5, 6]. The BGA packages are identified by the package bottom containing solder bumps. Solder bumps of BGA packages can be arranged by full array, multi-row perimeter, or staggered arrangement. Typical I/O counts for BGA package are usually 400, 736, or 625. Maximum counts can reach to more than 2000. The solder bumps are usually made of tin-lead or tin-lead-silver compounds. There are also some concerns associated with the BGA packages as follows: The solder joint defects, warpage during reflow process, ball size variation, inability to visually inspect solder joint, reduced resistance to thermal cycling, and rework problems are typical issues of BGA packages. However, those problems can be overcome if ICs producers have good designs, technology, and process enhancement.

Historically, there has been always a trend to pack more electronic functionality and

better performance into smaller volume of space. Packaging is a very important area of reducing size and increase the performance by eliminating the package or reducing the unnecessary points. In the late 1990s, chip-scale-package (CSP), which employed the BGA concept to reduce the terminal pitch to less than 1.0 mm for any mounting density greater than 100 pins/cm^2. Cellular phone was one of the applications that inherit the achievements of CSP about size reduction, weight, and performance at that time. Microball grid array, miniball grid array, and micro SMT packages which have less than 1.2 times the bare die size, employ direct surface mounting. CSPs are designed for the cases when flip chip are mounted using particular equipment and solder flow is required. CSPs not only offer an ease of the attribute of flip chips in a mountable package, it also provides an easy method for full functional and reliability testing of ICs. Thus, the designs of ICs and packaging always have a close relationship. The 1980s were the turning point of using electronic packaging.

From that important period of time, the reconsideration of electronic packaging had given the birth to Multichip modules (MCMs) as shown in Figure 3a. Although manufacturing hybrid circuits is not a new idea, the packaging technology which provides a mounting of a multiple number of ICs in a single package, had become an industry effort to push the electronic systems performance to higher levels. The fundamental intent of MCM technology is to provide the highest density of conductor matrix as possible for the interconnection of bare IC dies. As a result, the companies who designed their MCM products and others dropped the MCM for Multichip packages (MCP) (Figure 3b).

MCM, a viable technology today, played a major role in the evolution of multichip

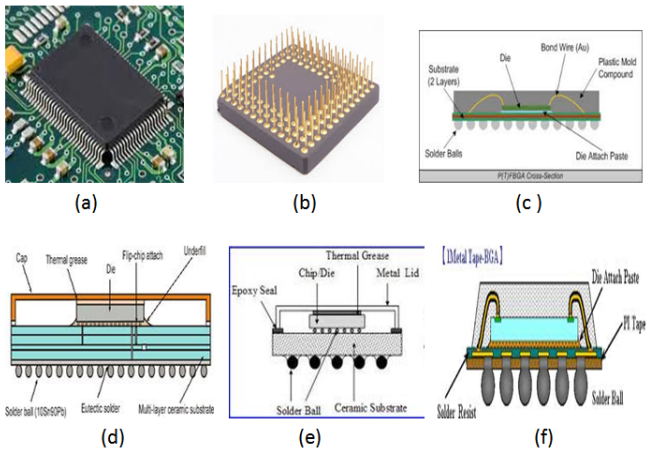

Figure 2: Recent microelectronics packages

(a) Quad Flatpack, (b) Pin Grid Array (PGA), (c) Plastic Ball Grid Array (BGA), (d) Ceramic BGA, (e) Ceramic Column Grid Array, and (f) Tape BGA

packaging in the 1990s, which includes three-dimensional (3D) stacking of ICs within a single package. Although chips can be stacked physically without connecting them to each other to save board space, present development efforts focus on interconnected, stacked chips. One of the first commercial efforts to stack chips within a single package mated flash memory with SRAM. In general, one can view multichip packaging as putting few ICs on a laminated substrate in a BGA package with the same appearance of a single-chip package. As electronic industries trying to reduce the product size, weight, and cost while extra performance also included, chip stacking may be the proper choice when high performance ICs are available in bare die form. However, chip stacking has created the need to thinning down chips to tens of micron in order to allow them to be placed in a conventional package. This packaging approach has been used as an

alternative to System-on-chip (SOC). The result is a System on package (SOP) or system in package (SIP). Chip thinning is not always positive. It can create new challenges due to the thinning process. These include induced stresses, microcracking, and the creation of defects in the chips. Furthermore, dicing and handling very thin chips during assembly can cause problems besides thermal issues, and higher cost for the system. Any approach to package stacking results in silicon efficiencies more than 100% . Package stacking (Figure 3c) is straightforward and is preferable when chips require burn-in. One mainly needs to develop techniques for connecting the packages together mechanically and electrically. This can be accomplished by simply soldering the leads of the packages together, or by use of an interposer. Package stacking has the advantages of using existing technology, it can have a CSP footprint, and it allows reasonably easy integration of different processes and materials. The most difficult issue of package stacking is the height of the finished package.

As both IC design and packaging technology progress, people need to address all of the critical problems associated with them. Such problems typically include moisture absorption, dielectric loss, warpage, limited interconnect dimensions, etc. Higher frequency system operation requires lower dielectric loss materials. Development of lower cost materials like ceramic, with lower processing temperatures must be developed and studied. For new materials, reliability issues need to be addressed as well. Finally, there is a new technology called Through-Silicon-Via (TSV) as shown in Figure 3d. In recent years, 3D integration exists in the form of wire-bonded flip-chip stacking which becomes dominant to overcome the limit of physical dimensional scaling [7, 8]. Many

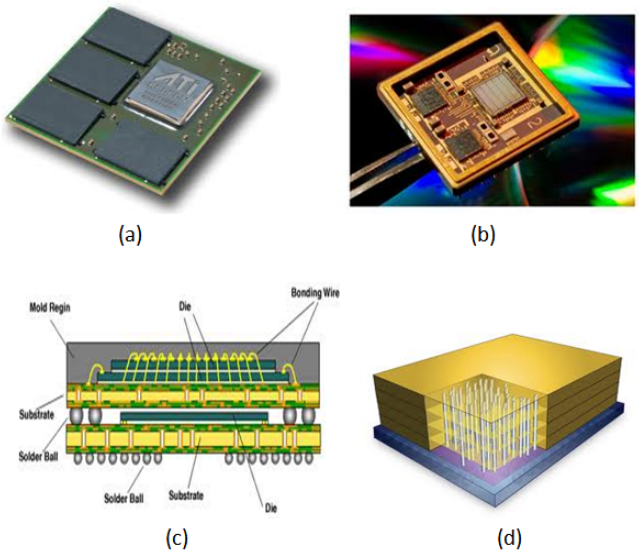

Figure 3: Multichip-module packages

(a) Multichip module (b) multichip package, (c) 3D package stacking, and (d) Through silicon vias (TSV) models.

research activities have been attempted on this topic. An example of achievements is an improved electrical behavior of coaxial vias, which provides better signal integrity than other conventional via structures [9]. Another achievement is a development of HF scalable electrical model for TSV which is verified with a 3-D field solver [10]. Today, TSV is an emerging method of wafer integration in 3-D space. IC designers will have more flexibility, greater energy and spatial economicity than traditional wire bonding or stacked flip chips. TSV is estimated to officially join the mainstream of IC fabrication industry in 2010, especially in the market of memory devices.

One can generally understand TSV as a process of vertically build up several chips and providing stable electrical and mechanical connection for them. TSV technology

provides high ratio between functionality and volume using recently developed micro fabrication methods. In TSV models, two or even more vertically stacked dies are joined together by vertical interconnection running from the bottom die to the top die. TSV has brought many attractive advantages such as shorter interconnects among dies, transfer power consumption reduction caused by wire bonding, and space efficiency. TSV technique also limits parasitic effects in the ICs, increase switching speed. Furthermore, TSV technology also allows higher I/O density of ICs. Memory manufacturers can implement TSV integration to make stacked DRAM chips to raise the memory total capacity and reduce PC board costs. Memory-processor latency will be sufficiently reduced and bandwidth will be extended. Later generations of cell phones will probably include image sensors or communication chips packaged with DSP and high capacity memory. Sub-components will be provided with faster data communication. Image sensors are now the most immediately desired application of TSV.

In TSV applications, the process sequence differs from traditional steps of wafer processing as it depends on the approach. Two typical approaches are the via-first and via-last approach. In those approaches, processing steps such as bonding, thinning, and subsequent de-bonding are performed on the TSV stack. The typical thickness ranges from 30 to 125 microns for thinned wafers which are bonded to class or dummy carriers. This will create new producing challenges. One typical issue is how to control the thermal budget. To achieve the integrity of adhesion of the bonding material used for wafers when bonded, operating temperature is not allowed to exceed 200Â°C. Another challenge is the requirement for new automatic test vehicles which are compatible with 3D ICs to

verify both mechanical and electrical functionalities of the final completed devices. Chip stacking categories can be divided into die-to-die or die-to-wafer, or even two completed wafers to be stacked together. If the high yielding wafers can be produced, the wafer-to-wafer stacking will be carried out to get a higher effectiveness. But for the early mainstream applications, it should be recommended to have die-to-wafer integration. In that approach, a single Known Good Die (KGD) is stacked onto other KGDs on a wafer.

TSV bring much benefit for chip manufacturing. However, there are also some challenges for implementing the TSV technology. The first one is the cost. Numerous aspects of design and producing will determine the implementation cost. Thus, TSV technology has to overcome that biggest barrier to get to the broad commercialization. More specific, the major cost barriers to TSV at the present are bonding, debonding, and via barrier/fill. When the production costs fit the roadmap, the value of TSV will be tremendous. Today, for example, smart phones have been successfully integrated with RF base chip, a flash memory, and an ARM microprocessor inside a plastic package with a reasonable cost of $12 to $17. Integration cost can even go well to under $5 if heterogeneous chip integration can be achieved. As estimated, a $30 cost increase compared to wire bonding, should be sufficient for TSV to get its return in functionality and performance. This is equivalent to a cost per wafer below $150 with 300 mm substrates, as an example. The second challenge for TSV technology is design. Because TSV is adopted for demanding complex applications that require a combination of different types of chips in a package such as RAM, processor, and RF base die, schematic and layout design guidelines must get along with the requirements for TSV technology.

Simulation software should also be able to address a variety of issues associated with the TSV stack design. Before the invention of TSV technology, chip architecture and layout are only suitable to the previous model of ICs design. But now, several thousand interconnections are presented between each couple of die. Thus, chip architecture and layout must be adapted such big changes.

1.2 Signal and Power Integrity

Some heterogeneous main modules such as mixed-signal ADC, OptoElectronic, analog RF links, CPU, DSP, MEM actuators, sensors, and resonators, Memory modules, and power electronics converters are usually integrated in future electronic systems. When such modules are assembled on a single SoP or SoC package, many convincing points of view have proved that compatibility-related problems have become more serious. In this work the physical electromagnetism viewpoint will be addressed. Both static and dynamic electromagnetic fields and propagation can be inevitably produced in electronic circuits. In addition, similar other fields could potentially cause malfunctions when presented in the operating environment of electronic circuits. Those phenomena are addressed by a more general term Electro-Magnetic Interference (EMI). The ultimate goal of electronic systems is ensuring their correct operation with respect to EMI phenomena. It is often called Electromagnetic Compatibility or EMC.

To maintain EMC, there is a need to find both the levels of electromagnetic field propagation from a device and the tolerence levels of other nearby devices. They should follow some standards to guarantee the operation of the system. Classical methodology

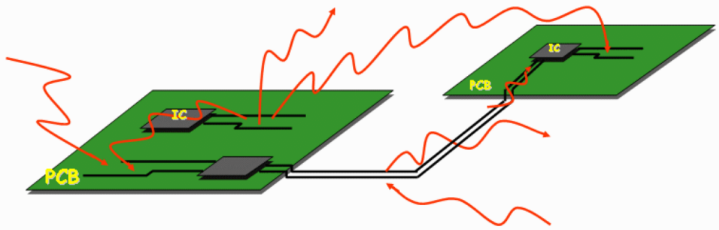

Arrows represent static and quasi-static EM fields. Their propagation which are produced by electronic circuits can result malfunction of adjacent electronic circuits.

Figure 4: Electro-Magnetic Interference (EMI)

of EMC required those levels should satisfies some predefined standards. EMI is traditionally classified as radiated and conducted, depending on the transmission method of the disturbances. Some EMI phenomena are demonstrated in Figure 4. Transmission of disturbances caused by conductors is referred as conducted interference which is induced into PDNs in power electronics, i.e. switching power supplies or electric motors. In the field of integrated circuits (ICs), conduction interference stands for substrate currents. It is also called current spikes induced into the PDN of the chip produced by switching activities of the digital gates. In a broader sense,conducted interference can be defined as capacitive cross-talk coupling which is short-distance interference of simple electric field or inductive coupling by a simple magnetic field. In order to analyze those phenomena, modeling by quasi-static circuit theory is sufficient. For instant, magnetic coupling between two adjacent pins of a package can be modeled as coupled inductors. Broad and long close conductors cross-talk due to coupling electric field can be modeled as capaci-

tors. In the literature, at the PCB level, researchers have extensively characterized and studied conducted interference. At this level, many controlling methods to mitigate its effects are known. For examples, in electric machinery and power electronics, filtering techniques have been employed to minimize such interference at the PDNs. On the contrary, at the level of ICs or IC packages, researchers have only addressed a few conducted interference problems. For example, ICs has been characterized with substrate noise, and the development of design guidelines to suppress the effects of cross-talk is evolving. Nevertheless, more research work, especially on conducted emissions of SSN onto the PDNs, is still needed.

Electromagnetic wave emission causes transmission disturbances, or radiated interference, which is a big concern. In this situation, we usually cannot ignore the distances between noise source and victim networks be cause at high frequencies, wavelengths are relatively short. Because of the interrelation of the electric and magnetic fields, modelling those types of emission with simple quasi-static circuits is not relevant. There is an unavailability of techniques to effectively and accurately analyze and model any type of electronic systems at any level (ICs, packages or even PCBs).

1.3 Main EMI problems for system design

To support the emerging design style described above, increasing attention needs to be devoted to ensure proper component encapsulation. Encapsulation is relative to a particular phenomenon of interest. While to support the emerging design style described above, increasing attention needs to be devoted to ensure proper component encapsu-

lation. Encapsulation is relative to a particular phenomenon of interest. While electric cross-talk, impedance matching, electro-migration have all been considered in a way, all other conducted and radiated EMI phenomena have not been properly addressed thus far. Since EMI emissions and susceptibility are of growing importance, as frequencies keep increasing in the GHz region, this encapsulation aspect needs to be addressed as well, in order to ensure the design quality and design time expected by this new SoC design style.

We further recognize that EMI problems are mainly due to two mechanisms: EMI emissions due to the components switching activity, and emissions and susceptibility of the communication wires interconnecting the components.

1.3.1 EMI emissions due to the switching activity of digital components

Most of the components used to assemble SoB, SoP or SoC, typically contain fast switching digital circuit blocks. Thousands to millions of gates may switch at the same time producing large spikes of currents in the power and ground connections of the block. Such currents are very-high-frequency conducted emissions that escape from the component, interfering the entire power and ground system. Flowing on the much longer wires of the power and ground grid, they can easily find favorable dimension-to-wavelength ratios and radiate. This phenomenon, depicted in Figure 4, can be responsible for the largest portion of EMI emissions.

1.3.2 Emissions and susceptibility of communication wires among system components

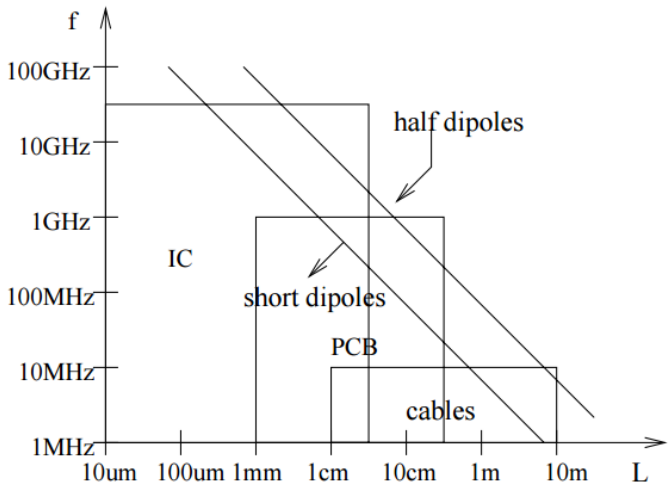

Figure 5: Typical harmonic contents and wire lengths on present and future electronic systems

Components are connected by wires to provide the necessary functionality. I/O communication wires represent a second very important issue, both for EMI emissions, and for susceptibility. Such wires carry high frequency communication signals between blocks and can be long compared to the wavelengths of the harmonics of the signals they carry. EMI emissions in this situation are very likely unless a close return path is provided.

Such wires can be very susceptible to radiation present in the environment, or coming from nearby systems. Incident electromagnetic fields can induce currents and voltages on such wires as shown in Figure 4. These are mixed with the signals on the wires, and

act as noise to the receiving input buffers. Severe and apparently inexplicable faults can result when this noise exceeds than the noise margins of the receiver.

1.4 Differential Signaling

Differential signaling is the use of two output drivers to transmit two independent transmission lines, one line carrying one bit and the other one carrying its complement. The measured signal is the difference between the two lines. With the increasing demand for high performance electronic devices, System on Package (SoP) has become popular. SoP is an essential step to not only replace the temporal System in Package (SiP) solution but also to join two levels of packaging together. This evolutionary step also brings many challenges in terms of noise suppression [11, 12]. The ultimate goal of designing package Power Distribution Networks (PDN) is to reduce the parasitics and increase the decoupling as much as possible [13]. The traditional method involves the optimization of capacitor selection and placement [14, 15, 16, 17, 18, 19]. Another solution is to use differential signaling.

Mixed-mode scattering parameters (S-parameters) were first introduced by Bockelman and Eisenstadt in 1995 [20]. In 1997 Bockelman continued his work and provided a conversion formula for mixed-mode S-parameters from single-ended S-parameters [21] for the case with no coupling. Although differential signaling is not a new concept any more, it is becoming more popular as the complexity of packages increases. A lot of research has been done on this topic including theoretical development, conversion from and to single-ended signaling, and simulation and measurement comparisons

[22, 23, 24, 25, 26]. All of them have taken into account the coupling between transmission lines that will give more accurate characterization of differential networks. Figure 4 in the work of [22] is a typical demonstration for the importance of the presence of coupling effect. In more details, the true differential S-parameters deviated significantly from themselves when coupling is not taken into account.

The conversion from single-ended to mixed mode S-parameters when coupling is present was introduced in [22]. It requires inversion of a transformation matrix that depends in turn on S-parameters. It is known that direct numerical inversion of a matrix may be unstable especially in the case when such matrix is ill-conditioned. If this is not taken into account, converted mixed-mode S-parameters may be highly inaccurate. In such cases, the direct numerical inversion should be avoided and regularized methods from the theory of ill-posed problems [27] should be used, for example, truncated singular value decomposition (SVD) method that would allow one to regularize the problem, and obtain accurate and reliable results.

Conversion from single-ended to mixed mode S-parameters is studied in Section 5.

1.5 Causality of High-Speed Interconnects

The design of high speed interconnects that are common on chip and at the package level in digital systems, requires systematic simulations at different levels in order to evaluate the overall electrical system performance and avoid signal and power integrity problems [12]. To conduct such simulations, one needs suitable models that capture the relevant electromagnetic phenomena that affect the signal and power quality. These models

are often obtained either from direct measurements or electromagnetic simulations in the form of discrete port frequency responses that represent scattering, impedance, or admittance transfer functions or transfer matrices in scalar or multidimensional cases, respectively. Once frequency responses are available, a corresponding macromodel can be derived using several techniques such as the Vector Fitting [28], the Orthonormal Vector Fitting [29], the Delay Extraction-Based Passive Macromodeling [30] among others. However, if the data are contaminated by errors, it may not be possible to derive a good model. These errors may be due to a noise, inadequate calibration techniques or imperfections of the test set-up in case of direct measurements or approximation errors due to the meshing techniques, discretization errors and errors due to finite precision arithmetic occurring in numerical simulations. Besides, these data are typically available over a finite frequency range as discrete sets with a limited number of samples. All this may affect the performance of the macromodeling algorithm resulting in non-convergence or inaccurate models. Often the underlying cause of such behavior is the lack of causality in a given set of frequency responses [31].

Causality can be characterized either in the time domain or the frequency domain. In the time domain, a system is said to be causal if the effect always follows the cause. This implies that a time domain impulse response function $h(t) = 0$ for $t < 0$, and a causality violation is stated if any nonzero value of $h(t)$ is found for some $t < 0$. To analyze causality, one can convert the frequency responses to the time domain using the inverse discrete Fourier transform. This approach suffers from the well known Gibbs phenomenon that is inherent for functions that are not smooth enough and represented

by a truncated Fourier series. Examples of such functions include impulse response functions of typical interconnects that have jump discontinuities and whose spectrum is truncated since the frequency response data are available only on a finite length frequency interval. Direct application of the inverse discrete Fourier transform to raw frequency response data causes severe over and under shooting near the singularities. This problem is usually addressed by windowing the Fourier data to deal with the slow decay of the Fourier spectrum [32, Ch. 7]. Windowing can also be applied in the Laplace domain [33] to respect causality. This approach is shown to be more accurate and efficient than the Fourier approach [34]. There are other filtering techniques that deal with the Gibbs phenomenon but they require some knowledge of location of singularities (see [35, 36, 37, 38] and references therein). A related paper [39] employs nonlinear extrapolation of Fourier data to avoid the Gibbs phenomenon and the use of windows/filtering.

In the frequency domain, a system is said to be causal if a frequency response given by the transfer function $H(w)$ satisfies the dispersion relations also known as Kramers-Krönig relations [40, 41]. The dispersion relations can be written using the Hilbert transform. They represent the fact that the real and imaginary parts of a causal function are related through Hilbert transform. The Hilbert transform may be expressed in both continuous and discrete forms and is widely used in circuit analysis, digital signal processing, remote sensing and image reconstruction [42, 32]. Applications in electronics include reconstruction [43] and correction [44] of measured data, delay extraction [45], interpolation/extrapolation of frequency responses [46], time-domain conversion [47], estimation of optimal bandwidth and data density using causality checking [48]

and causality enforcement techniques using generalized dispersion relations [49, 50, 51], causality enforcement using minimum phase and all-pass decomposition and delay extraction [52, 53, 54, 55], causality verification using minimum phase and all-pass decomposition that avoids Gibbs errors [56], causality characterization through analytic continuation for L_2 integrable functions [57], causality enforcement using periodic polynomial continuations [58, 59, 60, 61].

The Hilbert transform that relates the real and imaginary parts of a transfer function $H(w)$ is defined on the infinite domain which can be reduced to $[0, \infty)$ by symmetry properties of $H(w)$ for real impulse response functions. However, the frequency responses are usually available over a finite length frequency interval, so the infinite domain is either truncated or behavior of the function for large w is approximated. This is necessary since measurements can only be practically conducted over a finite frequency range and often the cost of the measurements scales in an exponential manner with respect to frequency. Likewise simulation tools have a limited bandwidth and there is a computational cost associated with each frequency data point that generally precludes very large bandwidths in these data sets. Usually $H(w)$ is assumed to be square integrable, which would require the function to decay at infinity. When a function does not decay at infinity or even grows, generalized dispersion relations with subtractions may be successfully used to reduce the dependence on high frequencies and allow a domain truncation [49, 50, 51]. A review of some previous work on generalized dispersion relations and other methods that address the problem of having finite frequency range is provided in [51].

In paper [61], an alternative approach was taken and instead of approximating the

behavior of $H(w)$ for large w or truncating the domain, a causal periodic continuation or causal Fourier continuation of $H(w)$ was constructed by requiring the transfer function to be periodic and causal in an extended domain of finite length. In [58, 59, 60], polynomial periodic continuations were used to make a transfer function periodic on an extended frequency interval. In these papers, the raw frequency responses were used on the original frequency interval. Once a periodic continuation is constructed, the spectrally accurate Fast Fourier Transform [62] implemented in FFT/IFFT routines can be used to compute discrete Hilbert transform and enforce causality. The accuracy of the method was shown to depend primarily on the degree of the polynomial, which implied the smoothness up to some order of the continuation at the end points of the given frequency domain. This in turn allowed to reduce the boundary artifacts compared to applying the discrete Hilbert transform directly to the data without any periodic continuation, which is implemented in the function `hilbert` from the popular software Matlab.

In [61], the idea of periodic continuations of an interconnect transfer function was implemented by approximating this function with a causal Fourier series in an extended domain. The approach allows one to obtain extremely accurate approximations of the given function on the original interval. The causality conditions are imposed exactly and directly on Fourier coefficients, so there is no need to compute Hilbert transform numerically. This eliminates the necessity of approximating the behavior of the transfer function at infinity similarly to a polynomial continuation technique employed in [58, 59, 60], and does not require the use of Fast Fourier Transform. The advantage of the method is that it is capable of detecting very small localized causality violations with

amplitude close to the machine precision, at the order of 10^{-13}, and a small uniform approximation error can be achieved on the entire original frequency interval, so it does not have boundary artifacts reported by using `hilbert` Matlab function, polynomial continuations [58, 59, 60] or generalized dispersion relations [49, 50, 51]. The performed error analysis unbiases an error due to approximation of a transfer function with a causal Fourier series from causality violations that are due to the presence of a noise or approximation errors in data. The developed estimates of upper bounds for these errors can be used in checking causality of the given data.

We use the SVD-based causal Fourier continuation [61] in this work in Section 6 to analyze loss of causality during the conversion from single-ended to mixed-mode S-parameters.

1.6 Time Delay Extraction

Identification and extraction of time delay is an important problem in signal processing and has applications in many areas such as radar, sonar, wireless communications, modeling of passive structures in an electronic system and, in particular, transmission line modeling [63], transient simulation of interconnects [64] and co-simulation of passive structures with active devices in time domain using SPICE. Passive interconnect structures in electronic systems have been traditionally analyzed in the frequency domain. As clock frequencies increase, the size of passive structures becomes of the same order as the signal wavelength at the operating frequency, which causes distributed effects such as time delay to play a significant role in the time domain simulations. For this

reason, time delay has to be included in macro-modeling, in particular, when causality is analyzed. The connection between causality and time delay is in the fact that time delays can pull a non-causal signal into the causal region or vice versa pull a causal signal into the non-causal region, while causality, in turn, can be expressed in terms of the Hilbert transform [65]. Several approaches can be used to extract delays in the frequency domain, for example, using the Hilbert transform [45], the minimum phase all-pass decomposition [64] or the cepstrum [66]. In the time domain, delayed rational functions [67] can be employed to extract delays. In this work, a novel approach is proposed in which time delay is determined in the frequency domain using a causality argument. Causality is verified in Section 8 using SVD-based Fourier continuation method [61, 60], while the time delay presence is incorporated by a linearly varying phase factor. Preliminary results [68] have been accepted for oral presentation at the 2015 IEEE 24th Conference on Electrical Performance of Electronic Packaging and Systems.

2 S-Parameters and Differential S-Parameters

2.1 Introduction and two-port network theory

All electromagnetic behaviors can ultimately be explained by 'Maxwell's' four basic equations. However, it is not always possible or convenient to use these equations directly. Solving them can be quite difficult. Efficient design requires the use of approximations such as lumped and distributed models.

Linear networks, or nonlinear networks operating with signals sufficiently small to cause the networks to respond in a linear manner, can be completely characterized by parameters measured at the network terminals (ports) without regard to the contents of the networks. Once the parameters of a network have been determined, its behavior in any external environment can be predicted, again without regard to the contents of the network.

We have known about conventional network parameters include Z-, Y-, and H-parameters. However, S-parameters are important in microwave design because they are easier to measure and work with at high frequencies than other kinds of parameters. They are conceptually simple, analytically convenient, and capable of providing a great insight into a measurement or design problem.

To show how s-parameters ease microwave design, and how one can best take advantage of their abilities, this application note describes s-parameters and flow graphs, and relates them to more familiar concepts such as transducer power gain and voltage gain. Data obtained with a network analyzer is used to illustrate amplifier design.

Although a network may have any number of ports, network parameters can be explained most easily by considering a network with only two ports, an input port and an output port, like the network shown in Figure 6. To characterize the performance of such a network, any of several parameter sets can be used, each of which has certain advantages. Each parameter set is related to a set of four variables associated with the two-port model. Two of these variables represent the excitation of the network (independent variables), and the remaining two represent the response of the network to the excitation (dependent variables). If the network of Figure 6 is excited by voltage sources V_1 and V_2, the network currents I_1 and I_2 will be related by the following equations (assuming the network behaves linearly):

$$I_1 = y_{11}V_1 + y_{12}V_2 \tag{1}$$

$$I_2 = y_{21}V_1 + y_{22}V_2 \tag{2}$$

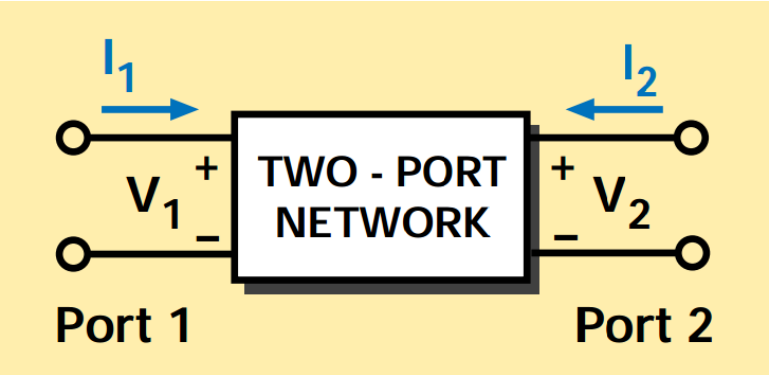

Figure 6: General two-port network

In this case, with port voltages selected as independent variables and port currents

taken as dependent variables, the relating parameters are called short-circuit admittance parameters, or y-parameters. In the absence of additional information, four measurements are required to determine the four parameters y_{11}, y_{12}, y_{21}, y_{22}. Each measurement is made with one port of the network excited by a voltage source while the other port is short circuited. For example, y_{21}, the forward transadmittance, is the ratio of the current at port 2 to the voltage at port 1 with port 2 short circuited, as shown in equation 3.

$$y_{21} = \frac{I_2}{V_1} \tag{3}$$

when V_2=0 (output short circuited)

Two-port, three-port, and n-port models simplify the input / output response of active and passive devices and circuits into “black boxes" described by a set of four linear parameters. Lumped models use representations such as Y (conductances), Z (resistances), and h (a mixture of conductances and resistances). Distributed models use s-parameters (transmission and reflection coefficients).

If other independent and dependent variables have been chosen, the network would have been described, as before, by two linear equations similar to equations 1 and 2, except that the variables and the parameters describing their relationships would be different. However, all parameter sets contain the same information about a network, and it is always possible to calculate any set in terms of any other set. “Scattering parameters " , which are commonly referred to as s-parameters, are a parameter set that relates to the traveling waves that are scattered or reflected when an n-port network is

inserted into a transmission line.

2.2 Using S-parameters

The ease with which scattering parameters can be measured makes them especially well suited for describing transistors and other active devices. Measuring most other parameters calls for the input and output of the device to be successively opened and short circuited. This can be hard to do, especially at RF frequencies where lead inductance and capacitance make short and open circuits difficult to obtain. At higher frequencies these measurements typically require tuning stubs, separately adjusted at each measurement frequency, to reflect short or open circuit conditions to the device terminals. Not only is this inconvenient and tedious, but a tuning stub shunting the input or output may cause a transistor to oscillate, making the measurement invalid.

S-parameters, on the other hand, are usually measured with the device imbedded between a 50 Ω load and source, and there is very little chance for oscillations to occur.

Another important advantage of s-parameters stems from the fact that traveling waves, unlike terminal voltages and currents, do not vary in magnitude at points along a lossless transmission line. This means that scattering parameters can be measured on a device located at some distance from the measurement transducers, provided that the measuring device and the transducers are connected by low-loss transmission lines.

2.3 Derivation

Generalized scattering parameters have been defined by [69]. These parameters describe the interrelationships of a new set of variables (a_i ,b_i). The variables a_i and b_i are normalized complex voltage waves incident on and reflected from the i^{th} port of the network. They are defined in terms of the terminal voltage V_i , the terminal current I_i , and an arbitrary reference impedance Z_i , where the asterisk denotes the complex conjugate:

$$a_i = \frac{V_i + Z_i I_i}{2\sqrt{|ReZ_i|}} \tag{4}$$

$$b_i = \frac{V_i - Z_i^* I_i}{2\sqrt{|ReZ_i|}} \tag{5}$$

For most measurements and calculations it is convenient to assume that the reference impedance Zi is positive and real. For the remainder of this article, then, all variables and parameters will be referenced to a single positive real impedance, Z_0. The wave functions used to define S-parameters for a two-port network are shown in Figure 7

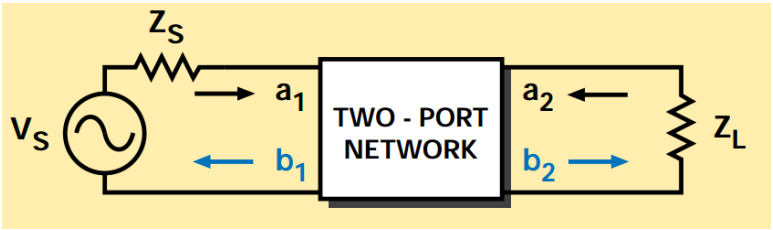

Figure 7: Two-port network showing incident waves (a_1, a_2) and reflected waves (b_1,b_2) used in S-parameter definitions

3 Finite Element Electromagnetic Simulation

3.1 Electronic Design Automation (EDA) software overview

Electronic design automation (EDA) software is classified as computer-aided tools used for electronic system designs. Two basic electronic system levels are printed circuit boards (PCBs) and integrated circuits (ICs). They usually include important design stages in a designing flow such as drawing layout, rule checking, and analyzing systems or subsystems.

Prior to EDA software, ICs were manually designed and laid out by hand. Temporal advanced techniques employed geometric software to extract Gerber images, but some components still need to be drawn mechanically. Because this process involves graphics and electronics is manually translated to graphics, a very few companies during this era can survive with their GDSII format. The best known company in this area is Calma. In the 1970s, the design was automated with the drafting by developers. This is marked by the first place-and-route software tools and the proceedings of conferences about Design Automation.

In 1980, the next era of this area was marked with the publication of [70]. This invention had translated IC design ideas into a programming language, making a significant increase of chip design complexity. Logic simulation played the key role in verification which is necessary prior to fabrication. As a result, chips layout were easier to be drawn and function as well as expected from complete simulations. The programming languages and tools can be changed, but the core physical basis still remains to be the

backbone of IC design in the recent years.

One of the most famous and earliest EDA tools was “Berkeley VLSI Tools Tarball" which was produced in academia for early VLSI systems. The next essential development was the tool which allowed an effective way to train student IC designers to produce real ICs. Its name was MOSIS. 1981 to 1984 were the years marking the dawn of EDA industry. In this era, big firms such as Intel, Tektronix, and Hewlett Packard, have immanently developed EDA. EDA turned out to be a big business with the foundation of Valid Logic System, Mentor Graphics, and Daisy Systems, then later were referred as DMV. EDA was such a big area that many companies specialized in many different emphasis during a short time. In 1984, Design Automation Conference was the very first commercial show of EDA industry. Also in this era, the U.S. Department of Defense started financing VHDL as a hardware description language. In 1986, Gateway Design Automation introduced Verilog as another popular high-level hardware discription language followed by simulators which together allowed direct simulations of IC designs.

The continuous scaling of silicon industry have increased the importance of EDA software for electronic engineering. Some used them for foundries of fabrication facilities, or provided evaluation services for incoming manufacturing design readiness. They are also used for functionality programming into FPGAs kits.

EDA Design flow from top to bottom includes High-level synthesis (also called behavioural synthesis or algorithmic synthesis) - and C++ high-level design description conversion to RTL, translation from RTL (Verilog or VHDL) to Logic synthesis with netlist of logic gates, Schematic Capture (i.e., Cadence Orcad or Proteus ISIS) for RF,

analog, or standard digital cells, and finally Layouting (i.e., Cadence Allegro or Proteus ARES).

Simulation flow includes different techniques that yield different accuracies and consume different amounts of time for trade-offs: transistor or linear simulation is a low-level simulator for behavior of schematics or layouts, with device-level accuracy, logic or simulation for RTLs and gate-netlist's digital (true/false) behavior of boolean level, behavioral simulation for architectural operation at high level with interface-level accuracy, hardware emulation which employs specific hardware to verify proposed design logic, called in-circuit emulation, CAD technology simulator to analyze the essential process technology in which device characteristics are verified directly from device physics, and finally electromagnetic field solvers which generate numerical solutions of Maxwell's equations applied for any interest of IC and PCB models. EM field solvers are the most accurate simulators but also the most time consuming. This research work focuses on utilizing the advantages of EM field solver using ANSYS^{TM} HFSS for characterization of electronic systems. Although the main disadvantage of EM field solvers is they are expensive to run, this difficulty can be overcome by separating the systems into multiple subsystems, then simulating each system level and cascading the S-parameters of each submodels. The more detailed discussion will be given in the following sections.

Beside the above design procedures, there are also EDA features that can offer users with functioning-focus verification and manufacturing preparation. Functional verification includes Clock Domain Crossing Verification, or CDC check, which is very similar to linting, but focuses on detecting and making aware of potential data loss due to multiple

clocking domain, formal verification or model checking, equivalence checking, static timing analysis, and physical verification. Manufacturing preparation includes Mask Data Preparation, Resolution Enhancement Techniques, Optical Proximity Correction, Mask Generation, Automatic test pattern generation, and built-in self-test.

3.2 Common Analysis Tools

For Signal and Power Integrity (SI/PI) and EMI/EMC simulation, although there are some methods such as Method of Moments, Cavity Resonator, SPICE equivalent circuits, and Finite Difference Time Domain Method, two the most popular categories of analysis methods available in industry, literature and market are Transmission Line Simulator (TLSim) and 3D EM field solvers. This section will first discuss the conventional TLSim and then go into more details about 3D EM filed solvers espeicially ANSYS HFSS which is the main software tool used for the thesis. HFSS uses 3D Finite Element Method which gives the best accuracy, but also consumes a great amount of time to simulate electronic structures.

3.2.1 Transmission Line Simulator

Typical microwave engineering problem involves the transmission line which is the linking path of any net in a circuit from generator to load. In most illustrations, the parallel-wire line shown in Figure 8 represents transmission line for simplicity.

The main steps of the Transmission-line (T-line) based simulators can be summarized as follows. Each wire is referred to its closest metal plane or planes (above and below)

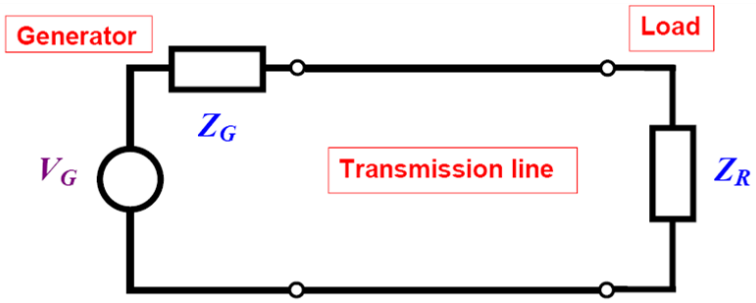

Figure 8: Typical representation of transmission lines.

and modeled using a transmission line. Two nearby parallel wires carrying a fully differential signal can also be modeled with a transmission line, and group of nearby parallel wires can be treated as multiconductor transmission lines. Characteristic parameters of the line are calculated from the interconnect geometry by a parameter extractor. The extractor is typically a two dimensional electric field solver that calculates per-unit-length capacitance and inductance matrices C and L, as well as a series per-unit-length resistance matrix R accounting for conduction losses, and a parallel per-unit-length conductance matrix G, accounting for dielectric losses,

$$\frac{dV}{dz} = -(R + j\omega L)I; \frac{dI}{dz} = -(G + j\omega C)V \tag{6}$$

where V and I are vectors with the voltages and currents along direction z of the conductors lines. Such model can be integrated in different ways with a SPICE like circuit simulator. For instance, a subcircuit model of the multiconductor T-line can be generated and included directly with the rest of the circuit for a SPICE like simulator analysis. One can also use a specialized solver to handle the multiconductor transmission lines and run a SPICE like simulator in parallel handling the rest the circuit. Electromagnetic

radiation can be calculated once all currents on the lines are known, using superposition and Green's function integrals.

T-line based simulators have the following advantages and disadvantages. As described above, the main and almost only disadvantage of T-line based simulators is a need for a clear and well defined return path for the current such as a parallel ground wire nearby or a metal reference plane. Without such a reference, the transmission line propagation hypothesis fails, and T-line based simulators cannot be used. In particular, we would like to underline that by metal reference plane we mean a complete and uniform metal plane. A layer divided into some islands of ground and "VDD" partial planes does NOT satisfy this hypothesis. All wires crossing the intersection from a ground plane region to a "VDD" plane region will not be in general simulated correctly. Holes on the plane and gaps can produce severe radiation that would not be captured by T-line simulators. For these reasons T-line simulators may not be an appropriate choice for handling, for instance, two-layers PCB or 4-layers PCB without a metal plane reference.

Assuming a good reference is present, any T-line based simulator becomes a wonderful tool for Signal Integrity and maybe even for EMI analysis. Speed is, for instance, among the main advantages of the T-line based simulators. Such simulators can usually handle entire PCB systems. Their computation speed is as fast as a SPICE like circuit simulator. T-line simulators can also account naturally for reflections from unmatched loads or terminations. Because they work in the time domain, they can also easily account for non-linear devices and loads. Reflections from wire bends could be included without much effort, even though not many available simulators implement this feature

yet.

3.2.2 Three Dimensional Field Solvers

We have seen in the previous section how a Transmission line simulator can be used as a tool of choice for all systems with a uniform metal plane or for those interconnects in a system that are fully differential. However, we have also discussed how such inadequate such simulators are for systems with a partial and segmented metal plane or with no plane at all. For these systems, one cannot make any assumptions on the type of propagation (e.g., TEM transmission line modes). The best approach for this situation at the moment is solving numerically the Maxwell equations. There exist many different numerical methods. Each method has its own peculiar characteristics that makes it suitable for one particular application rather than another. It seems that so far no one single method is suitable for all types of applications and simulation analysis. In this section, we give a brief summary of the main characteristics of the most important numerical methods in computational electromagnetics. We will underline the advantages and disadvantages of each method rather than giving any technical description of the method itself. We will point out which application may be more suitable for each method, and, in the process, we will select an approach for our specific application: EMI simulation in electronic circuits.

Before we show the differences among the methods, let us present some common features. In particular, almost all numerical methods are characterized by the following three phases:

1. **Discretization of the simulation domain**. Numerical methods cannot generally work with continuous quantities. The simulation domain is therefore subdivided into elementary cells. The main idea for most methods is that such cells are so small that field or charge and current quantities within such cells can be considered uniform. Some methods need to use the same cell size for the entire domain. This usually leads to waste of memory. Others can discretize with smaller cell size regions of space where fields or other quantities vary more rapidly in space. Some methods need to discretize the entire domain of simulation. This also can lead to waste of memory and computation power. Other methods can discretize only the parts of the simulation domain that are of interest for the particular application (for example only conductors, or only the surface of conductors).

2. **Setup of a linear system of equations**. The main purpose of the discretization is to be able, in a second phase, to convert some forms of the Maxwell equations into a linear system of algebraic equations.

3. **Solution of the linear system**. Finally the system is solved using algebraic techniques that in some cases can exploit the underlined physical structure of the problem. 3D solvers all discretize some form of Maxwell equations. We can distinguish four main classes based on the domain of the operator (giving differential equation methods or integral equation methods); and the domain of the variable (giving time domain methods or frequency domain methods).

3.2.3 Differential Methods vs. Integral Equation Methods

The natural form of Maxwell's equations is a system of differential equations. We call differential methods those methods that directly discretize such system. Examples are the Finite Difference Time Domain (FDTD) method and the Finite Element Method (FEM). Differential equations methods discretize the entire domain. Hence they usually end up with huge linear systems to be solved (tens to hundreds of millions of unknowns). Fortunately, the matrices are very sparse because each cell in the discretization only interacts with its neighbor. Hence, they massively exploit sparse matrix algorithms for the solution of their system. Because they discretize the entire domain, they can easily handle very inhomogeneous problems, for example when material properties vary quite rapidly in space. However, modeling open boundary problems can be problematic because of numerical reflections at the boundaries. Maxwell differential equations can also be rewritten in an integral equation formulation. Tools that discretize such formulation are called integral equation methods. Examples are, for instance, the Method of Moments (MoM), or the Partial Element Equivalent Circuit (PEEC) method. Integral methods need to discretize only the active regions, for example the conductors, or the surface of the conductors. Hence, they usually end up with much smaller systems than the differential methods (hundred thousands to millions of unknowns). Unfortunately, the resulting linear system has a very dense matrix because each element in the discretization interacts to all other elements. Highly inhomogeneous media are difficult to model with these methods. On the other hand, open boundary conditions and thin wire-like geometries such as in circuits can be modeled easily. We summarize in Table 1

Table 1: Comparison of differential vs. integral equation methods.

Differential Methods	Integral Methods
discretize entire domain	discretize only active region
good for inhomogeneous materials	problems with inhomogeneous materials
problem with open boundary conditions	good for open boundary conditions

the main characteristic of both integral and differential methods.

3.2.4 Time Domain vs. Frequency Domain Methods

A second important classification of numerical methods can be done based on the domain of the variables. Time-domain methods can easily handle non-linearities, furthermore they can produce very educational and intuitive animations of the wave propagation phenomena. Among the main disadvantages, in order to produce a spectrum result they need to run a very long time simulation in which all the significant modes need to be excited and need to be given enough time to develop and eventually decay. Finally, a Fast Fourier Transform of the resulting time waveforms gives the desired spectrum. The most important example of a time domain method is the Finite Difference Time Domain (FDTD) method. Another example of a time domain method is the Partial Element Equivalent Circuit (PEEC) method [71]. Frequency-domain methods consider harmonic solutions of Maxwell equations, simulating the system only at specified frequency points. Among the advantages, they naturally provide the frequency response at the specified frequency with a reasonably short simulation time, so that if only a small frequency range is required, much computation can be saved. They produce dynamical linear

Table 2: Comparison of time vs. frequency domain methods.

Time-Domain Methods	Frequency-Domain Methods
can handle non-linearities	problems with non-linearities
run a long simulation exciting all significant modes and then take an FFT	solve for specific frequency points
can produce insightful animations	can exploit new techniques for fast calculation of the dominant eigenvalues

systems on which it is possible to apply the Reduced Order Modeling techniques to get very accurate broad range frequency responses without having to evaluate every single frequency point. Non-linearities are problematic for frequency domain methods. Usually the system needs to be separated into a non-linear part and a linear part. The frequency domain method only handles the linear part. Examples of frequency domain methods are the Finite Element Method (FEM), and the Method of Moments (MoM). The Partial Element Equivalent Circuit (PEEC) method can be modified and used not only in the time domain but also in the frequency domain. [72, 73]. We summarize in Table 2 the main characteristics of both time and frequency domain methods.

In Table 3, we identify some of the most popular electromagnetic field solvers.

Finite Element Method (FEM) is a differential method working in the frequency domain. The entire domain is discretized into cells. Cell sizes can be chosen according to the fast or slow variations of fields around some parts of the simulation domain. In particular, much larger cells can be used far away from sources or conductors or non-

Table 3: Classification of some of the most popular numerical methods

Categories	Differential Methods	Integral Methods
Time-Domain Methods	FDTD	PEEC
Frequency-Domain Methods	FEM	MoM, PEEC

homogeneous media. Because the entire domain is discretized and non-uniform cell sizes can be used, this method is ideal for highly inhomogeneous materials. Because of the non-uniform cell sizes, the method has smaller memory requirements than FDTD for storing computed fields. However additional memory is required when storing explicit matrices for the computation. Because it works in the frequency domain, it naturally provides frequency responses but cannot handle non-linearities. The method has the similar problems of FDTD when dealing with open field environment.

3.3 ANSYS HFSS Simulation Technique Development

This section will illustrate the simulation techniques that had been used with ANSYS HFSS. The major steps include building up CAD model, finding/ interpolating the material libraries, defining ports, setting the boundary conditions, changing the size of the airbox, doing mesh refinement in solving adaptive passes to get the desired accuracy, then finally running the frequency sweep. We will go through each step as follows.

First, any electrical model can be drawn schematically, in 2D layouts, or can be converted into a 3D CAD model. We have fabricated a simple Power Distribution

Network at package level and manually drew it in HFSS. After a comparison with the converted model from SIWave, a very accurate 3D CAD model was obtained as shown in Figure 9. Our model consists of a copper plane at the bottom layer which is connected to a small square-shaped pad on the top layer, and another copper plane on the top layer. Those two nets are named as "VCC " and "GND ".

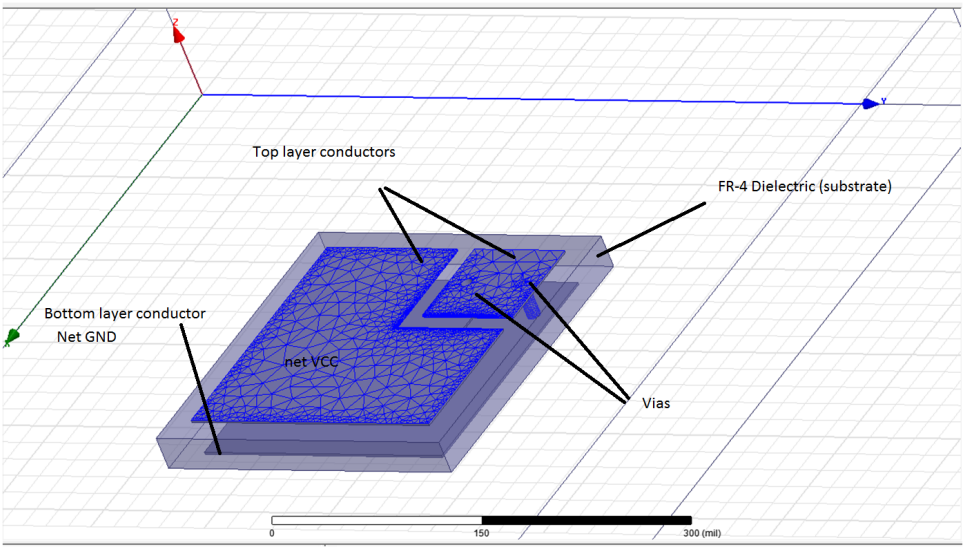

Figure 9: 3D CAD model of a simple power Distribution Network in HFSS.

Second, libraries of material parameters should be adjusted following the datasheet provided by PCB manufacturer. In this model, copper planes are plated with solder. Hence, due to the skin effect, the model libraries for conductors should be "solder", the conductivity of solder is 7.7e6 $siemens/m$, close to the conductivity of "solder" material in HFSS. For FR402 dielectric substrate, we always have to use frequency-dependent dielectric constant and loss tangent. We can pick any of the given frequency points from the datasheet to import to the library and enable the option for fitting methods for

material properties in HFSS.

Third, the port will be drawn in such a way that its size agrees with the actual size of the probes we used with the PNA. Figure 10 shows the defined port between the two nets. Its width is 40 μm corresponding the the width of the Z-Probe we used with the Agilent PNA Network Analyzer. The boundary is set to be radiation for all of the size of the air box except for the bottom side since the DUT is placed on a metal (Perfect E) surface in the clean room. Simulations should reflects what is going on at the measurement station.

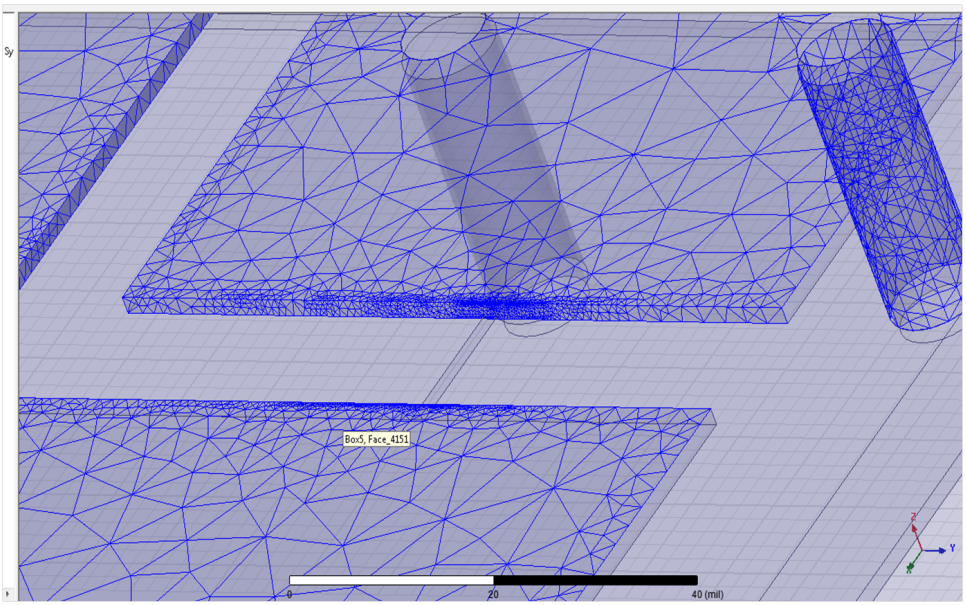

Figure 10: Port definition

Next, few simulation sweeps will be run with the changing air box size. The bigger the air box should give better convergence but very time consuming. Figure 11 shows the convergence of the solution sweeps when the size of the airbox changes.

For the next step, we will do the mesh refinement until the desired accuracy is

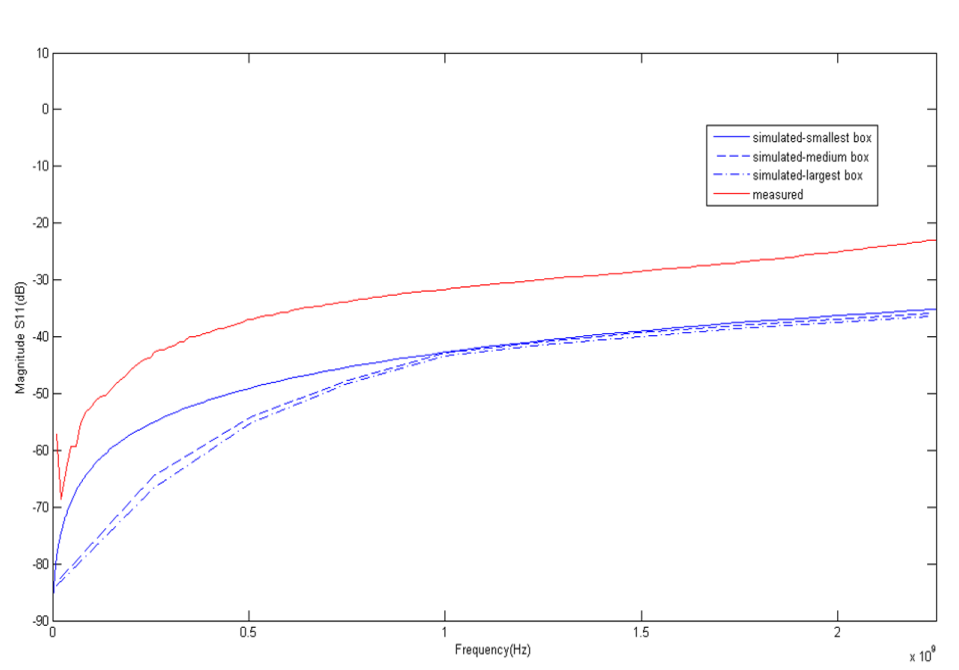

Figure 11: Convergence of the solution sweeps when the size of the outer air box changes.

acquired. Table 4 shows the relative error of adaptive passes with the Monte-Carlo method. Figure 12 shows the impedance profile of the PDN after the simulation had completed by Cadence (red solid) and HFSS (blue solid).

Figure 13 shows the comparisons of simulated and measured S-parameters. Figure 14 show the comparison of the simulated and measured impedance profiles of the PDN.

Another example is shown in Figure 15 which had been simulated in [1]. This model was simulated by HFSS (Figure 15) and Cadence (Figure 16). The insertion loss in [1] is shown in Figure 17. It agrees well with the result generated by both Cadence (Figure 18) and HFSS (Figure 19).

Another example is presented in Figure 20 which is from [2]. Figure 21 shows the simulated and measured results of S_{11} and S_{12}. Figure 22 shows that my simulated result

Table 4: FEM Mesh refinement

Pass number	Total Tetrahedras	Max Mag. ΔS
1	3458	N/A
2	13842	0.13824
3	55391	0.01777
4	70939	0.0049216
5	87916	0.001516
6	97871	0.00061112
7	111363	0.0004124
8	129281	0.00034451
9	152085	0.00019035
10	172823	0.00013465
11	208606	0.00016358

agrees better with the author's measured result.

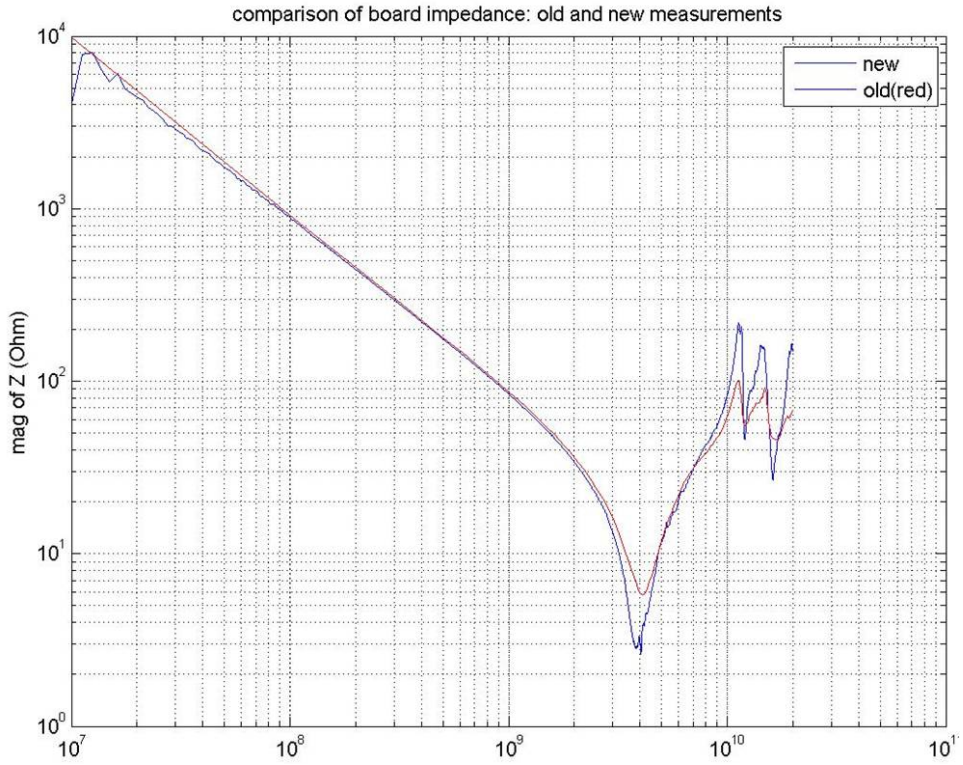

Figure 12: Comparison of simulated impedance profiles of the PDN generated by Cadence (red) and HFSS (blue).

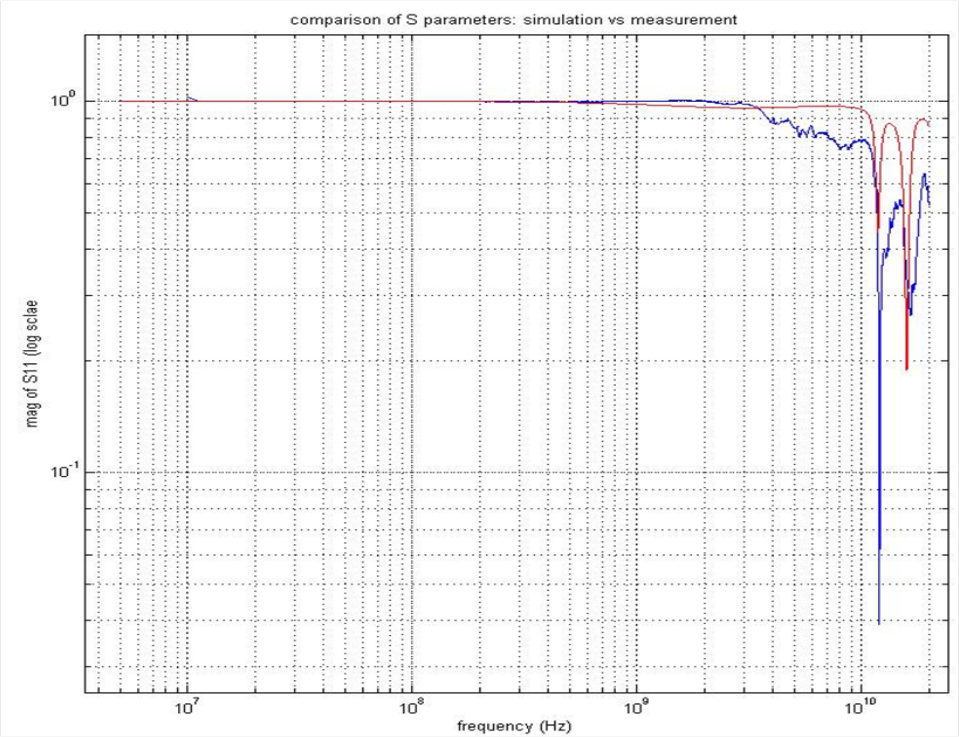

Figure 13: Comparison of simulated (red) and measured (blue) of S-parameters of the PDN.

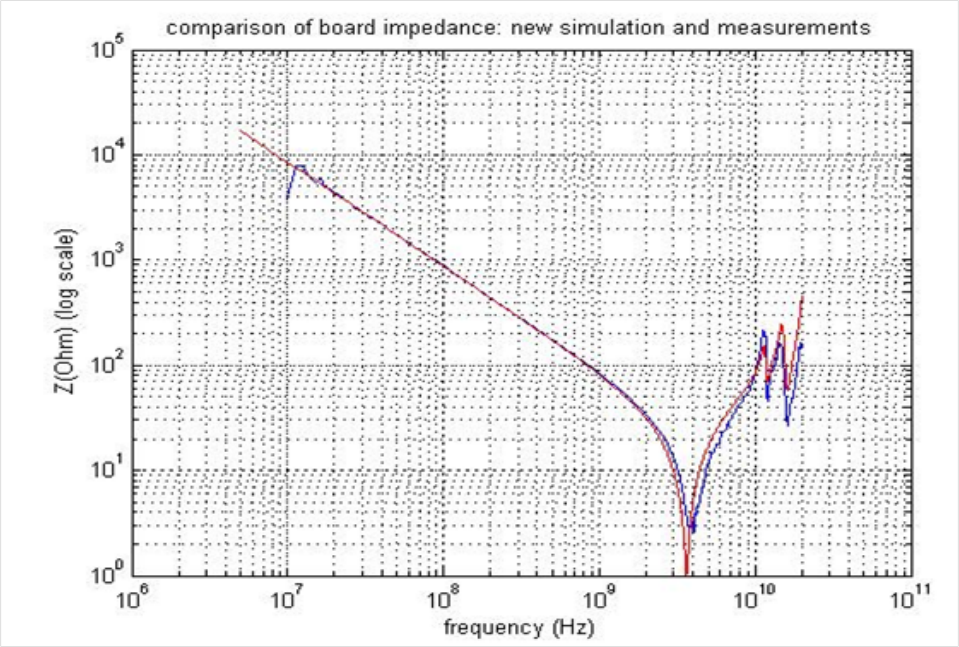

Figure 14: Comparison of simulated (red) and measured (blue) impedance profiles of the PDN.

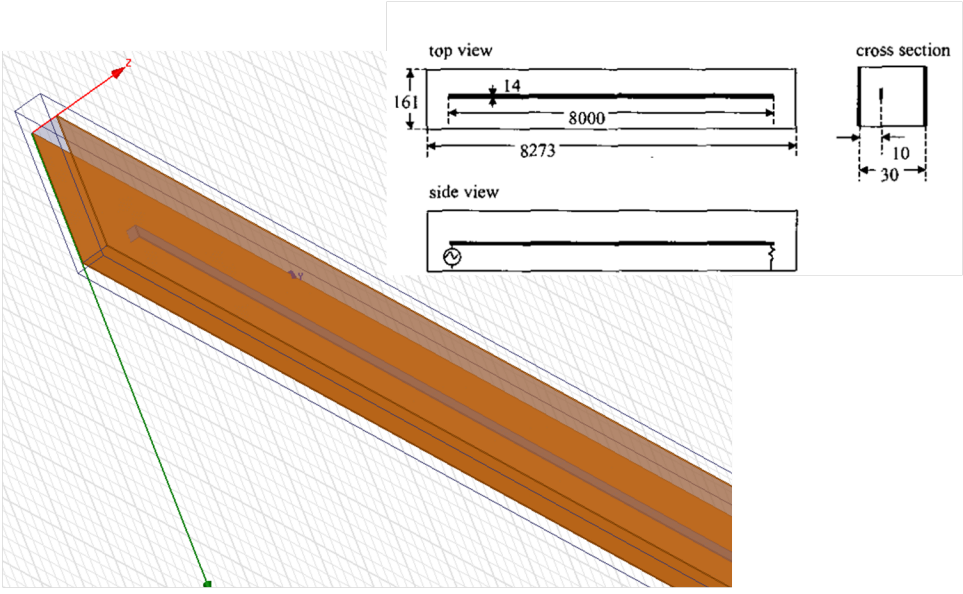

Figure 15: HFSS model of [1].

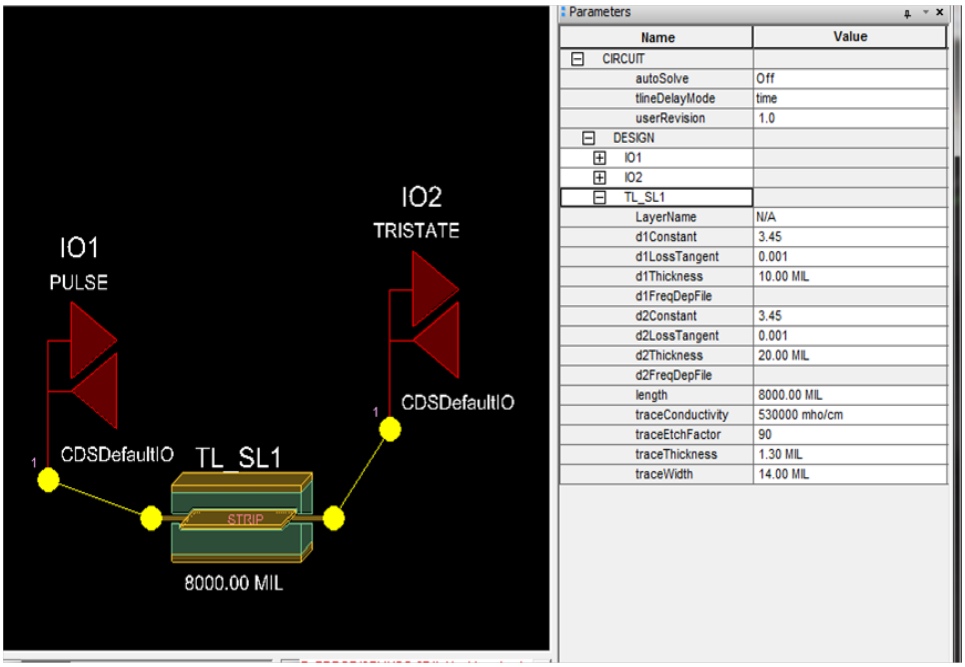

Figure 16: Cadence model of [1].

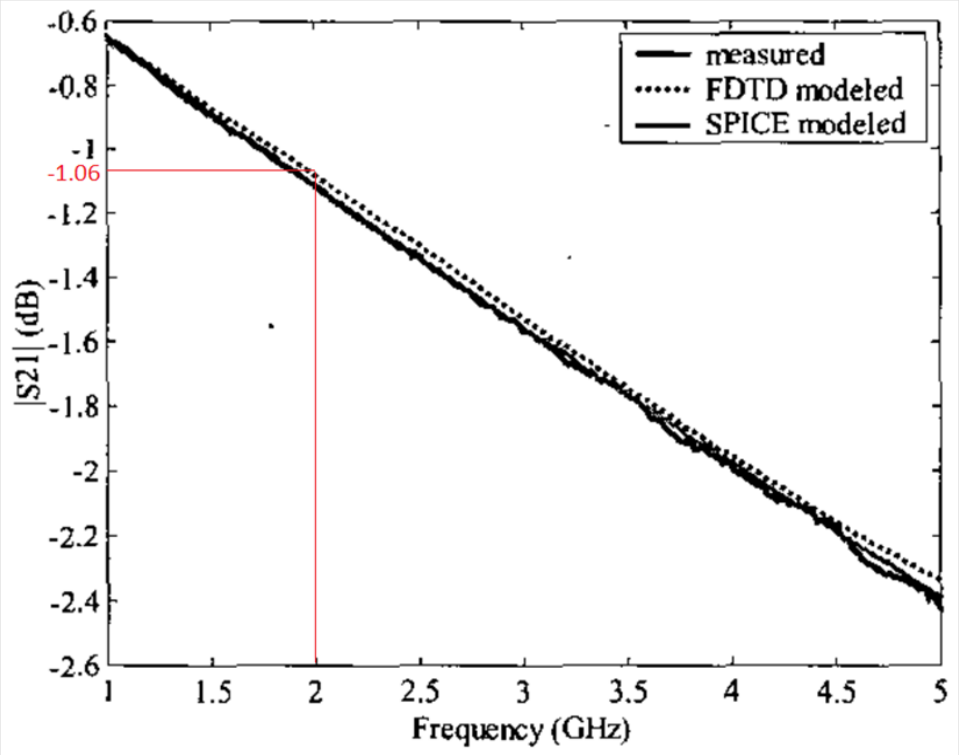

Figure 17: Insertion loss of [1].

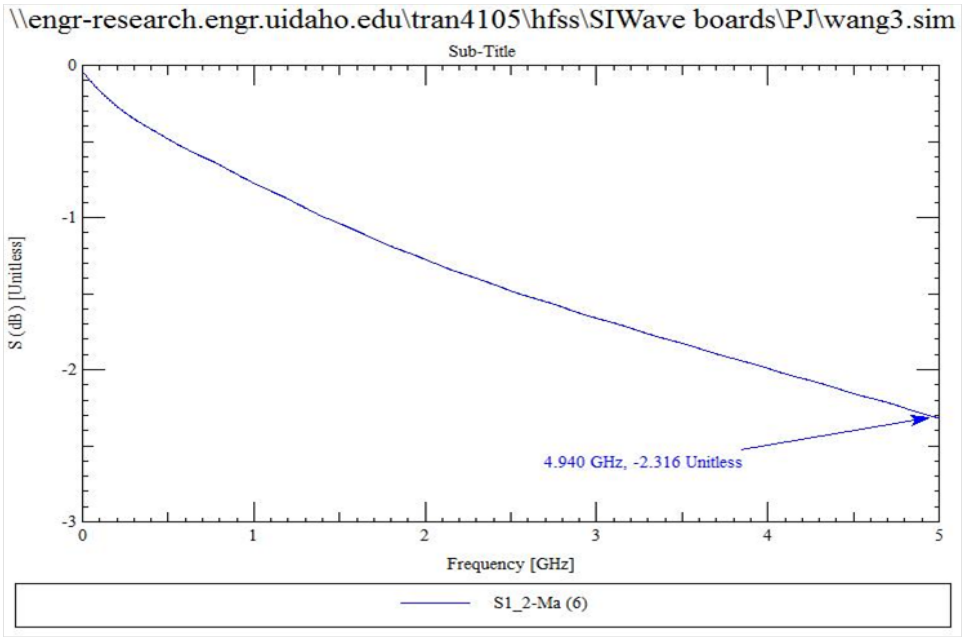

Figure 18: Insertion loss of [1], simulated by Cadence.

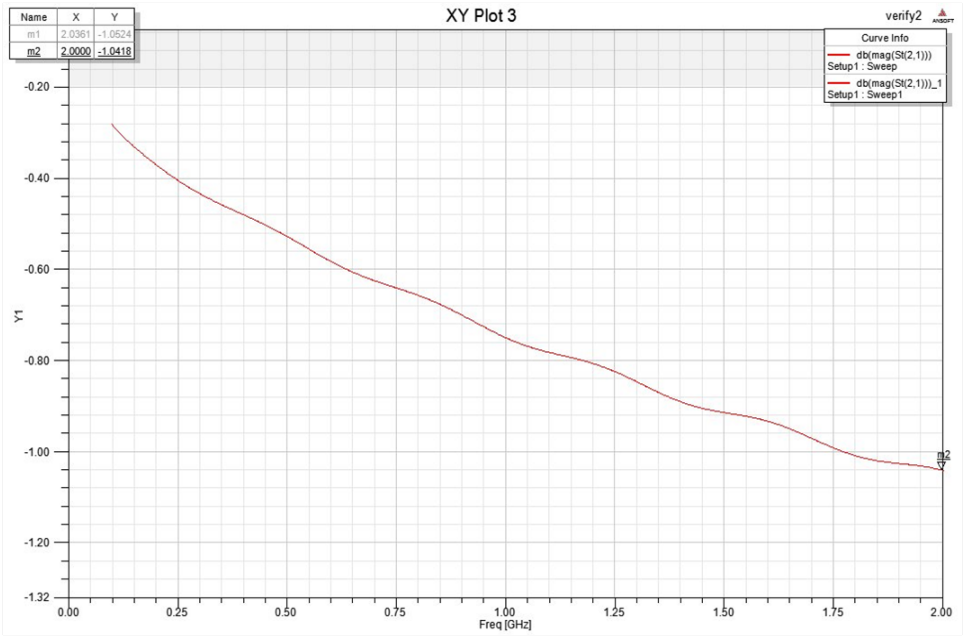

Figure 19: Insertion loss of [1], simulated by HFSS.

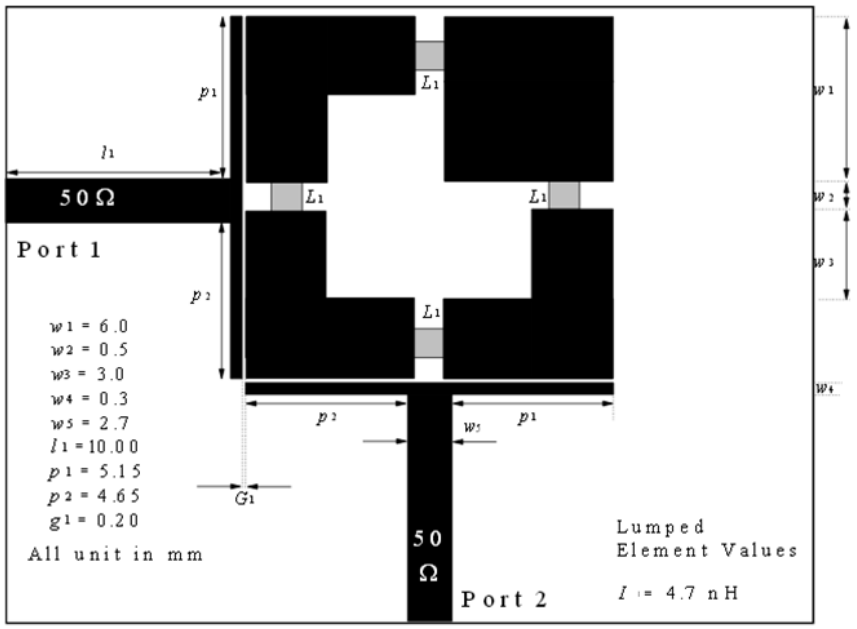

Figure 3.14: Top view of lump microstrip square ring filter

Figure 20: Microstrip filters modeled in [2].

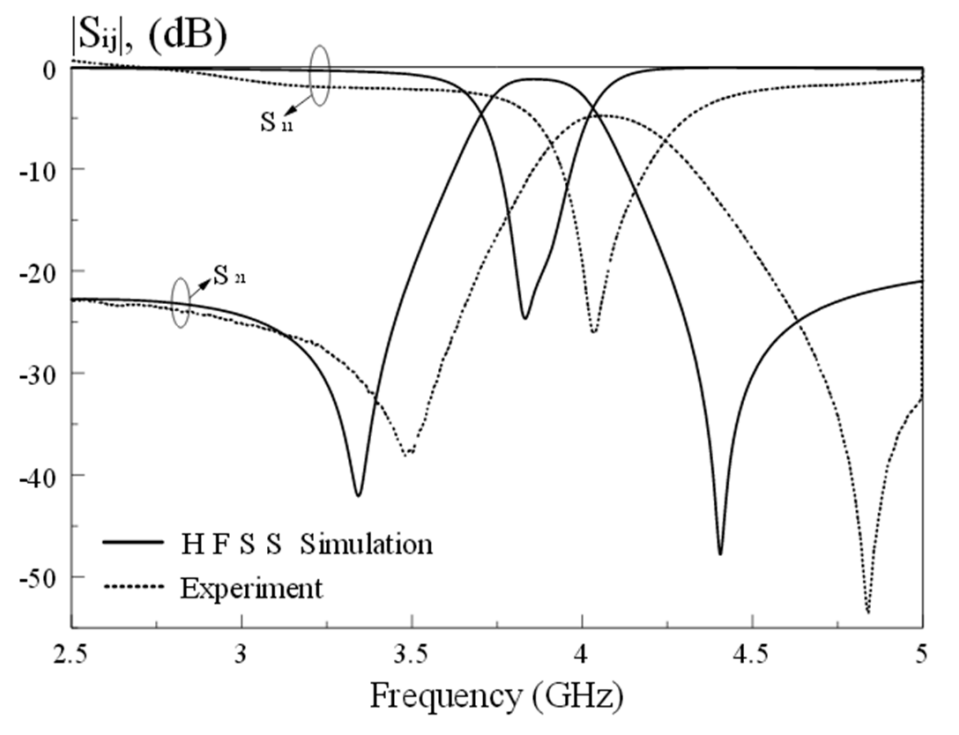

Figure 21: Return and Insertion loss of the filter simulated in [2].

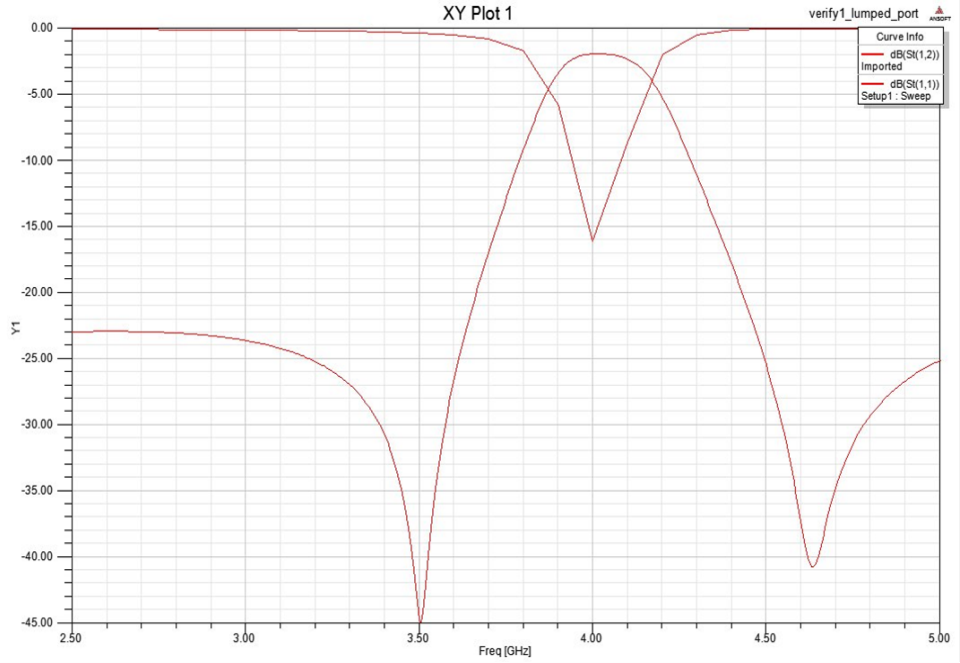

Figure 22: Return and Insertion loss of the filter simulated in [2].

4 Measurement Procedures and Verification

4.1 PNA Network Analyzer N5225A

In the class 10,000 clean-room, we have an Agilent's PNA Network Analyzer model N5225A for microwave measurements. It has a capability to measure structures in the frequency range from 10MHz to 50 GHz. Four single-ended ports along with two internal signal sources from will allow one to extract both 4-port single-ended S-parameters and 2-port mixed-mode S-parameters. An electrostatic discharge protection mounted on user's wrist is required to protect to PNA. Static electricity usually come from our body, and it can damage circuit elements when discharged. To prevent damage to the instrument, we will always have a grounded which mean to wear wrist strap before touch instruments. The PNA we have purchased with standard 4- port configuration and temporary license for integrated true-mode stimulus application (iTMSA). The iTMSA provides true differential and true common stimulus and enables balanced measurements under real operating conditions. The iTMSA also has the ability to do forwardonly sweep, reverse-only sweep, and frequency or power sweep with arbitrary phase for balanced measurements. The operating environment is also important to maintain better performance. The PNA is necessary to keep in temperature between 20 degree and 26 Celsius, and when calibration has done, the temperature must maintain within 1 degree Celsius. The humidity should keep 0% to 95% at 40 degree Celsius maximum, non-condensing. The PNA need to warm up 30 minutes before operating to have accurate measurements.

The PNA has measurement uncertainty. It includes the residual systematic errors

and the random errors even after calibration. The systematic errors include Directivity, Source match, Load match, Reflection and transmission frequency tracking, and Isolation (crosstalk). The random errors include Noise, Drift, Connector repeatability, and Test cable stability. All the measurement must include those error terms. This is unpredictable errors [74].

4.2 Calibrations

Good equipment and calibration standards are required to have accurate S-parameter measurements. There are several types of calibration methods. The most common are short-openload-reflect (SOLT) and thru-reflect-line (TRL). Why do we need to do calibration? We should be able to connect adaptors, cables, and probes, and do the measurement. Any measurements without calibration would be inaccurate, but even with good calibration that can still contain some errors which cannot be removed. Calibrations are usually applied to network analyzer, and remove the errors from instruments, cable, probe or SMA connector. After calibrations are done, there would be a new reference point. Depending on its frequency range and application both calibrations have its own advantage and disadvantage.

SOLT calibration is easy to perform and it is most widely used in coaxial cable measurements. There are many coaxial calibration kits available to fit most of the connector types [74]. There are some standard for both TRL and SOLT. For TRL THRU, it should be no loss and no characteristic impedance, S21=S12=1, and S11=S22=0 for zero length. If non-zero length, characteristic impedance of THRU must be the same as

the LINE, and attenuation of THRU does not need to be known. For TRL REFLECT, reflection coefficient magnitude is optimally 1, the reflection coefficient must be identical on both ports, and the phase of reflection coefficient must be within quarter length or 90 degrees. For the TRL LINE, characteristic impedance of the LINE starts as the reference impedance of the measurements. The length of line should be quarter wavelength, and the ration of usable bandwidth is 8:1 for a single THRU/LINE pair [74]. We have used only SOLT calibration for two ports calibration and SOL for one port calibration. In the PNA N5225A, the calibration

4.3 Probes, connectors, and calibration substrates

In this work, we use probes and SMA connector to perform S-parameter measurements. The probes we first used was GS-500 Z-Probe for one port measurement, and later on we purchased SG-500 Z-Probe for two port measurement. There are many different vendors and types of probes for difference purpose and application. The price can be vary from several hundred to several thousand dollars. The probes can be described as infinity probes, air coplanar probes, |z| probes, RFIC and functional test probes, board test and signal integrity probes, and special-purpose RF/microwave probes. We have air coplanar probes and Z probes in the cleanroom. The Z probes can be divided into four different types: Z Probe, Dual Z Probe, Z Probe Power, and Z Probe PCB

Those Z probe can be used from DC up to 67GHz, and the connector of probes from 1.85mm 2.4mm, and 2.92mm. The probes have GS, SG GSG, SGS, GSSG, and GSGSG configuration. GS represent the ground and signal for example: GSG is ground-signal-

ground probe. The pitch of Z probe can be as small as 50 um and up to 2500 um. The probe I used was Z Probe PCB GS- 500 and SG-500. Those probes were used for PCB, IC pins and ceramic substrate probing. Figure 23 is an air coplanar probe.

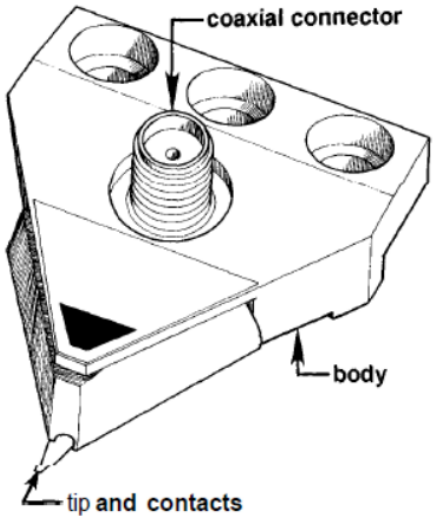

Figure 23: Air Coplanar Probe

How to operate the Z probe to have best accurate and secure measurement? The probe tips are very easy to be broken, so to avoid overtravel is very important. The Z probe is recommended overtravel is 5 um on gold and 30 um on aluminum pads. Figure 24 are the cases of worse and the best overtravel. The Figure 25 describes the top view, side view, and bottom view of probe and substrate.

Using appropriate connectors would save measurement cost since they will protect both ends of probes and cables from being damaged. There are many different sizes of connector. Each different size of connector could operate in different range of frequency. The smaller size would have higher operated frequency. The connector for our Z-probe

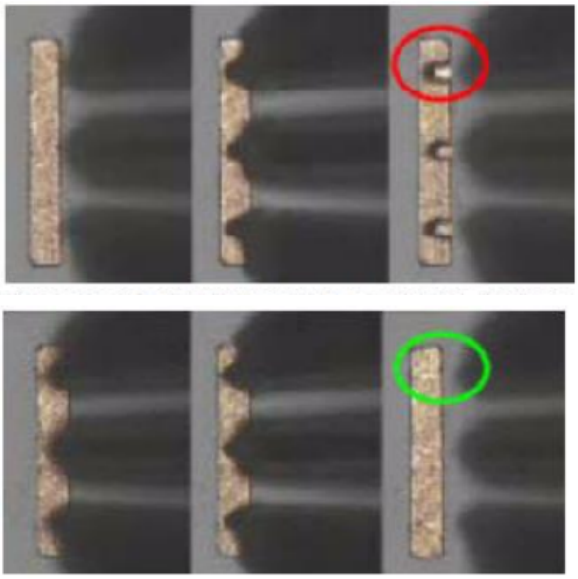

Figure 24: Worst case (red) and best case (green) for probing

is 2.4mm to 2.92 mm. The 2.4 mm is to connect to cable, and 2.92 mm is for probe. Figure 27 shows the probe and probe with connector.

For the calibration substrate, purchasing from a company is most reliable decision, but most of time calibration substrates cost much more than we can afford. Because of high roughness of PCB manufacture company, it is not reasonable to make your own calibration substrates for probes. Calibration substrates for probes would have short, open, load, thru, and line. Those substrate is made with limit range of pitch. The calibration substrate I used is called CSR-5, and is made especially for Z-probes. The CSR-5 has characteristics listed in Table 5.

The standards on the divided into two groups: transmission and reflection. There are aliment standard which can be used for computer control probes that given (X, Y) coordinates. For two ports calibration, the probe must be GS/SG configuration. Figure

Table 5: CSR-5 Characteristic

Material	Alumina
Size	16 x 13.7mm
Thickness	635um
Dielectric Constant	$\epsilon = 10.2$
Effective Permittivity	5.73
Effective Velocity	0.43
Phase Velocity	7.36 ps/m
THRU Impedance	nominally 50 Ω
DC accuracy (LOAD)	$50\ \Omega + / - 0.15\Omega$
Temperature	between -263^oC and $+150^oC$
Maximum Power	0.3W

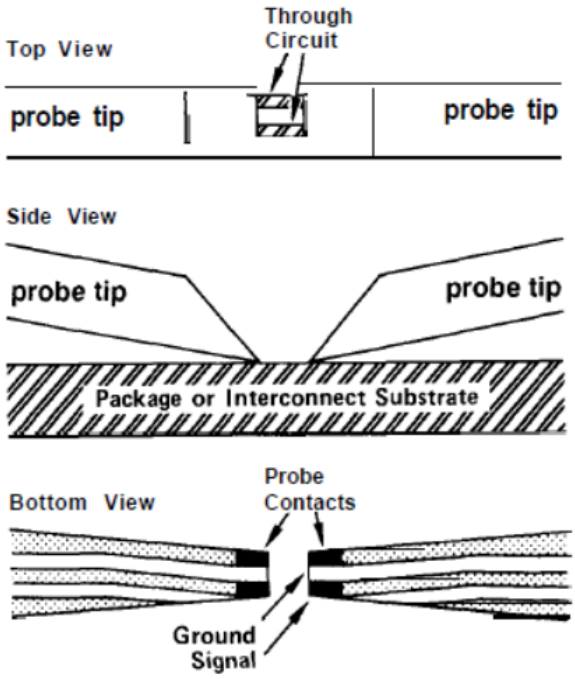

Figure 25: Top, side, and bottom view of probe

28 shows the spacing of probe and calibration standard on the substrate.

4.4 Measurement Procedures and Equipment

For this research work, we used N5225A PNA microwave network analyzer that has four ports with two internal sources and operate from 10 MHz to 50 GHz. Before doing any measurement, we needed to use pure alcohol to clean up the entire connectors and adaptors as shown in Figures 29 and 30 (connectors 33 and cables). After cleaning, we needed to apply gage kit calibration. There are two type of gage kit in our lab. One is 2.92 mm/3.5 mm manual gage kit and the other one is 1.85 mm/ 2.4 mm digital gage kit. Those gage kit calibration tools are to test all the connectors and adaptors

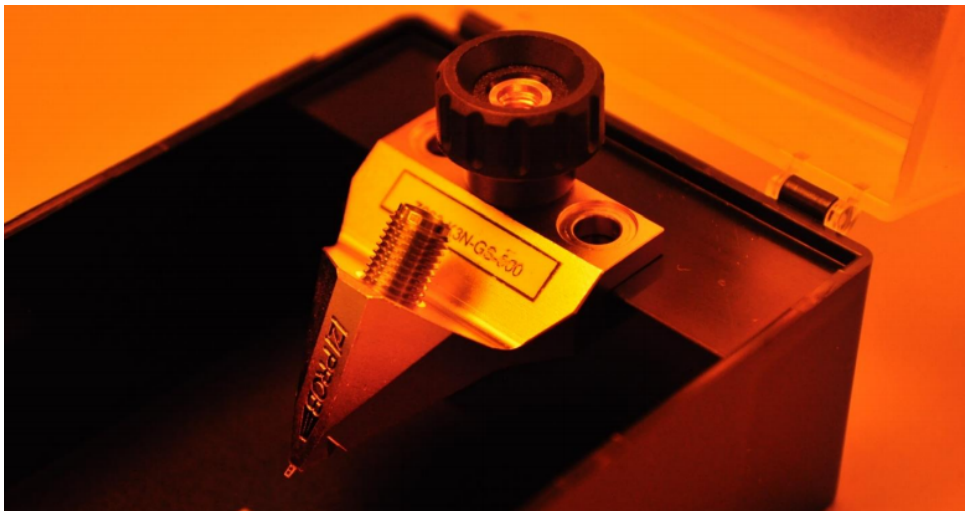

Figure 26: Z-Probe PCB GS-500

have corresponding contact as shown in Figure 31 and 32. The gage kits need to be calibrated with standard connector then apply 4 lb. wrench and set to zero (Figures 33 and 34). Next apply gage kit to adaptors and connectors. To make correct contact, turn the screw in one end and hold it tight in other end. This can avoid the connections get grind each other and damage the center pin. After gage kit connects to adaptors or connectors use the correct wrench with certain force. Now from the gage kit, the value must be negative which mean good connection (Figures 34 and 35). If the values turn to positive, the adaptors or connectors would have been damaged. If we ignore what is happening and continue to use those adaptors, whatever connects with those damage adaptors would be damaged as well.

For the first step of measurement setups, probes are carefully taken out from their box. Models of probes are Cascade Microtech GS 500 and SG 500 Z-Probe. The GS 500 means ground-signal 500um pitch at tip. Figure 26 shows GS 500 Zprobe and SG

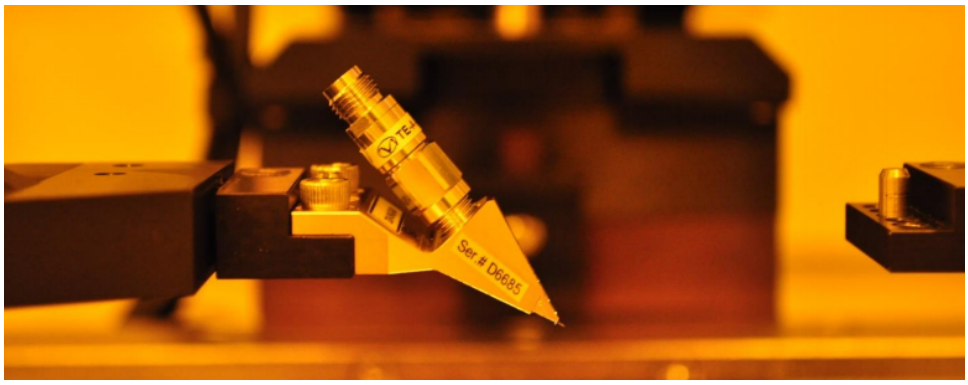

Figure 27: Z-Probe PCB SG-500 with connector

500 Z-Probe. Place Z-probe to the station, and connect with 2.4mm/2.92mm adaptor (Figure 27 shows the probe with adaptor). Connect cable to PNA and adaptor. The cable is 2.4 mm at connection with 50 GHz maximum operate frequency.

Equipments include PNA N5225A, probe station, vacuum, lights, microscope.

Level substrate and Calibration: Figure 28 shows (CSR-5 and substrate) The CSR-5 has alignment short open load, and line standard. To perform calibration method ex: SOL, SOLT, TRL etc., alignment standard provide accurate probe distance which give same amount of parasitic capacitance in each measurement.

4.5 Device Under Test (DUT)

During my research, we have created three different PCB boards for testing. First and second PCB were made for Z-probe probing. The last one was made using SMA connector which is much reasonable and cheaper. The figure below was first PCB that had probing space of 10 mil. There were short, open, and load calibration standard

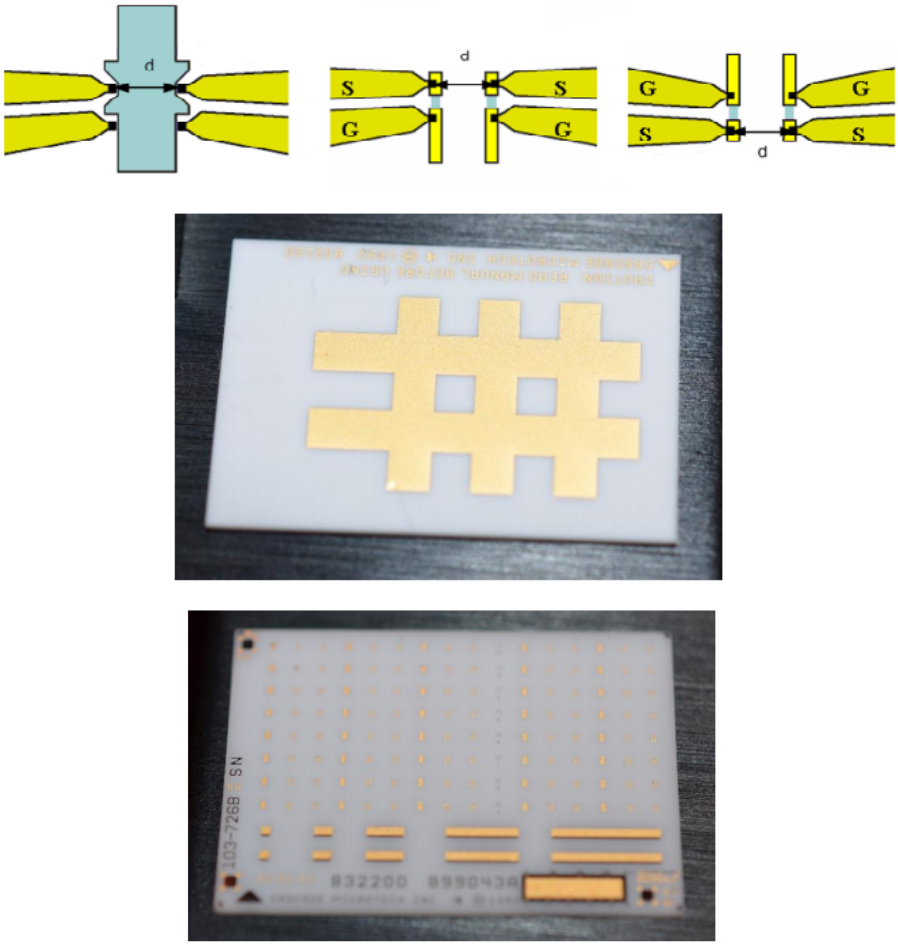

Figure 28: Probe spacing, Contact substrate, and Calibration substrate, respectively

on this PCB. Because of unpredictable calibration parameters, the measurements were done with inaccurate result, but it was really good experience to make this one. By knowing the measurement was not good enough, we purchased the calibration substrate CSR-5.

Figure 29: Connector or cable cleaning

Figure 30: Gage kit

4.6 Calibration and measurement results

How do we know if my calibration is correct? The easiest way to confirm is re-measure the calibration standard again for example: short, open, and load. From smith chart, I know the open circuit should locate in right hand side within the circle. The short circuit should locate in left hand side within the circle. The reason one is at left and other is at right that is because both of the magnitude are the same but 180 degree out of phase. For the perfect calibration, the plot in smith chart would show only one dot,

Figure 31: Analog gage kit (3.5/2.92mm)

but it is impossible to happen. I try to obtain correct calibration data from setting my goal to be the plot within circle. If the plot go beyond the circle which mean the device become active, then the calibration would consider incorrect. From smith chart plot I can tell short, open, and load measurements.

Figure 32: Digital gage kit (2.4/1.85mm)

Figure 33: Apply two wrench to tight connector

Figure 34: Digital gage kit calibrate cable (negative reading)

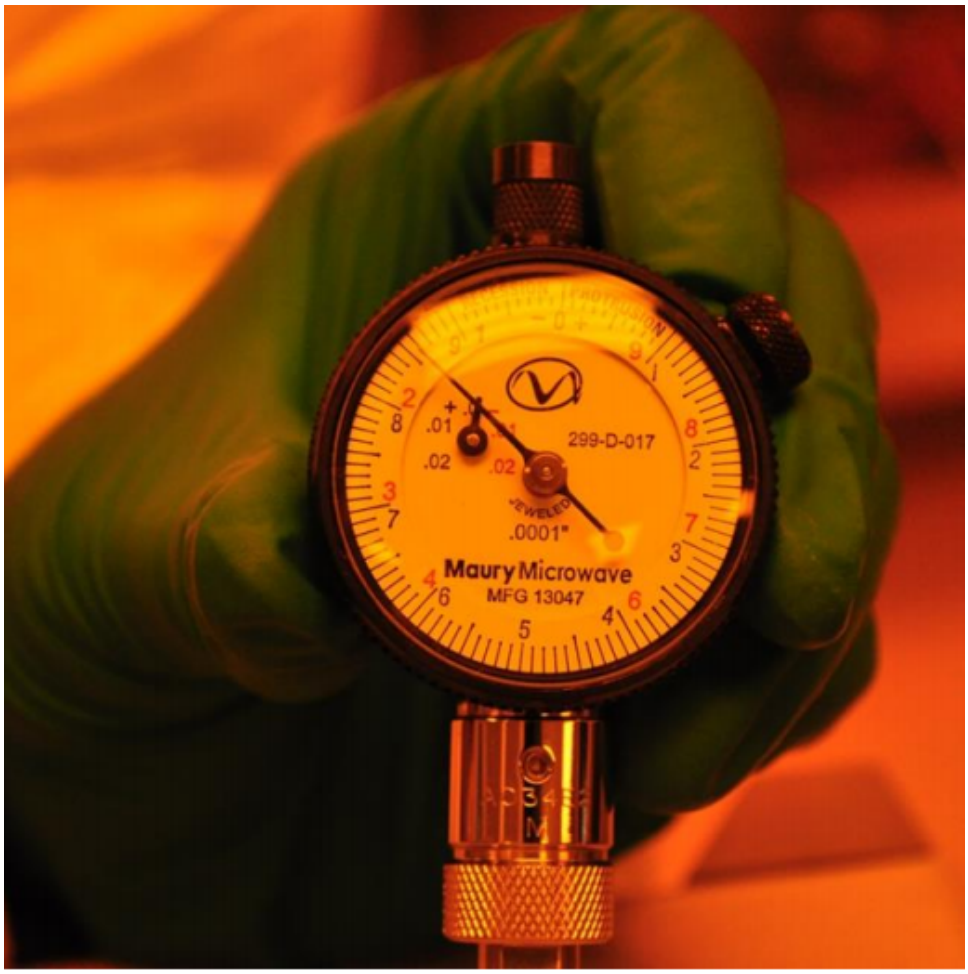

Figure 35: Analog gage kit calibrate connector (negative reading)

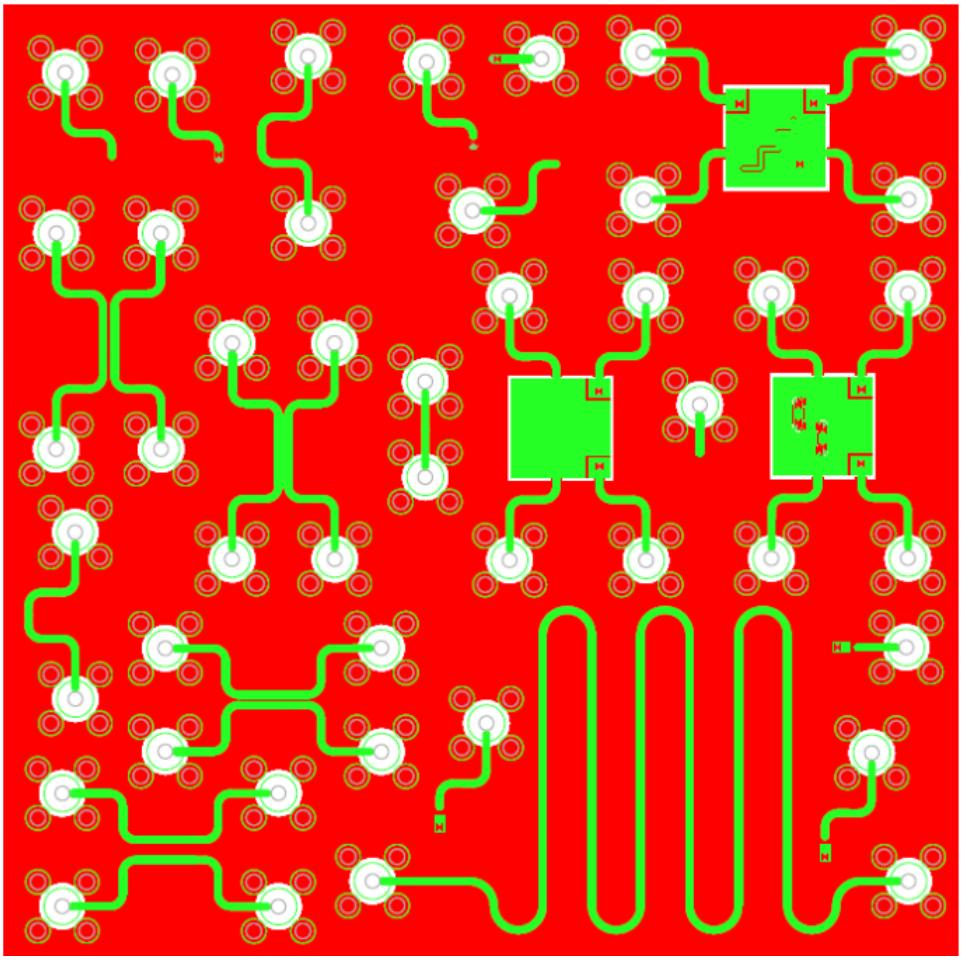

Figure 36: Third PCB design with SMA connector

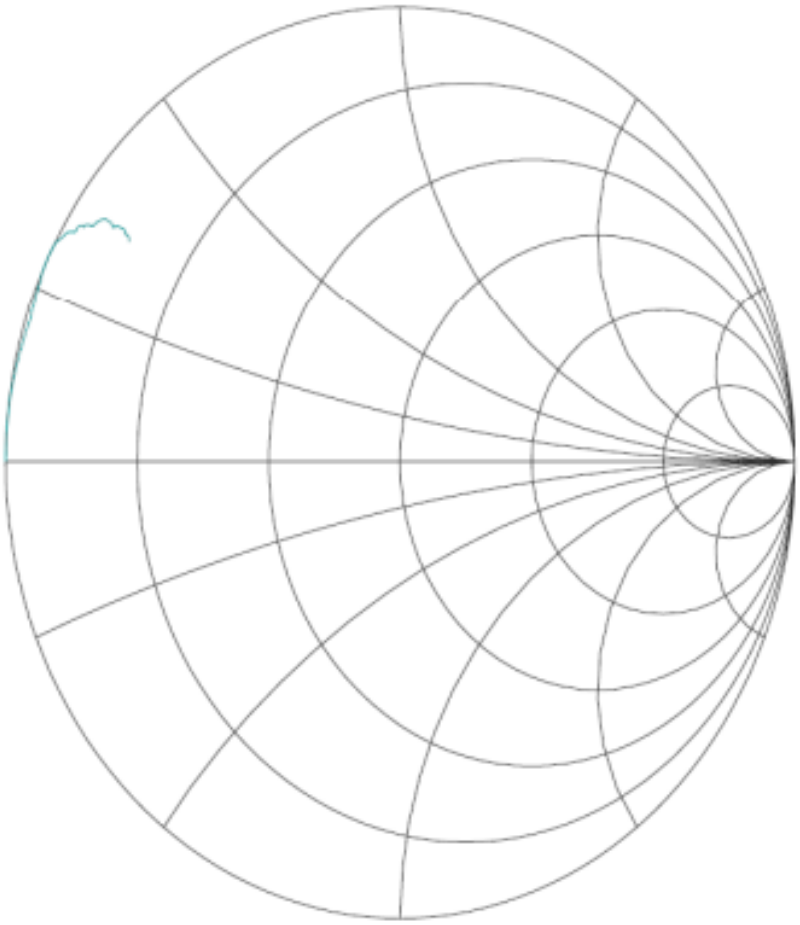

Figure 37: Measurement of a short connection

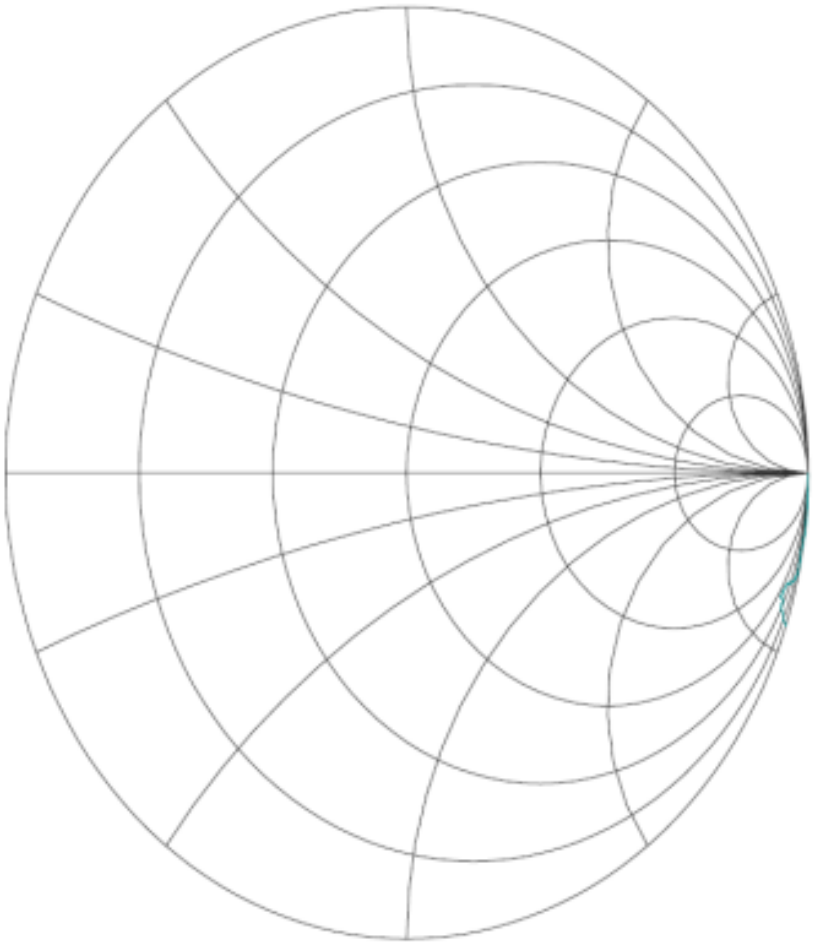

Figure 38: Measurement of an open connection

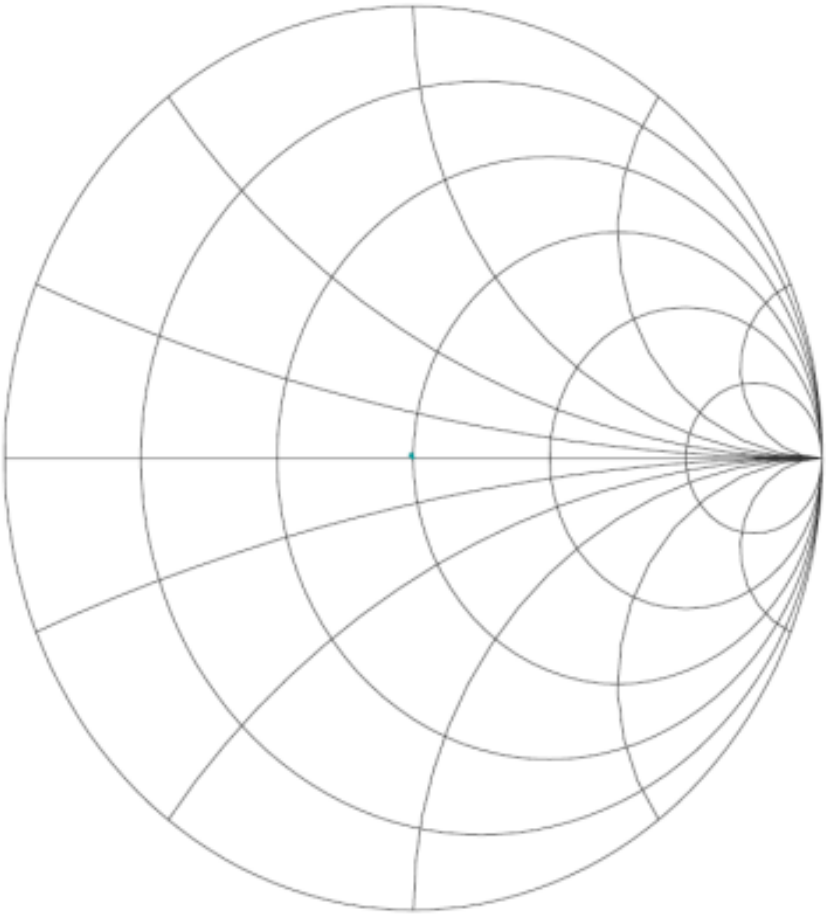

Figure 39: Measurement of a 50 Ω load

5 Conversion from Single-Ended to Mixed-Mode S-Parameters

Accurate extraction of mixed-mode S-parameters from single-ended S-parameters is critical for signal and power integrity co-simulation where SSN is generated mainly by high-frequency interconnects. A standard conversion between single-ended and mixed-mode S-parameters involves inversion of a transformation matrix. If there is no coupling, this transformation matrix is orthogonal and numerical inversion can be done accurately. In the presence of coupling, the transformation matrix depends on S-parameters and may become ill-conditioned, i.e. has high condition number, for some values of physical parameters resulting in unstable inversion of the transformation matrix and leading to highly inaccurate converted mixed-mode S-parameters. To analyze a possibility of ill-conditioning, we consider two cases: broadside coupled striplines and coupled microstrip pairs. We find that in both cases when two transmission lines get very close to each other and, thus, the coupling is strong, the condition number becomes very large. In this case, regularized methods from the theory of ill-posed problems should be used, for example, the truncated SVD method, to obtain accurate mixed-mode S-parameters.

5.1 Single-Ended and Mixed-Mode S-Parameters

In this section, we present some fundamental concepts on single-ended and mixed-mode S-parameters using a four-port single-ended network shown in Fig. 40, where port 1 and 2 represent the differential input and port 3 and 4 represent the differential output. Port

1 and 3 are positive voltage references, port 2 and 4 are negative ones. The conversion

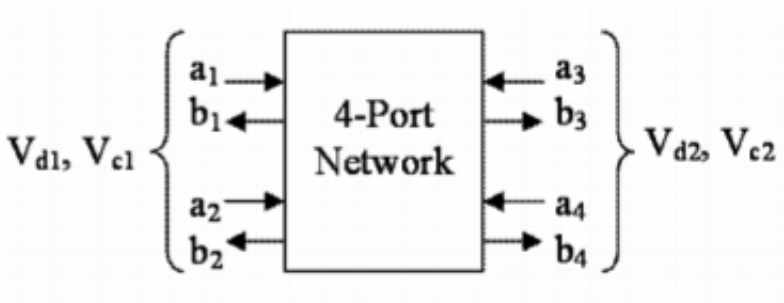

Figure 40: Four-port network.

between single-ended S-parameters and mixed-mode S-parameters, denoted by S^{mm}, for this four-port network is provided by [22]:

$$S^{mm} = (M_1 S + M_2)(M_2 S + M_1)^{-1} \tag{7}$$

where

$$M_1 = \begin{pmatrix} \frac{1+k_{oo}}{2\sqrt{2k_{oo}}} & -\frac{1+k_{oo}}{2\sqrt{2k_{oo}}} & 0 & 0 \\ 0 & 0 & \frac{1+k_{oo}}{2\sqrt{2k_{oo}}} & -\frac{1+k_{oo}}{2\sqrt{2k_{oo}}} \\ \frac{1+k_{oe}}{2\sqrt{2k_{oe}}} & \frac{1+k_{oe}}{2\sqrt{2k_{oe}}} & 0 & 0 \\ 0 & 0 & \frac{1+k_{oe}}{2\sqrt{2k_{oe}}} & \frac{1+k_{oe}}{2\sqrt{2k_{oe}}} \end{pmatrix}$$

$$M_2 = \begin{pmatrix} \frac{1-k_{oo}}{2\sqrt{2k_{oo}}} & -\frac{1-k_{oo}}{2\sqrt{2k_{oo}}} & 0 & 0 \\ 0 & 0 & \frac{1-k_{oo}}{2\sqrt{2k_{oo}}} & -\frac{1-k_{oo}}{2\sqrt{2k_{oo}}} \\ \frac{1-k_{oe}}{2\sqrt{2k_{oe}}} & \frac{1-k_{oe}}{2\sqrt{2k_{oe}}} & 0 & 0 \\ 0 & 0 & \frac{1-k_{oe}}{2\sqrt{2k_{oe}}} & \frac{1-k_{oe}}{2\sqrt{2k_{oe}}} \end{pmatrix}$$

The coupling coefficients k_{oo}, and k_{oe} are defined from

$$Z_d/2 = Z_{oo} = k_{oo}Z_0, \quad 2Z_c = Z_{oe} = k_{oe}Z_0,$$

where Z_0 is the reference impedance, e.g., $50\,\Omega$; Z_{oo} and Z_{oe} are odd- and even-mode characteristic impedances. The values of the coupling coefficients k_{oo} and k_{oe} depend on how much signal coupling is present in a differential network [22] and $0 \leq k_{oo} \leq 1$, $k_{oe} \geq 1$.

Since the conversion formula (7) involves the inversion of matrix $T = M_2S + M_1$, we would like to analyze the accuracy of such inversion, which we do by analyzing the condition number of this matrix. When there is no coupling, M_2 is the zero matrix, while M_1 is an orthogonal matrix, so matrix T is well-conditioned with the condition number $cond(T) = 1$. When there is coupling, the conversion matrix T depends on both M_1 and M_2 as well as S-parameter matrix S. While matrices M_1 and M_2 are orthogonal, nothing is known about matrix S, and, hence, about $T = M_2S + M_1$. So, our goal is to analyze the condition number of this matrix in the presence of coupling. If the condition number is large, matrix T is ill-conditioned and direct inversion of this matrix may be highly unstable, which would cause inaccuracy in conversion between single-ended and mixed-mode S-parameters. In such situations, direct inversion of T should be avoided and the mixed-mode S parameters S^{mm} should be computed as a linear system

$$S^{mm}(M_2S + M_1) = (M_1S + M_2)$$

using, for example, the truncated singular value decomposition (SVD) method to regularize the problem [27].

5.2 Broadside Coupled Striplines

As a model problem, we consider broadside coupled striplines depicted in Fig. 41. The conductors are 80 percent conductivity relative to the International Annealed Copper Standard (IACS). The dielectric is FR-4 with relative permittivity $\epsilon_r = 4.5$. For this example we have chosen w_0 to be 0, conductor width w, substrate thickness H, and conductor spacing s. The problem is made dimensionless by considering w/H and s/H ratios to obtain a closed-form formula used in MATLAB approximation of matrix T. The range of s/H is from 0 to 1, and that of w/H is from 0 to 5 [75, p. 146]. This type of trans-

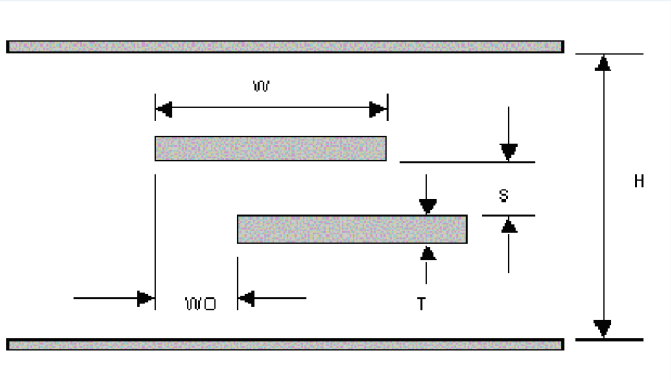

Figure 41: Geometry of broadside coupled striplines.

mission lines is used for analysis because the closed-form formula can be applied for a uniform dielectric material. The approach we used here follows the conversion procedure reported in [22]: first calculate the odd- and even-mode characteristic impedance to find coupling constants k_{oo} and k_{oe}, then construct the matrix M_1 and M_2. The single-ended S-parameters are approximated as follows: $|S_{11}| = |S_{22}| = |S_{33}| = |S_{44}|$ are approximated as reflection coefficients, $S_{14} = S_{23}$ are usually very small, i.e. 10^{-40}, $S_{12} = S_{12}$

and equal to coupling coefficient [75, p. 354], and $S_{12} = \pm\sqrt{1 - S_{11}^2 - S_{13}^2 - S_{14}^2}$ due to the conservation of energy. To simplify the problem, S-parameters is assumed to have zero phase to avoid the complexity of frequency dependence.

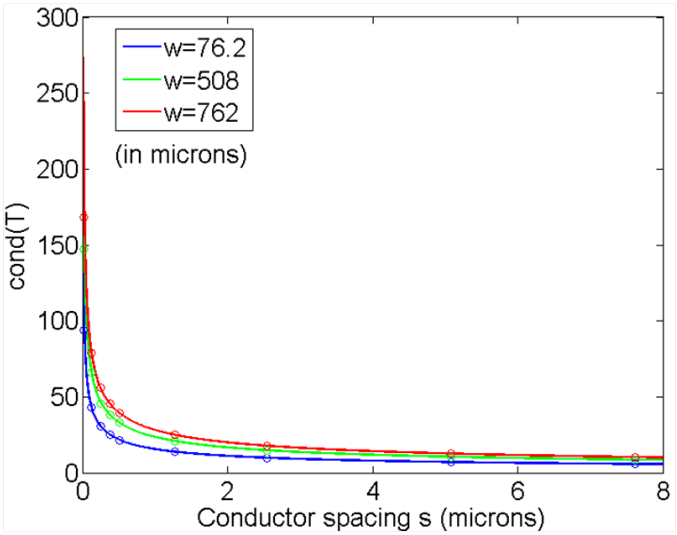

Figure 42: Cond(T) as a function of spacing s for different widths in the case of broadside coupled striplines.

The condition number of matrix T as a function of width w/H for different (small) values of spacing s/H between traces is shown in Fig. 42, for the case when $H = 20$ mils. The graph shows that as the differential traces come close to each other, or the spacing s approaches 0, the condition number of T increases, which can affect the accuracy of conversion between single-ended and mixed mode S-parameters.

5.3 Coupled Microstrip Pair

We consider a problem of coupled microstrip pair depicted in Fig. 43. For this type

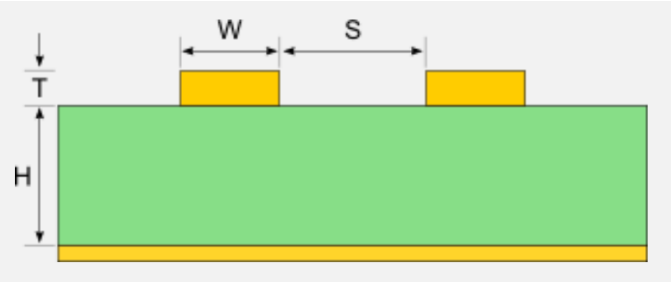

Figure 43: Geometry of coupled microstrips.

of transmission lines we chose relative permittivity $\epsilon_r = 4.5$, substrate thickness $H = 20\,\text{mils}$, conductor thickness $T = 1.3\,\text{mils}$, the width of microstrips w to vary from 0 to 20 mils, and conductor spacing s to vary from 0.01645 to 20 mils. The closed-form formula for approximating single-ended, odd-, and even- mode characteristic impedances Z_{oo} and Z_{oe} which are used in the analysis is from [76].

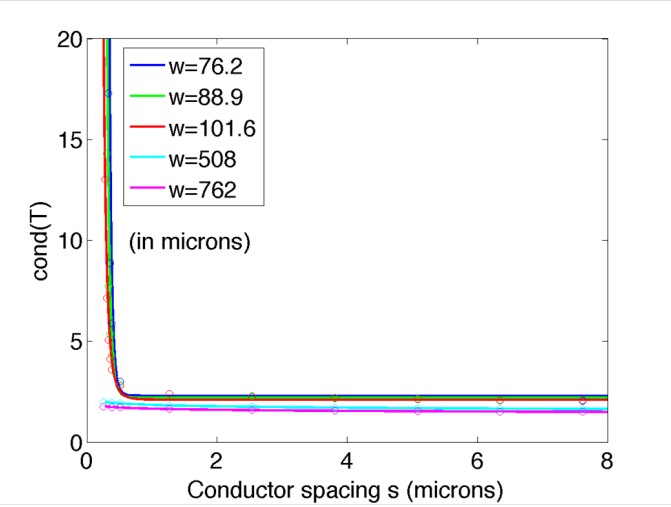

Figure 44: The condition number of matrix T vs conductor spacing s (microns)

The behavior of the condition number of matrix T as a function of spacing s for different (small) values of conductor width w is shown in Fig. 44. Again, the graph shows

that as the differential traces come close to each other, or the spacing s approaches 0, the condition number of T increases, which can affect the accuracy of conversion between single-ended and mixed mode S-parameters. In order to provide a finite element method

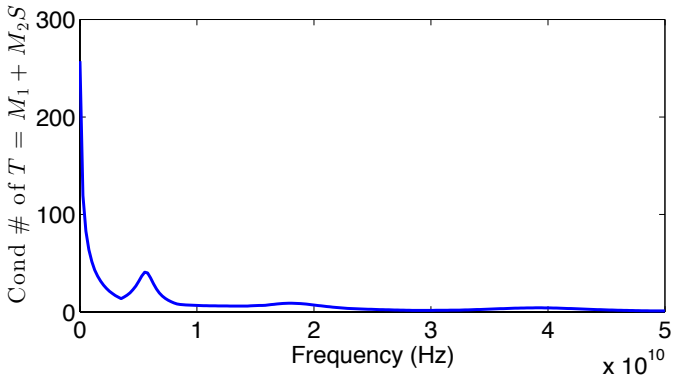

Figure 45: The condition number of matrix T as a function of frequency in microstrips case with $\epsilon_r = 4.5$, $H = 508\mu$m, $T = 33\mu$m, $w = 101.6\mu$m, $s = 0.38\mu$m, $Z_{oo} = 0.00273\Omega$ and $Z_{oe} = 183\Omega$.

(FEM) electro-magnetic (EM) simulation example, the model is simulated using ANSYS HFSS software with the following set of parameters. We have chosen relative permitivity to be $\epsilon_r = 4.5$, substrate thickness $H = 20$ mils, conductor thickness $T = 1.3$ mils, the width of microstrips $w = 4$ mils, and conductor spacing $s = 0.015$ mils. We used the PCB Impedance Calculator offered on *www.eeweb.com* which is based on the work of [76]. We set the odd- and even-mode characteristic impedances to 0.00273 and 183 Ohm, respectively, to obtain single-ended S-parameters. In this case, we get $Z_{oo} = 0.00273$ Ohm and $Z_{oe} = 183$ Ohm. The coupling constants k_{oo} and k_{oe} are computed as

$$k_{0o} = \sqrt{\frac{Z_{0o}}{Z_{0e}}}, \quad k_{0e} = \frac{1}{k_{0o}}.$$

Fig. 45 shows the condition number behavior of conversion matrix T with frequency. The condition number reached the maximum value of 265.57 at the first frequency point. Then we computed the inverse of T to be T^{-1}. After putting a perturbation of 0.001 on S(1,1) and computing the inverse of the new matrix T to be T_{new}^{-1}, , the norm of the difference matrix $(T^{-1}-T_{new}^{-1})$ is 0.9619. This means that, if the accuracy of S-parameters is 0.001, the errors of matrix T can be relatively very large since the magnitude of S-parameters cannot be larger than 1. Fig. 46 show a case for broadside coupled stripline pair. Fig. 47 show the independence on conductor thickness of the condition number.

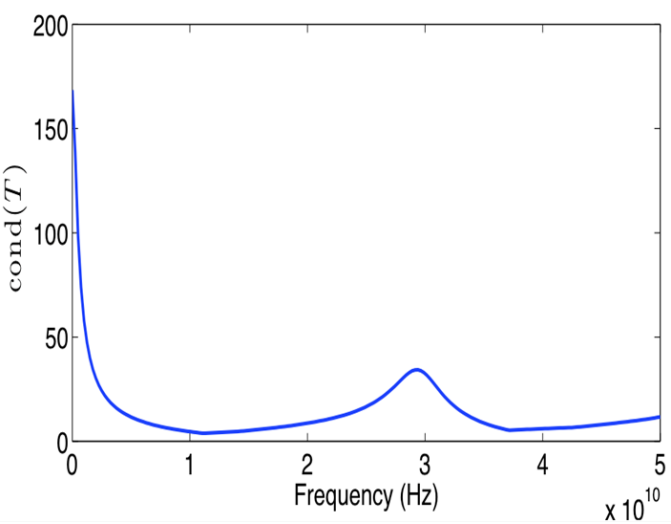

Figure 46: The condition number of matrix T as a function of frequency in broadside coupled striplines case with $\epsilon_r = 4.5$, $H = 330\mu$m, $T = 33\mu$m, $w = 762\mu$m, $s = 0.025\mu$m, $Z_{oo} = 0.00309\Omega$ and $Z_{oe} = 87\Omega$.

The material shown in this section was presented at the 2015 IEEE Workshop on Microelectronics and Electron Devices and published in [77].

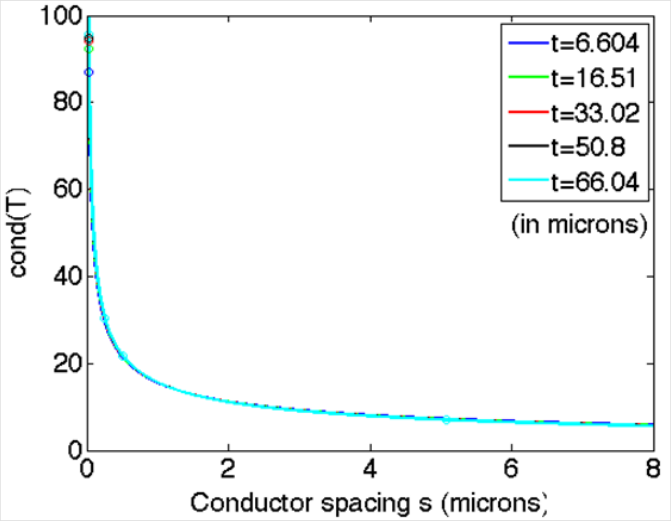

Figure 47: The condition number of matrix T as a function of conductor spacing with different thicknesses.

6 Causality of Single-Ended vs. Converted Mixed-Mode S-Parameters

In this section, we compare accuracy in causality of given single-ended S-parameters with that of corresponding converted mixed-mode S-parameters. We expect that in the case of strong coupling when the condition number of the transformation matrix T is high, conversion is not very accurate, which could affect causality of the converted mixed-mode S-parameters.

We start from reviewing basic concepts of causality for linear time-translation invariant systems and show main steps in derivation of SVD-based causal Fourier continuation method [61]. We then apply this method to check causality of single-ended and converted mixed-mode S-parameters and compare corresponding reconstruction errors.

6.1 Causality of Linear Time-Invariant Systems

Consider a linear and time-invariant physical system with the impulse response $h(t)$. Denote by

$$H(w) = \int_{-\infty}^{\infty} h(\tau)\, \mathrm{e}^{-iw\tau}\, d\tau \tag{8}$$

the Fourier transform of $h(t)$, which is also called the transfer function.

The system is causal if the output cannot precede the input, i.e. if $f(t) = 0$ for $t < T$, the same must be true for $x(t)$. This primitive causality condition in the time domain implies $h(t) = 0$, $t < 0$. Hence, domain of integration in (8) can be reduced to $[0, \infty)$.

For $H(w) \in L_2(\mathbb{R})$, starting from Cauchy's theorem and using contour integration,

one can show [65] that for any point w on the real axis, $H(w)$ can be written as

$$H(w) = \frac{1}{\pi i} \fint_{-\infty}^{\infty} \frac{H(w')}{w - w'} dw', \quad \text{real } w, \tag{9}$$

where

$$\fint_{-\infty}^{\infty} = P \int_{-\infty}^{\infty} = \lim_{\epsilon \to 0} \left(\int_{-\infty}^{w-\epsilon} + \int_{w+\epsilon}^{\infty} \right)$$

denotes Cauchy's principal value. Separating the real and imaginary parts of (9), we get

$$\operatorname{Re} H(w) = \frac{1}{\pi} \fint_{-\infty}^{\infty} \frac{\operatorname{Im} H(w')}{w - w'} dw', \tag{10}$$

$$\operatorname{Im} H(w) = -\frac{1}{\pi} \fint_{-\infty}^{\infty} \frac{\operatorname{Re} H(w')}{w - w'} dw'. \tag{11}$$

These expressions relating $\operatorname{Re} H$ and $\operatorname{Im} H$ are called the dispersion relations or Kramers-Krönig relations. These formulas show that $\operatorname{Re} H$ at one frequency is related to $\operatorname{Im} H$ for all frequencies, and vice versa. Choosing either $\operatorname{Re} H$ or $\operatorname{Im} H$ as an arbitrary square integrable function, then the other one is completely determined by causality. Recalling that the Hilbert transform is defined by

$$\mathcal{H}[u(w)] = \frac{1}{\pi} \fint_{-\infty}^{\infty} \frac{u(w')}{w - w'} dw',$$

we see that $\operatorname{Re} H$ and $\operatorname{Im} H$ are Hilbert transforms of each other, i.e.

$$\operatorname{Re} H(w) = \mathcal{H}[\operatorname{Im} H(w)], \quad \operatorname{Im} H(w) = -\mathcal{H}[\operatorname{Re} H(w)].$$

Dispersion relations are the causality condition in the frequency domain.

An example of a function $H(w)$ that is not square integrable but satisfies the Kramers-Krönig dispersion relations (10), (11) is provided by $H(w) = \mathrm{e}^{-iaw}$, $a > 0$.

The real and imaginary parts are $\cos(aw)$ and $-\sin(aw)$, and dispersion relations (10), (11) can be verified by noting that $\mathcal{H}[\cos(aw)] = \sin(aw)$ and $\mathcal{H}[\sin(aw)] = -\cos(aw)$.

Evaluation of the Hilbert transform requires integration on $(-\infty, \infty)$, which can be reduced to $[0, \infty)$ for real-valued $h(t)$ by spectrum symmetry of $H(w)$. In practice, only a limited number of discrete values of $H(w)$ is available on $[w_{min}, w_{max}]$. Thus, the domain of integration has to be truncated. This usually causes serious boundary artifacts. To reduce the dependence of out-of-band frequency responses, the generalized dispersion relations with subtractions [51] can be used. In recent papers by the authors, an alternative approach was proposed, which required construction of a periodic polynomial [59] or Fourier continuations [61, 60]. This approach was motivated by the above example $H(w) = \mathrm{e}^{-iaw}$, $a > 0$, that is not square integrable but still satisfies the dispersion relations. Using polynomial continuation or Fourier continuation method allows one to significantly reduce or completely remove boundary artifacts caused by the domain truncation, respectively. The techniques can be used for both baseband and bandpass cases and can be extended to multidimensional cases.

6.2 Causal Fourier Continuations

Consider a transfer function $H(w) = \mathrm{Re}\, H + i\, \mathrm{Im}\, H$, whose discrete values are available on $[w_{min}, w_{max}]$, $w_{min} \geq 0$. For real-valued impulse response functions $h(t)$, $\mathrm{Re}\, H$ and $\mathrm{Im}\, H$ are even and odd functions, respectively. This implies that $H(w)$ has values on $[-w_{max}, -w_{min}]$ by spectrum symmetry. For convenience, we rescale the frequency interval $[-w_{max}, w_{max}]$ to $[-0.5, 0.5]$ by the substitution $x = \frac{0.5}{w_{max}} w$, so the rescaled transfer

function $H(x)$ is defined on the unit length interval. Both baseband and bandpass can be considered.

The idea of Fourier continuation is to construct an accurate Fourier series approximation of $H(x)$ by allowing the Fourier series to be periodic and causal in an extended domain. The result is the Fourier continuation of H that we denote by $\mathcal{C}(H)$, and it is defined by

$$\mathcal{C}(H)(x) = \sum_{k=-M+1}^{M} \alpha_k \, \mathrm{e}^{-\frac{2\pi i}{b}kx}, \tag{12}$$

for even number $2M$ of terms, whereas for odd number $2M+1$ of terms, the index k varies from $-M$ to M. Throughout this paper we will consider Fourier series with even number of terms for simplicity. All presented results have analogues for Fourier series with odd number of terms. Here b is the period of approximation. For SVD-based periodic continuations b is normally chosen as twice the length of the domain on which function H is given though the value $b = 2$ is not necessarily optimal. The optimal value b depends on a function being approximated. In practice, several values $b \in (1, 4)$ may be tried to get a better reconstruction of $H(x)$ with a Fourier series.

Functions $\phi_k(x) = \mathrm{e}^{-\frac{2\pi i}{b}kx}$, $k \in \mathbb{Z}$, form a complete orthogonal basis in $L_2[-\frac{b}{2}, \frac{b}{2}]$. Moreover, $\mathcal{H}\{\phi_k(x)\} = i\,\mathrm{sgn}(k)\phi_k(x)$, i.e. functions $\{\phi_k(x)\}$ are the eigenfunctions of the Hilbert transform $\mathcal{H}$ with associated eigenvalues $\pm i$ with $x \in [-\frac{b}{2}, \frac{b}{2}]$. For a causal periodic continuation, we need $\mathrm{Im}\,\mathcal{C}(H)(x)$ to be the Hilbert transform of $-\mathrm{Re}\,\mathcal{C}(H)(x)$. It can be shown [61] that this implies $\alpha_k = 0$ for $k \leq 0$ in (12). Hence, a causal Fourier

continuation has the form

$$\mathcal{C}(H)(x) = \sum_{k=1}^{M} \alpha_k \phi_k(x). \tag{13}$$

Evaluating $H(x)$ at points x_j, $j = 1, \ldots, N$, $x_j \in [-0.5, 0.5]$, produces a complex valued system

$$\mathcal{C}(H)(x_j) = \sum_{k=1}^{M} \alpha_k \phi_k(x_j) \tag{14}$$

with N equations for M unknowns α_k, $k = 1, \ldots, M$, $N \geq M$. If $N > M$, the system (14) is overdetermined and has to be solved in the least squares sense. When Fourier coefficients α_k are computed, formula (13) provides reconstruction of $H(x)$ on $[-0.5, 0.5]$. The least squares problem is extremely ill-conditioned. However, it can be regularized using a truncated SVD method when singular values below some cutoff tolerance ξ close to the machine precision are being discarded. To make ill-conditioning of matrix problem (14) better, more data points N than the Fourier coefficients M should be used. We use at least $N = 2M$ as an effective way to obtain an accurate and reliable approximation of $H(x)$ over the interval $[-0.5, 0.5]$.

Since $\operatorname{Re} H(x)$ and $\operatorname{Im} H(x)$ are even and odd functions of x, respectively, the Fourier coefficients

$$\alpha_k = \frac{1}{b} \int_{-b/2}^{b/2} H(x) \overline{\phi_k(x)} dx, \quad k = 1, \ldots, M,$$

are real. Here $\bar{}$ denotes the complex conjugate. To ensure that numerically computed Fourier coefficients α_k are real, instead of solving complex-valued system (14), one can

separate the real and imaginary parts of $\mathcal{C}(H)(x_j)$ to obtain real-valued system

$$\begin{aligned} \operatorname{Re}\mathcal{C}(H)(x_j) &= \sum_{k=1}^{M} \alpha_k \operatorname{Re}\phi_k(x_j), \\ \operatorname{Im}\mathcal{C}(H)(x_j) &= \sum_{k=1}^{M} \alpha_k \operatorname{Im}\phi_k(x_j). \end{aligned} \tag{15}$$

We show in [61] that real formulation provides slightly more accurate reconstruction than complex.

To access the quality of approximation of $H(x)$ with its causal Fourier series, we introduce reconstruction errors $E_R(x)$ and $E_I(x)$,

$$E_R(x) = \operatorname{Re} H(x) - \operatorname{Re}\mathcal{C}(H)(x), \tag{16}$$

$$E_I(x) = \operatorname{Im} H(x) - \operatorname{Im}\mathcal{C}(H)(x) \tag{17}$$

on the original interval $[-0.5, 0.5]$.

The error analysis performed in [61] shows that the error between $H(x)$ and its causal Fourier continuation $\mathcal{C}(H+\varepsilon)$ under the presence of a noise ε, has the following upper bound:

$$||H - \mathcal{C}(H+\varepsilon)||_{L_2(\Omega)} \leq \epsilon_F + \epsilon_n + \epsilon_T. \tag{18}$$

Here

$$\epsilon_F = (1 + \Lambda_2\sqrt{N(M-K)})||H - \hat{H}_M||_{L_\infty(\Omega)}$$

is the error due to approximation of H with a causal Fourier series and it decays as $\mathcal{O}(M^{-k+1})$, where k is the smoothness order of the transfer function $H(x)$.

$$\epsilon_T = \Lambda_1\sqrt{K/b}||\hat{H}_M||_{L_\infty(\Omega^c)} \tag{19}$$

is the error due to the truncation of singular values and it is typically small and close to the cut-off value ξ. As (19) indicates, ϵ_T depends on b and the function H being approximated.

$$\epsilon_n = (1 + \Lambda_2\sqrt{N(M-K)})||\varepsilon||_{L_\infty(\Omega)}$$

is the error due to the presence of a noise or approximation errors in the given data and it shows a level of causality violation. In practice the size of ϵ_n is close to the size of noise in data.

The error bound (18) shows that the reconstruction errors E_R and E_I decrease first due to the term with ϵ_F as the resolution of data given by the number N of points and the corresponding number M of Fourier coefficients increase until either the level ϵ of a noise or level ϵ_T due to truncation of singular values is reached. If only round-off errors are present in data, the errors will level off at ϵ_T. If reconstruction errors level off at some value $\epsilon > \epsilon_T$ as the resolution increases, the data are declared non-causal with the error approximately at the order of ϵ.

In the next section, we apply the SVD-based causal Fourier continuation method to compare causality accuracy in given single-ended and converted mixed-mode S-parameters.

6.3 Numerical Experiments: Causality Verification

In this section, we analyze a case of broadside coupled striplines with spacing $s = 0.025\mu m$, width $w = 76.2\mu m$. This is an example of a 4-port DUT with strong coupling which yields large errors in conversion. The causality violations of differential

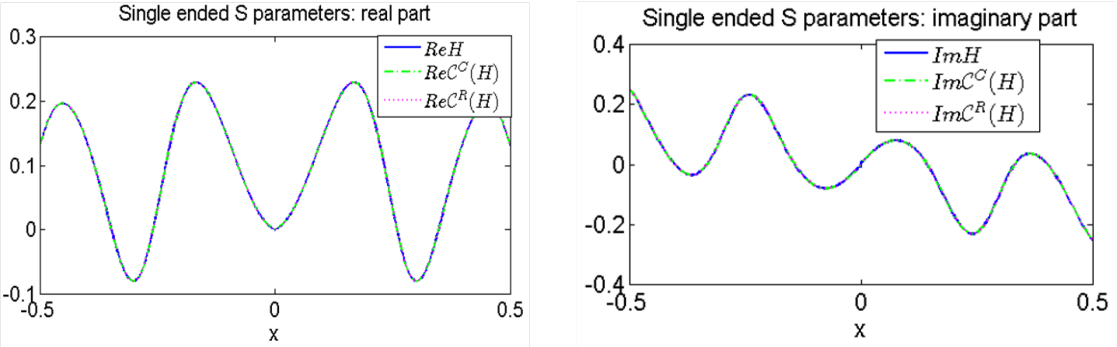

Figure 48: Real and imaginary parts of single-ended S-parameters together with their causal Fourier continuations in the case of broadside coupled striplines with strong coupling with $s = 0.025\mu m$, width $w = 76.2\mu m$.

S-parameters are studied in the case with non-coupling conversion and coupling conversion. Single-ended S-parameters are simulated on $[w_{min}, w_{max}]$ with $w_{min} = 100\,\text{Hz}$ and $w_{max} = 10\,\text{GHz}$ at 200 frequency points. We chose $H(w) = S_{11}(w)$ element to analyze. The real and imaginary parts of rescaled and reflected by spectrum symmetry transfer function $H(x)$, $x \in [-0.5, 0.5]$, corresponding to single-ended S-parameters are shown in Fig. 48. Superimposed are their causal Fourier continuations with $M = 200$ and $b = 2$. Even though $H(x)$ and Fourier continuation $\mathcal{C}(H)$ look indistinguishable in Fig. 48, the actual reconstruction errors E_R and E_I, shown in Fig. 49, are on the order of 10^{-5} except in the area close to DC, where the errors are by almost two orders higher. Large errors around $x = 0$ are due to the fact that the transfer function is not known at $x = 0$ but they decrease when w_{min} becomes smaller and closer at 0 [61]. Therefore, for causality evaluation purposes, we will analyze the reconstruction errors away from $x = 0$.

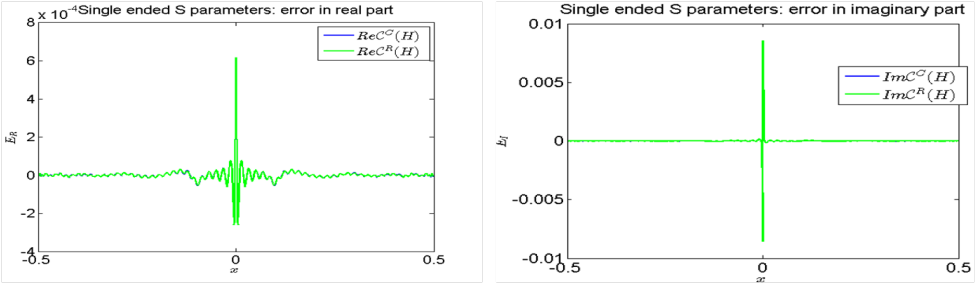

Figure 49: Reconstruction errors E_R and E_I for single-ended S-parameters in the case of broadside coupled striplines with strong coupling with $s = 0.025\mu m$, width $w = 76.2\mu m$.

Next we analyze the order of reconstruction errors in the converted mixed-mode S-parameters. First we use conversion without coupling for which transformation matrix T is orthogonal, thus, we expect accurate numerical conversion. We consider element $H(w) = S_{11}^{(dd)}$. With the same number $M = 200$ of Fourier coefficients and period $b = 2$ of the extended domain, we obtain corresponding causal Fourier continuation. These are depicted in Fig. 50. The corresponding reconstruction errors, shown in Fig. 51, reveal that causality is satisfied within the same accuracy as in single-ended S-parameters though physically the results are not correct since coupling is not taken into account.

In Fig. 52, we show converted mixed-ended S-parameters (element $H = S_{11}^{(dd)}$) computed using the transformation matrix with coupling. Superimposed are their causal Fourier continuations. It is clear that there is large discrepancy between the given transfer function H and its causal Fourier continuation that develops oscillations on the entire domain. The reconstruction errors, shown in Fig. 53, are on the order of 10^{-2} away from $x = 0$ and on the order of 10^{-1} around $x = 0$.

The above results suggest that in the case of strong coupling, conversion from single-

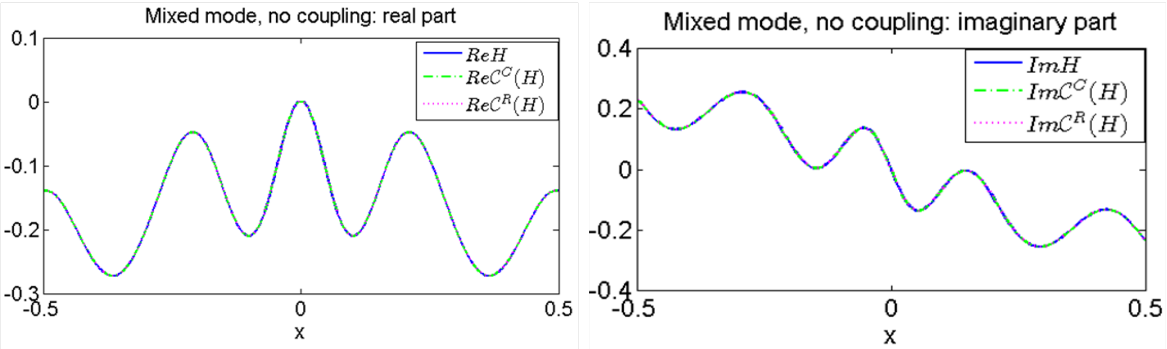

Figure 50: Real and imaginary parts of converted mixed-ended S-parameters (element $S_{11}^{(dd)}$) using non-coupling formula together with their causal Fourier continuations in the case of broadside coupled striplines with strong coupling with $s = 0.025\mu m$, width $w = 76.2\mu m$.

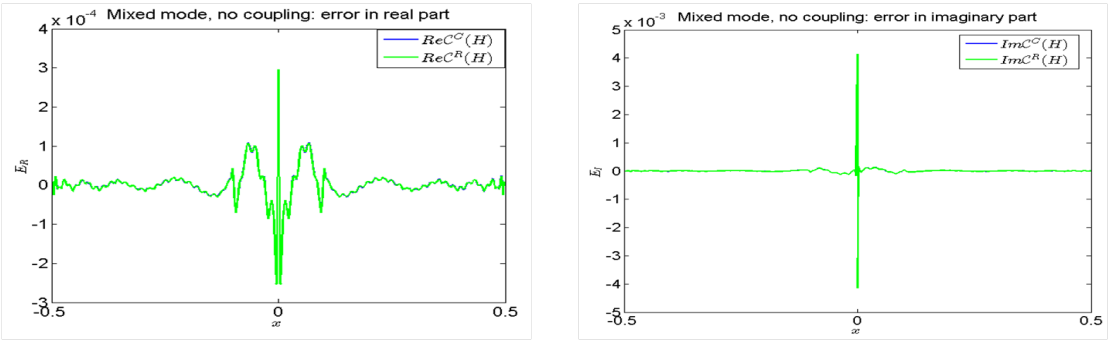

Figure 51: Reconstruction errors E_R and E_I of converted mixed-ended S-parameters (element $S_{11}^{(dd)}$) using non-coupling formula in the case of broadside coupled striplines with strong coupling with $s = 0.025\mu m$, width $w = 76.2\mu m$.

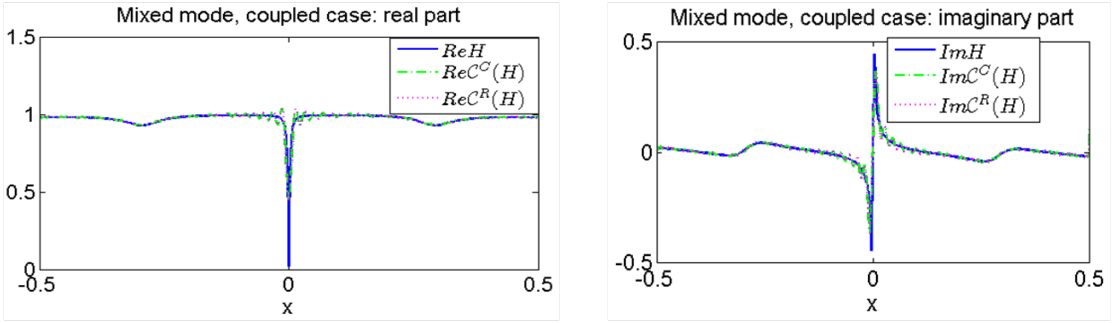

Figure 52: Real and imaginary parts of converted mixed-ended S-parameters (element $S_{11}^{(dd)}$) using coupling formula together with their causal Fourier continuations in the case of broadside coupled striplines with strong coupling with $s = 0.025\mu m$, width $w = 76.2\mu m$.

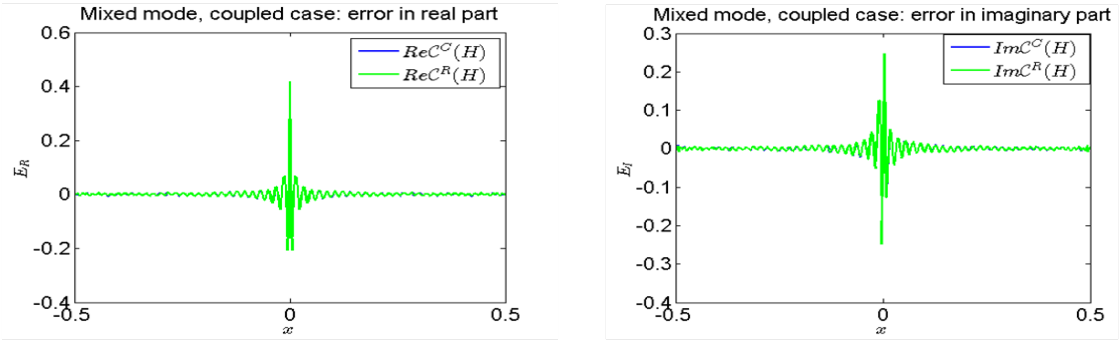

Figure 53: Reconstruction errors E_R and E_I of converted mixed-ended S-parameters (element $S_{11}^{(dd)}$) using non-coupling formula in the case of broadside coupled striplines with strong coupling with $s = 0.025\mu m$, width $w = 76.2\mu m$.

ended to mixed-mode S-parameters should be avoided, and alternative methods for extracting differential S-parameters should be used, for example, direct numerical simulations of mixed-mode S-parameters.

More detailed results [78] from this section will be submitted for publication to the *Journal of Microelectronics and Electronic Packaging*.

7 Direct Simulation of Mixed-Mode S-Parameters

In this section, we present a new technique on how to simulate directly differential S-parameters using true excitations without conversion from single-ended S-parameters. We demonstrate this approach on the example on coupled microstrip lines, where we validate our method in the case of weak coupling and show expected difference between differential S-parameters converted from single-ended S-parameters using no coupling and simulated directly with coupling in the case of strong coupling. We discuss an application of using directly simulated differential S-parameters to modeling of PDNs. This newly proposed approach allows one to correctly characterize PDNs and obtain a good model for SSN estimation.

As discussed in Section 1, PDNs are the sources of switching noise that cause power integrity problems for electronic systems. Traditionally, PDNs usually consist of nets "VCC" and "GND" which are typically characterized using single-ended S-parameters that require a signal or power net as the net under investigation and a reference net which is necessarily a uniform reference plane. For example, for the common structures such as striplines or microstrips, there are always uniform reference planes as "GND" net to be the reference for S-parameters measurement or simulation. But in practice, especially for high I/O density structures, a good "reference plane" hardly exists. Figure 54 shows a typical power planes of a SDRAM and their voltage drop distribution. The regions in red color have the highest voltage drop on the power planes. As we can see from the picture, their shapes are not uniformly rectangles but can be of any possible

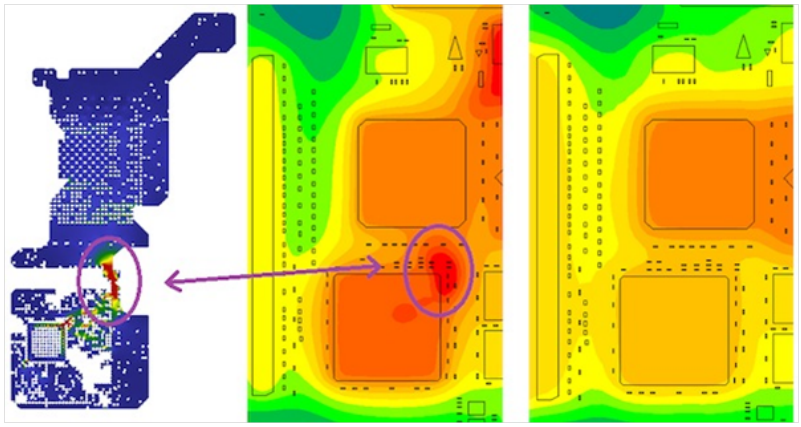

Figure 54: A typical power plane and its voltage drop distribution.

geometry, while a good reference plane has a nearly-uniform voltage distribution.

Since a good reference plane may not exist in an electronic system and single-ended S-parameters require a uniform "GND", there is a certain need to use differential S-parameters between an arbitrarily shaped power plane pair. In terms of simulation and modeling, every model needs to correctly reflect the measurement conditions in order to fully characterize the nets under operating condition, i.e. "VCC" nets usually have positive voltage while "VSS" usually have negative one. Hence, we need to come up with a technique to model the PDNs with true complement excitations using differential S-parameters. Furthermore, as the size of chip packages keeps shrinking down, the spacing between conductors becomes smaller and smaller and hence, the coupling effects become more and more important. This research serves with a knowledge about coupling not only in packaging level but also possibly in chip level because the conductor spacings/widths in silicon are much smaller than that in package or PCB level. Since in most of software tools and literature, mixed-mode S-parameters are usually obtained via

conversion with formulas that do not take into account the coupling effect, we would like to analyze how coupling affects the conversion at different levels of coupling strength.

7.1 Simulation of mixed-mode S-parameters by conversion with and without coupling

Figure 55 shows an 3D-CAD model of edge coupled microstrips which we would like to investigate. We simulated it with ANSYS HFSS 2014 which allows us to simulate the structure with composite excitations. We use a pair of edge coupled microstrips with conductors to be copper with thickness of 1.3 mils, trace widths of 32 mils, substrate of FR-4 with thickness of 20 mils, and dielectric constant of 4.4 at 1GHz. The spacings of striplines have values of 50 mils, 15 mils, and 6 mils. In this part, we built the 3D-CAD models and fabricated them for measurements. We simulated single-ended 4-port S-parameters, then converted into 2-port mixed-mode S-parameters with and without coupling effects taken into account, then compared with the measurements of mixed-mode S-parameters obtained from PNA Network Analyzer. The model number of our PNA is 5225A which allows us to get mixed-mode S-parameters either converted without coupling effects or with true excitations. We used SMAs as probes. Since the SMA measurement is only good up to 1 or 2 GHz, we set the frequency range from DC to 2GHz. Figures below show the acquired results which are also further discussed.

In the next set of figures, we present simulation results of mixed-mode S-parameters converted from single-ended S-parameters using non-coupling and coupling formulas, shown by solid and dashed blue curves, respectively. Measurement results with true ex-

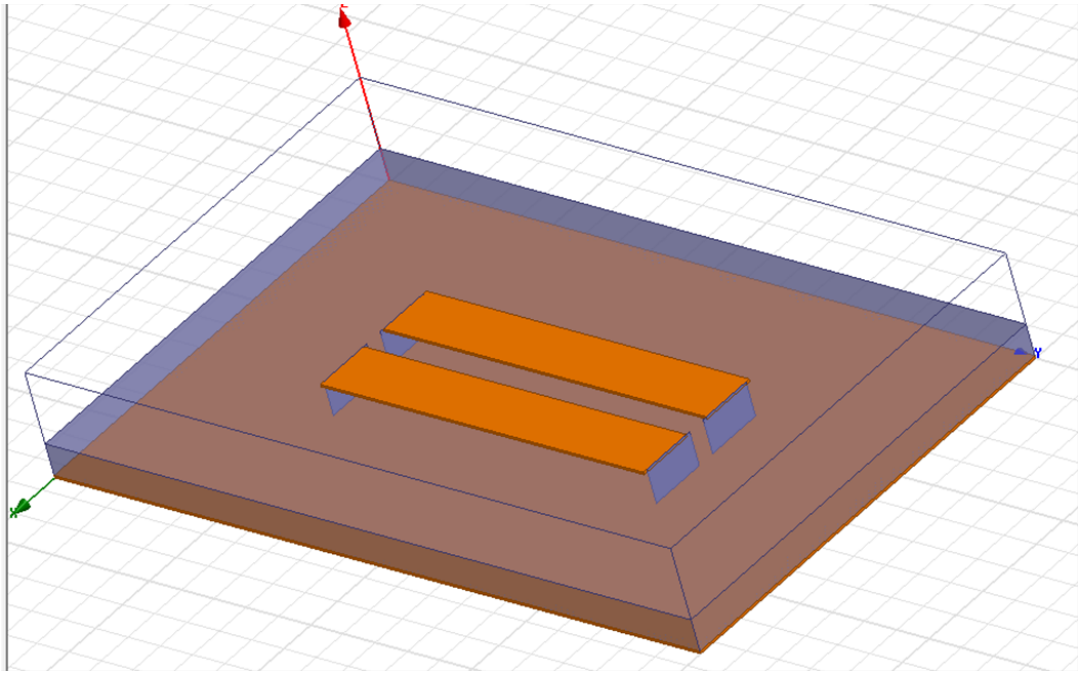

Figure 55: Device under investigation (edge coupled microstrips) with weak coupling in order to verify the method.

citation are depicted using green curves, while the red curves illustrate the measurement results obtained from non-coupling conversion.

Figure 56 shows the simulation and measurement results of the coupled microstrips with conductor spacing of 50 mils, that corresponds to large spacing with weak coupling. The entries of mixed-mode S-parameters being plotted are S_{12}^{cc}, S_{11}^{cc}, S_{11}^{dd}, and S_{12}^{dd}. Since this structure illustrates weak coupling effect, we can observe that the gree and red curves, representing direct measurements with true excitations and measurements obtained in the result on non-coupled conversion, do not deviate a lot from each other. However, the coupling still affects the conversion (solid and dashed blue curves) as we can see that the conversion with coupling effect tend to converge to the measurement

results.

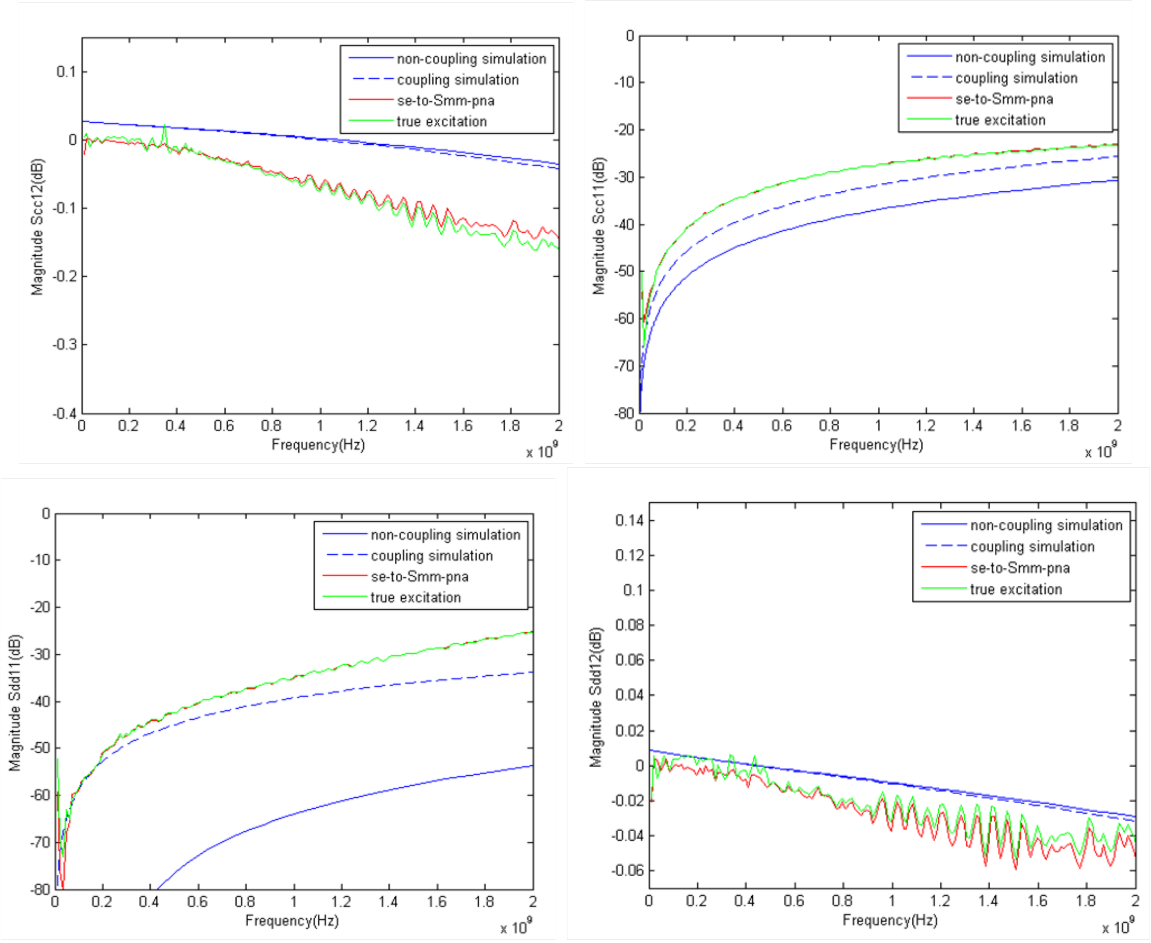

Figure 56: Comparison of simulated and measured mixed-mode S-parameters with large spacing $s = 50$ mils and weak coupling.

Next we reduce the conductor spacing to 15 mils to provide a stronger coupling effect. Figure 57 shows the simulation and measurement results of the coupled microstrips with conductor spacing of 15 mils. The entries of mixed-mode S-parameters being plotted are S_{11}^{dd} and S_{12}^{dd}. This structure illustrates medium coupling effect as we can see that the red and green curves deviate more from each other compared to the previous case

when coupling effect is weak. The effect of coupling affects the conversion (solid and dashed blue curves) more as we can see that the conversion with coupling effect tend to converge to the measurement results. In this case, the dashed curve converge more to measurement result.

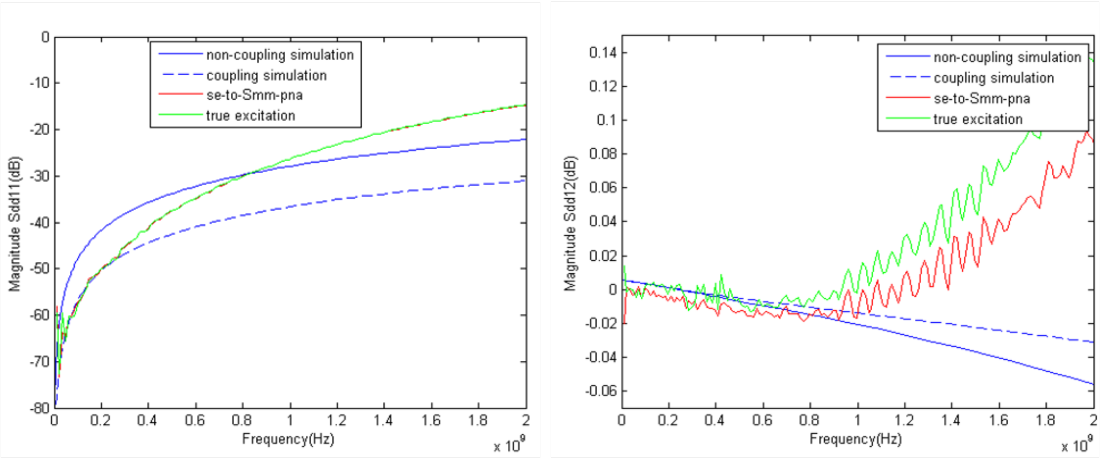

Figure 57: Comparison of simulated and measured mixed-mode S-parameters with moderate spacing $s = 15$ mils and medium coupling.

Finally, lets take a look at Figure 58 illustrating the results of the coupled microstrips with the conductor spacing of 6 mils to provide the strongest coupling effect that we can fabricate. In practice, the smallest spacing and width is around 5 microns at PCB level. In our fabricated board, we chose the minimum spacing/width to be 6 mils not only because it is a common value in industry but also for low price. Figure 58 shows the S_{11}^{cc}, S_{12}^{cc}, S_{11}^{dd}, and S_{12}^{dd} entries of mixed-mode S-parameters. This is a structure illustrating the strongest coupling effect as we can see that the red and green curves deviate the most from each other compare to the other cases when coupling effect is weaker. The

effect of coupling affects the conversion (solid and dashed blue curves) a lot as we can see that the conversion with coupling effect converges more to the measurement results. In this case, the dashed curve converge the most to measurement result.

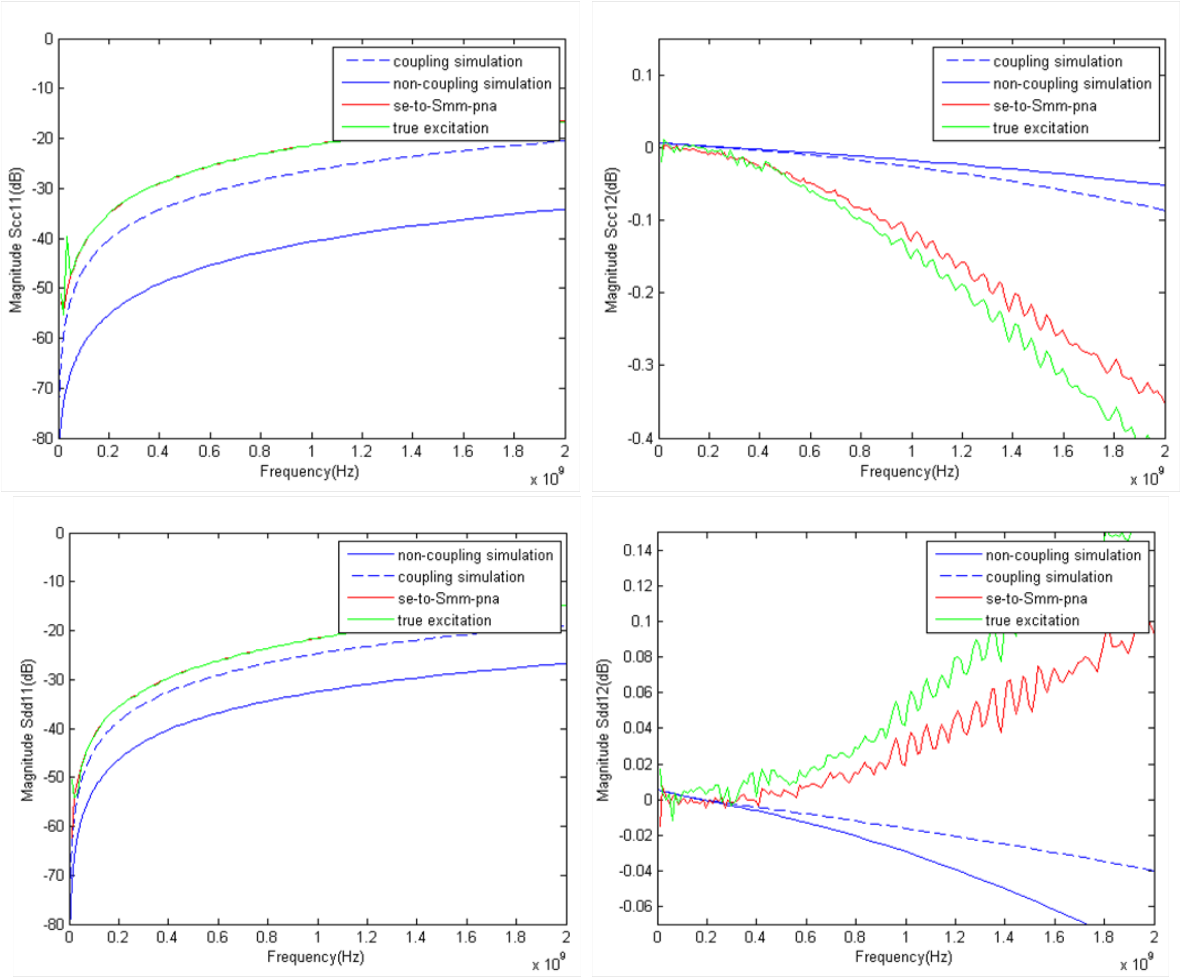

Figure 58: Comparison of simulated and measured mixed-mode S-parameters with small spacing $s = 6$ mils and strong coupling.

Based on the results we acquired, we can conclude that the smaller the conductor spacing is, the more important the coupling formula is. However, there is a difficulty that we need to overcome: for an arbitrarily shaped DUT, saying a PDN, the coupling

coefficients needed to obtain conversion matrices are not known exactly since the spacing between the conductors varies across the entire area. One would need to analyze the coupling coefficient C extracted from S-parameters to avoid errors from different calculators for getting odd- and even-mode characteristic impedances. The converted differential S-parameters should depend only on the single-ended S-parameters.

7.2 Simulation of Mixed-Mode S-Parameters with True Excitations

In this section we discuss how to simulate differential S-parameters directly using true excitations. In most of the EDA software tools and Network Analyzers, mixed-mode S-parameters are obtained with non-coupling conversion. Some measurement machines (Agilent PNA 5225A) can generate two differential wave sources to extract true differential S-parameters. However, none of software tools that we investigated can offer such a direct simulation of differential networks. The software tool ANSYS HFSS version 2014 is the one which can allow us simulate antenna structure with electromagnetic excitations. It also allows us to change multiple excitations by sending a vector to its solver telling it to know that the input waves have been shifted or magnified accordingly to the desire of users. With this tool, we can calculate incident, reflected, or absorbed electromagnetic powers through a port. The software also offers network analysis solutions with the ability to extract single-ended S-parameters with single excitations. However, for the option of composite excitations, we can only get the calculation for powers. My effort to extract mixed-mode S-parameters is through calculating the square-roots of the

power ratio. Unfortunately, only the accepted power can be measured from a port. I could not find a way to get reflected power through an arbitrary port without excitation and thus I will leave this part for future research.

We investigate the structure of edge coupled microstrips as before and set the spacing of the conductors to 50 mils, which provides a weak coupling. We would like to investigate the weak coupling case first because the conversion should not deviate far from the true result. The four rectangles represent the four single-ended ports which will guarantee the DUT to reflect the true operating conditions. In differential networks, the two nets are driven by two complementary sources. Hence, we also need to set 4 single-ended ports to drive the same excitations. The problem left is how to define differential ports as we have defined the single-ended ports before? Based on the literature, the differential ports need to have reference impedance to be 100Ω while single-ended ones refer to 50Ω reference impedance. The single-ended ports have been defined before. If we further defined the differential ports, the model will not reflect the true operating condition and actually has lead to incorrect results. In other words, the port terminated impedances have been changed. To overcome this problem, I have chosen the reference impedance of newly defined differential ports to have very large values, i.e. $5,000,000\Omega$. In practice, we cannot pick larger values because the ill-conditioning will cause the solver to stop. Figure 59 shows the differential insertion loss (S_{12}^{dd}). The idea is the same with the case when you attach a very high impedance shunt into a network which will not change the behavior of the circuit since an open circuit does not change anything to the device.

As we can see from the results shown in Fig. 59, the coupling and non-coupling formulas give results very close to each other, as expected, and the simulation result (green curve) gives a very good agreement to the converted results. The error is of course non-zero since there is always a deviation from conversion compared to the true result, but the error is small. Furthermore, the solver calculates powers through the calculated E and H fields, while single-ended S-parameters may result from calculating voltages and current which require one more step of computation of integrals having another approximation error. Again, due to the low quality of SMAs, the measurement results have large errors at GHz range but give a good agreement at low frequencies.

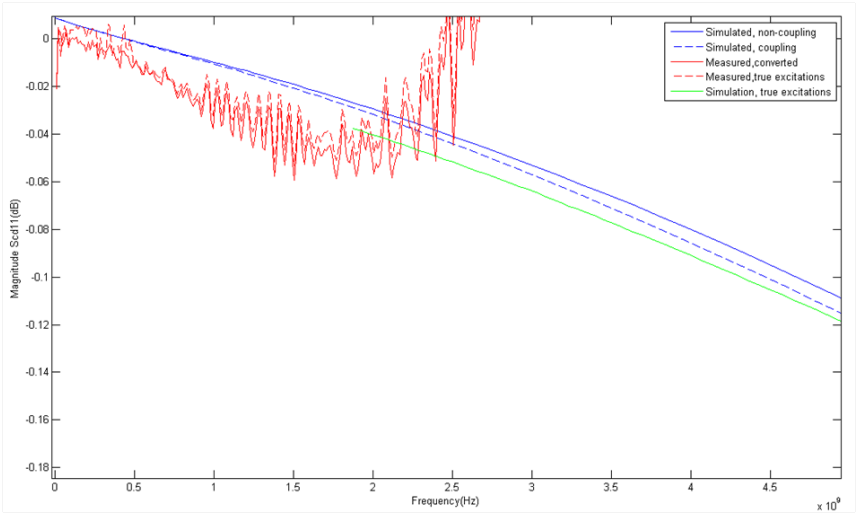

Figure 59: Simulation of differential S-parameters with true excitations.

7.3 Application: Simulation of PDNs Using Differential S-Parameters

The method of direct simulations of differential S-parameters using true excitations described above can be used to model PDNs. In order to do this, one needs to find a common conductor employed as a reference plane for the single-ended ports as shown in Figure 60. Usually one can pick "GND" as the common reference to simulate the PDN consisting of "VCC" and "VSS" power nets which contain complementary voltages.

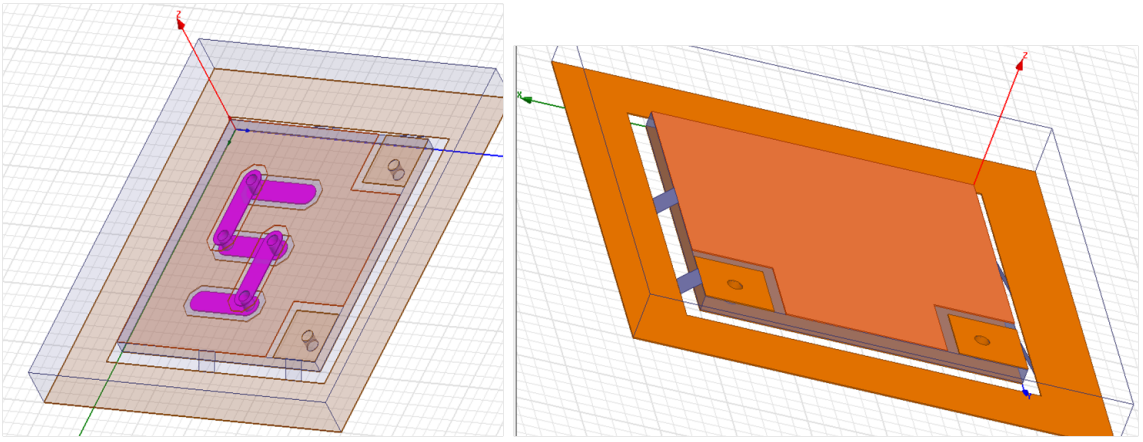

Figure 60: Simulation of differential S-parameters for PDNs: a common conductor employed as a reference plane for the single-ended ports.

8 Time Delay Estimation Using SVD-Based Causal Fourier Continuations

The above approach for causality assessment can be transformed into a delay estimation algorithm by observing the following. Suppose that $h(t)$ is non-zero only from time $T_0 \geq 0$, and we would like to identify the time delay T_0. Consider the Fourier transform $H(w)$ of $h(t)$:

$$H(w) = \int_{t=T_0}^{\infty} \mathrm{e}^{-iwt}\, h(t)dt = \int_{t=T_0}^{\infty} \mathrm{e}^{-i\frac{x}{a}t}\, h(t)dt$$

where we used the substitution $x = aw$, $a = \frac{0.5}{w_{max}}$. Introducing $\tau = \frac{t}{a}$ and employing $u = \tau - \frac{T_0}{a}$, we obtain

$$H(w) = a\,\mathrm{e}^{-ix\frac{T_0}{a}} \int_0^{\infty} \mathrm{e}^{-ixt}\, h(T_0 + au)du = a\,\mathrm{e}^{-ix\frac{T_0}{a}}\, G(x),$$

where $G(x)$ is the Fourier transform of a causal function with no time delay. This implies that when $0 \leq T \leq T_0$, the transfer function $H(x)\,\mathrm{e}^{ix\frac{T}{a}}$ is causal, but when $T \geq T_0$, the transfer function $H(x)\,\mathrm{e}^{ix\frac{T}{a}}$ has a non-causal component. Therefore, $\tilde{T}_0 = T_0/a$ is the time delay for $H(x)$, and the delay T_0 for the original function $H(w)$ is recovered by multiplying $\tilde{T}_0$ by a. Since one can add any integral multiple of 2π to T/a, it is enough to restrict our investigations to the interval $T/a \leq T_{max} = \frac{2\pi}{a\,w_{max}} = 4\pi$. Then for each potential time delay $0 \leq T/a \leq T_{max}$, we solve the following modified system

$$\sum_{k=1}^{M} \alpha_k\, \mathrm{e}^{-\frac{2\pi i}{b}kx_j} = \mathrm{e}^{ix_j\frac{T}{a}}\, H(x_j), \quad j = 1, \ldots, N. \tag{20}$$

For $T < T_0$, the reconstruction errors E_R, E_I should be small and approximately of the same order. As T increases and becomes greater than T_0, the reconstruction errors

should grow indicating non-causal behavior. This contribution extends work [45] to more general than square integrable transfer functions. Moreover, we use a different causality measure than in [45].

Next, we apply a proposed technique to several analytic and simulated examples when the time delay is either known exactly or can be estimated using other techniques. We also consider the effect of noise presence on the accuracy of timed delay estimation.

8.1 Two-Pole Example

The two-pole transfer function with time delay T_0 [45] is defined by $H(w) = \mathrm{e}^{-iwT_0}\left(\frac{r}{iw+s} + \frac{\overline{r}}{iw+\overline{s}}\right)$ where $r = 1+3i$, $s = 1+2i$, $T_0 = 0.25$. We sample data on the interval from $w = 0$ to $w_{max} = 4$ and use various values of M ranging from 20 to 800. The evolution of $||E_R||\infty$ is shown in Fig. 61. Results for $||E_I||\infty$ are similar. As the number M of Fourier coefficients increases, the error E_R decreases until

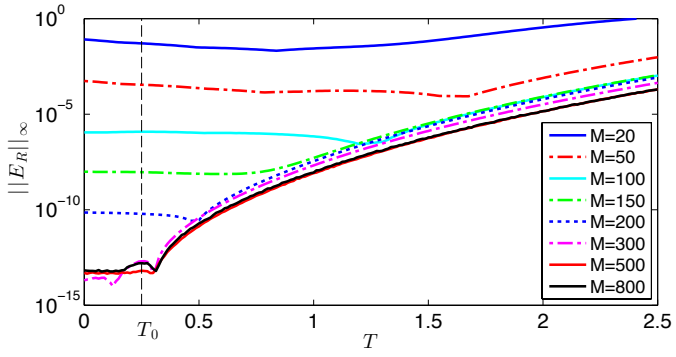

Figure 61: $||E_R||_\infty$ in the two-pole example as M varies. Vertical dashed line indicates the time delay $T_0 = 0.25$.

the level close to machine precision is reached. For each M, as T increases, the er-

rors first are small and about of the same order until a critical time close to T_0 is approached. After that the errors grow approximately as a power function on the loglog scale. Critical times of transition of the error from a plateau region to a growth region are different for each M, decrease as the resolution increases and approach T_0. The goal is to estimate their limit T_0. A typical error curve (the loglog plot is shown) with $M = 300$ with its quadratic fit are depicted in Fig. 62. Specifically, we assume that

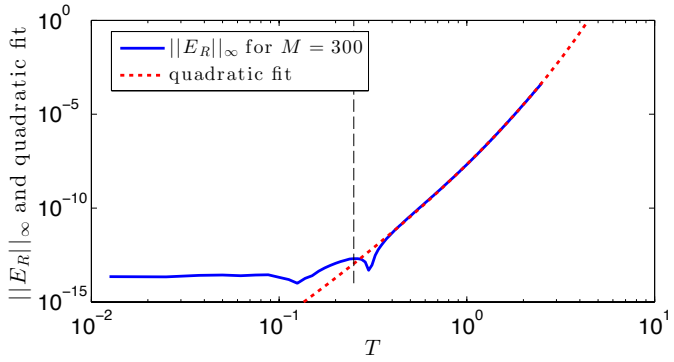

Figure 62: $||E_R||_\infty$ in the two-pole example with $M = 300$ together with its quadratic fit. Vertical dashed line indicates the exact time delay $T_0 = 0.25$.

$\ln T = a_2 (\ln ||E_R||_\infty)^2 + a_1 \ln ||E_R||_\infty + a_0 \equiv f(\ln ||E_R||_\infty)$, where coefficients a_0, a_1, and a_2 are to be determined in the least squares sense. The resulting quadratic function $f(\ln ||E_R||_\infty)$ is then evaluated at the value of $||E_R||_\infty$ at $T = 0$ that is assumed to be the most "causal" time. This procedure produces an estimate of the time delay (critical transition times) for a given M. Approximations of T_0 for $M \geq 200$ are presented in Table 6. The results indicate that the approximations become more accurate as M increases. The error with $M = 700$ and 800 is less than 1%. One can clearly see that the critical times converge to the value close to $T_0 = 0.25$ as M increases. A reasonable

approximation of T_0 is achieved even at $M = 300$ or $N = 150$. This is important since in practice the number N of samples of the transfer function $H(w)$ is usually limited.

M	T_0 estimate	M	T_0 estimate
200	0.5296	500	0.2617
250	0.3139	600	0.2474
300	0.2016	700	0.2478
400	0.2164	800	0.2514

Table 6: Approximations of T_0 for various M in the two-pole example. The exact value $T_0 = 0.25$.

We also consider the effect of noise on the time delay estimation. We impose a cosine perturbation $a\cos(20\pi x)$ of various amplitudes that we add to $\mathrm{Re}\, H$, while keeping $\mathrm{Im}\, H$ unchanged. We set $N = 500$, $b = 4$ and vary a from 10^{-10} to 10^{-3}. The error E_R with no perturbation for early times $T < T_0$ is of the order of 10^{-13}, that corresponds to the level of filtering of singular values. When the perturbation is added, the errors for $T < T_0$ are higher and approximately of the order of a. For $T > T_0$, E_R grow at the same rate and coincide almost perfectly with each other. This observation suggests that the proposed approach can also be used in the cases with noise, which is typical in real-life applications. In this case, the fitted curved can be extrapolated and their intersection with the threshold level ξ can be used for time delay estimation as demonstrated in the next example.

8.2 Transmission Line Example

We consider a uniform transmission line segment with the following per-unit-length parameters: $L = 4.73$ nH/cm, $C = 3.8$ pF/cm, $R = 0.8\ \Omega$/cm, $G = 0$ and length $\mathcal{L} = 10$ cm. The frequency is sampled on the interval $(0, 1.0]$ GHz. The scattering matrix of the structure is computed using Matlab function `rlgc2s` and the element $H(w) = S_{11}(w)$ is considered. The time delay $T_0 = 1.25\,\text{ns}$ is imposed by multiplying $H(w)$ by $\exp(-iwT_0)$. The results of time delay estimation are shown in Fig. 63, showing an excellent agreement with the exact time delay.

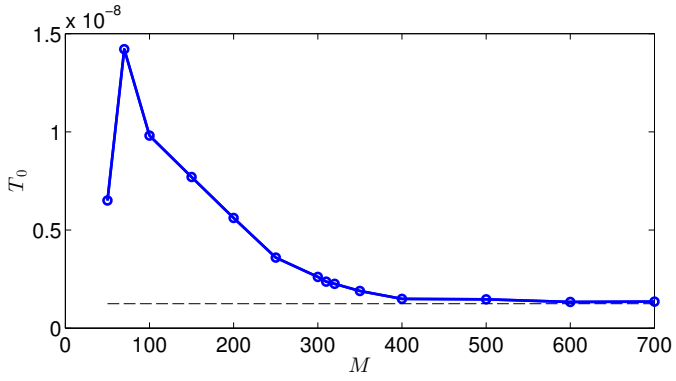

Figure 63: Estimation of the delay time in the transmission line example as M varies. The dashed line corresponds to the exact delay $T_0 = 1.25\,\text{ns}$.

High resolution data may not be available in practice and an alternative approach can be used to estimate the time delay by using quadratic fit(s) of $||E_R||_\infty$ described above and finding their intersection(s) with a limiting error that we take equal to the tolerance $\xi = 10^{-13}$ in filtering of singular values. The results of this procedure are shown in Fig. 64 for three moderate values of $M = 150$, 200 and 400. The corresponding time delay

estimations are 1.2821, 1.2613, 1.2538 ns, respectively.

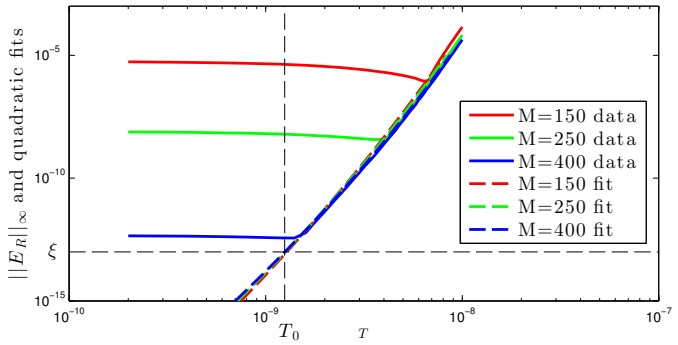

Figure 64: $||E_R||_\infty$ in the transmission line example with $M = 150$, 200 and 400 together with their quadratic fits. Vertical dashed line indicates the exact time delay $T_0 = 1.25$ ns, while horizontal dashed line indicates the level of filtering of singular values given by $\xi = 10^{-13}$.

8.3 Stripline Example

We simulated an asymmetric stripline modeled in [1] with length $L = 8$ in, width $W = 14$ mils, distances from the trace to reference planes $H_1 = 10$ mils, $H_2 = 20$ mils, substrate dielectric Megtron6-1035, Laminate with a dielectric constant $\epsilon_r = 3.45$ using a Cadence software tool with FEM full-wave field solver. The stripline was simulated on $[0, w_{max}]$ with $w_{max} = 2$ GHz. We analyzed element $H(w) = S_{11}(w)$ of the transfer matrix. The real and imaginary parts of H are shown in Figs 65.

The evolution of $||E_R||_\infty$ for various M is depicted in Fig. 66. Even for high values of M, the error in causality does not go to machine precision and instead levels off around 10^{-6}. This indicates that our finite element simulations are accurate only within

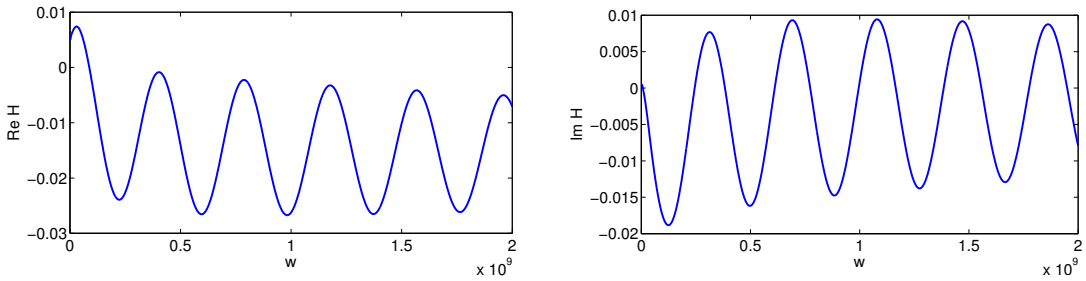

Figure 65: $\mathrm{Re}\, H$ and $\mathrm{Im}\, H$ in the stripline example with $N = 1000$.

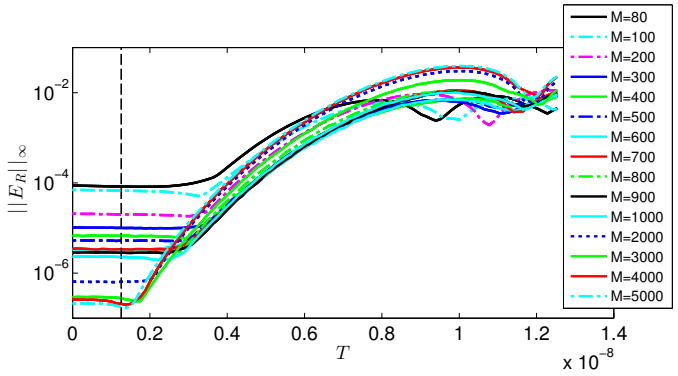

Figure 66: $||E_R||_\infty$ in the stripline example for various M. Vertical dashed line indicates the close form microwave theory time delay approximation $T_0 = 1.25809\,\mathrm{ns}$.

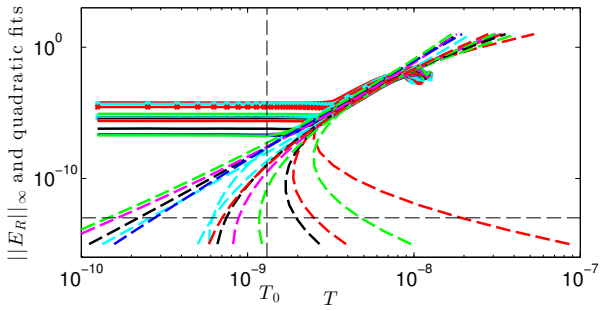

Figure 67: Extrapolated quadratic curves based on initial fitting range in the stripline example.

$10^{-7} - 10^{-6}$. For causality characterization, this implies that data have noise/error with amplitude around $10^{-7} - 10^{-6}$. Graphs of $||E_R||_\infty$ suggest that for $M \leq 2000$, the error is dominated by Fourier series approximation error, while for higher of M, the error dominated by the noise/approximation errors from the finite element method.

In this example, the time delay was estimated using a closed form microwave theory approximation as $T_0 = 8 \times 0.0254/(c_0/\sqrt{(}\epsilon_r) = 1.25809\,\text{ns}$, where $c_0 = 3 \times 10^8 \text{m/s}$ is the speed of light, 0.0254 is a conversion factor to convert from in to m. The error curves were fitted to quadratic curves as explained above. Because of relatively high noise in data, the fitted region is not long enough and transition regions from error being small and flat to growing regions as well as more nonlinear behavior of the error for high values of T make it difficult to estimate the time delay as shown in Fig. 67. As can be seen, extrapolated quadratic curves do not focus at T_0 but instead spread out around T_0. This problem can be corrected by decreasing the fitting range and going more away from transition regions. The results are shown in Fig. 68. Averaging obtained approximations

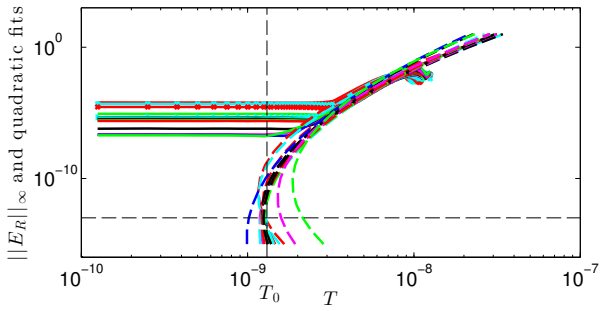

Figure 68: Extrapolated quadratic curves based on more narrow fitting range in the stripline example. The average time delay is $T_0^{(aver)} = 1.2669\,\text{ns}$.

of T_0, we obtain $T_0^{(aver)} = 1.2669\,\text{ns}$, that agrees well with an analytically estimated time delay using a closed form formula.

Preliminary study [77] from this section has been accepted for oral presentation at 2015 IEEE 24th Conference on Electrical Performance of Electronic Packaging and Systems, Oct. 25-28, 2015, in San Jose, California. More detailed analysis [79] will be submitted for publication to the *Journal of Microelectronics and Electronic Packaging*.

9 Conclusions

Differential signaling is a signal transmission method where a transmitting signal is sent in pairs with the same amplitude but with mutually opposite phases. The main advantage of the differential signaling is that any introduced noise equally affects both differential transmission lines if the two lines are tightly coupled together. Since only the difference between the lines is considered, the introduced common-mode noise can be rejected at the receiver device. However, due to manufacturing imperfections, signal unbalance will occur resulting in that the energy will convert from differential-mode to common-mode and vice versa, which is known as cross-mode conversion. To damp the common-mode currents, a common-mode choke can be used (without any noticeable effect on the differential currents) to prevent radiated emissions from the differential lines. To produce the electrical field strength from microamperes of common-mode current, milliamperes of differential current are needed. Moreover, the generated electric and magnetic fields from a differential line pair are more localized compared to those from single-ended lines. Owing to the ability of noise rejection, the signal swing can be decreased compared to a single-ended design and thereby the power can be saved. When the signal on one line is independent of the signal on the adjacent line, i.e., an uncoupled differential pair, the structure does not utilize the full potential of a differential design. To fully utilize the differential design, it is beneficial to start by minimizing the spacing between two lines to create the coupling as strong as possible. Thereafter, the conductors width is adjusted to obtain the desired differential impedance. By doing this, the coupling between the differential line pair is maximized to give a better common-

mode rejection.

We find that the conversion from single-ended to mixed-mode S-parameters may suffer from numerical ill-conditioning. We study the condition number of the conversion matrix for two test cases: broadside coupled striplines and edge coupled microstrips and find that ill-conditioning increases significantly as coupling increases, which results in inaccurate conversion. We employ the SVD-based causal Fourier continuation method to study loss of causality during conversion. When strong coupling is present, we observe higher error in causality of converted mixed-mode S-parameters compared to the one of original single-ended S-parameters.

We also develop a way to simulate differential S-parameters directly using true excitations and apply it to characterizing the power distribution networks, whose characterization by single-ended S-parameters is not appropriate because of ground bounce and IR drop.

We propose a new method for time delay extraction based on the causality argument. We modify the SVD-based causal Fourier continuation method by incorporating the linear varying phase factor to the system of equations that defines Fourier coefficients. We test the method on several analytic and simulated example for which time delay is either known exactly or can be estimated using alternative approaches. The method can be applied to both single-ended and mixed-mode S-parameters.

References

[1] C. Wang, J. L. Drewniak, J. Fan, J. L. Knighten, N. W. Smith, and R. Alexander, "Transmission line modeling of vias in differential signals," in *2002 IEEE International Symposium on Electromagnetic Compatibility*, 2002, pp. 249–252.

[2] H. Y. Sing, "Hybrid lumped-element microstrip filters," *University of Tunku Abdul Rahman*, p. 68, 2012.

[3] D. Seraphim and I. Feinberg, "Electronic Packaging evolution in IBM," *IBM Journal of R&D*, vol. 25, no. 5, pp. 617–630, 1981.

[4] A. Wagiman, "Miniaturization innovation evolution of electronics packaging - what is coming next...?" *34th IEEE/CPMT International, IEMT*, 2010.

[5] E. Perkto, S. Ray, T. Wassick, and H. Stoller, "Evolution of Engineering Change and Repair Technology in High Performance Multichip Modules at IBM," *IEEE Tran. on Advanced Packaging*, vol. 22, no. 2, pp. 129–135, May 1999.

[6] R. Howard, "Optimization of indium-lead alloys for controlled collapse chip connection application," *IBM Journal of R&D*, pp. 372–378, May 1982.

[7] R. Patti, "Three-dimensional integrated circuits and future of system-on-chip designs," *Proc. of the IEEE*, vol. 94, no. 6, pp. 1214–1224, 2006.

[8] K. Zoschke and J. Wolf, "Tsv silicon interposer technology for 3d wafer level system integration - technological milestones and challenges," in *30th Tokyo OHKA Seminar, Tokyo, Japan*, P. Philippov, Ed., 2009, pp. 31–53.

[9] Z. Xu and J.-Q. Lu, "Three-dimensional coaxial through-silicon-via (TSV) design," *IEEE Electron Devices Lett.*, vol. 33, no. 10, pp. 1441–1443, Oct. 2012.

[10] J. e. a. Kim, "High-frequency scalable electrical model and analysis of a through silicon via (TSV)," *IEEE Trans. Comp. Packag. Manufact. Technol.*, vol. 1, no. 2, pp. 181–195, Feb. 2011.

[11] T. Granberg, *Handbook of Digital Techniques for High-Speed Design: Design Examples, Signaling and Memory Technologies, Fiber Optics, Modeling, and Simulation to Ensure Signal Integrity.* Prentice Hall, 2004.

[12] M. Swaminathan and E. Engin, *Power Integrity Modeling and Design for Semiconductors and Systems.* Prentice Hall, 2007.

[13] E. Bogatin, *Signal and Power Integrity - Simplified.* Prentice Hall, 2009.

[14] A. C. Scogna, A. Orlandi, and V. Ricchiuti, "Signal and Power Integrity Analysis of Differential Lines in Multilayer Printed Circuit Boards With Embedded Electromagnetic Bandgap Structures," *IEEE Trans Electromagn Compat*, vol. 52, no. 2, pp. 357–364, 2010.

[15] T.-L. Wu, H.-H. Chuang, and T.-K. Wang, "Overview of Power Integrity Solutions on Package and PCB: Decoupling and EBG Isolation," *IEEE Trans Electromagn Compat*, vol. 52, no. 2, pp. 346–356, 2010.

[16] Z. Liu, S. Sun, and P. Boyle, "FPGA Core PDN Design Optimization," in *2011 IEEE International Symposium On Electromagnetic Compatibility (EMC)*, ser. IEEE In-

ternational Symposium on Electromagnetic Compatibility, 2011, pp. 411–416, IEEE International Symposium on Electromagnetic Compatibility (ISEMC), Long Beach, CA, Aug 14-19, 2011.

[17] F. Carrió, V. González, and E. Sanchis, "Basic concepts of power distribution network design for high-speed transmission," *The Open Optics Journal*, vol. 5, no. (Suppl 1-M8), pp. 51–61, 2011.

[18] W. Beyene, C. Yuan, J. H. Kim, and M. Swaminathan, "Modeling and analysis of power distribution networks for gigabit applications," in *4th International Symposium On Quality Electronic Design, Proceedings*, Kawada, S, Ed., 2003, pp. 235–240, 4th IEEE International Symposium on Quality Electronic Design, San Jose, CA, Mar 24-26, 2003.

[19] C. Golovanov, "Keep the noise down," *ANSYS Advantage*, vol. 8, no. 2, pp. 40–42, 2014.

[20] D. E. Bockelman and W. R. Eisenstadt, "Combined Differential And Common-Mode Scattering Parameters - Theory And Simulation," *IEEE Trans. Microw. Theory Techn.*, vol. 43, no. 7, pp. 1530–1539, 1995.

[21] ——, "Pure-mode network analyzer for on-wafer measurements of mixed-mode S-parameters of differential circuits," *IEEE Trans. Microw. Theory Techn.*, vol. 45, no. 7, pp. 1071–1077, 1997.

[22] A. Huynh, P. Hakansson, and S. Gong, "Mixed-mode s-parameter conversion for networks with coupled differential signals," in *IEEE 37th European Microwave Conference*. IEEE, 2007, pp. 238–241.

[23] ——, "Mixed-mode s-parameters and conversion techniques," in *Advanced Microwave Circuits and Systems*. InTech, 2010, available from: http://www.intechopen.com/books/advanced-microwave-circuits-and-systems/mixed-mode-s-parameters-and-conversion-techniques.

[24] K. Vaz and M. Caggiano, "Measurement technique for the extraction of differential s-parameters from single-ended s-parameters," in *27th International Spring Seminar on Electronics Technology, Books 1-3, Conference Proceedings: Meeting The Challenges Of Electronics Technology Progress*, Philippov, P, Ed., 2004, pp. 313–317, 27th International Spring Seminar on Electronics Technology, Sofia, BULGARIA, MAY 13-16, 2004.

[25] A. Ferrero and M. Pirola, "Generalized mixed-mode S-parameters," *IEEE Trans Microw Theory Techn*, vol. 54, no. 1, pp. 458–463, 2006.

[26] D. M. Garcia-Mora, M. A. Tlaxcalteco-Matus, R. Torres-Torres, G. Hernandez-Sosa, and O. M. Becerra-Fuentes, "Reducing glitches when reconstructing four-port S-parameters of differential transmission lines from two-port measurements," *Microwave And Optical Technology Letters*, vol. 56, no. 10, pp. 2257–2260, 2014.

[27] P. C. Hansen, *Rank-Deficient and Discrete Ill-Posed Problems: Numerical Aspects of Linear Inversion*. SIAM, 1987.

[28] B. Gustavsen and A. Semlyen, "Rational approximation of frequency domain responses by vector fitting," *IEEE Trans. Trans. Power Delivery*, vol. 14, no. 3, pp. 1052–1061, 1999.

[29] D. Deschrijver, B. Haegeman, and T. Dhaene, "Orthonormal vector fitting: A robust macromodeling tool for rational approximation of frequency domain responses," *IEEE Trans. Adv. Packag.*, vol. 30, no. 2, pp. 216–225, 2007.

[30] A. Charest, R. Achar, M. Nakhla, and I. Erdin, "Delay extraction-based passive macromodeling techniques for transmission line type interconnects characterized by tabulated multiport data," *Analog Integr. Circ. S.*, vol. 60, no. 1–2, pp. 13–25, 2009, 50th Midwest Symposium on Circuits and Systems, Montreal, CANADA, SEP 05-AUG 08, 2007-2008.

[31] P. Triverio, S. Grivet-Talocia, M. S. Nakhla, F. G. Canavero, and R. Achar, "Stability, causality, and passivity in electrical interconnect models," *IEEE Trans. Adv. Packag.*, vol. 30, no. 4, pp. 795–808, 2007.

[32] A. V. Oppenheim and R. W. Schafer, *Discrete-Time Signal Processing*, ser. Prentice-Hall Signal Processing Series. Prentice Hall, 1989.

[33] J.-F. Blais, M. Cimmino, A. Ross, and D. Granger, "Suppression of time aliasing in the solution of the equations of motion of an impacted beam with partial constrained layer damping," *J. Sound Vib.*, vol. 326, no. 3-5, pp. 870–882, 2009.

[34] D. Granger and A. Ross, "Effects of partial constrained viscoelastic layer damping parameters on the initial transient response of impacted cantilever beams: Experimental and numerical results," *J. Sound Vib.*, vol. 321, no. 1–2, pp. 45–64, 2009.

[35] D. Gottlieb and C.-W. Shu, "On the Gibbs phenomenon and its resolution," *SIAM Rev.*, vol. 39, no. 4, pp. 644–668, 1997.

[36] A. Gelb and J. Tanner, "Robust reprojection methods for the resolution of the Gibbs phenomenon," *Appl. Comput. Harmon. Anal.*, vol. 20, no. 1, pp. 3–25, 2006.

[37] E. Tadmor, "Filters, mollifiers and the computation of the Gibbs phenomenon," *Acta Numer.*, vol. 16, pp. 305–378, 2007.

[38] H. Mhaskar and J. Prestin, "Polynomial operators for spectral approximation of piecewise analytic functions," *Appl. Comput. Harmon. Anal.*, vol. 26, pp. 121–142, 2009.

[39] G. Beylkin and L. Monzón, "Nonlinear inversion of a band-limited Fourier transform," *Appl. Comput. Harmon. Anal.*, vol. 27, pp. 351–366, 2009.

[40] H. A. Kramers, "La diffusion de la lumiere par les atomes," *Atti Cong. Intern. Fisica (Transactions of Volta Centenary Congress) Como*, vol. 2, pp. 545–557, 1927.

[41] R. D. L. Kronig, "On the theory of dispersion of x-rays," *J. Opt. Soc. Am.*, vol. 12, no. 6, pp. 547–557, 1926.

[42] E. A. Guillemin, *Synthesis of Passive Networks: Theory and Methods Appropriate to the Realization and Approximation Problems.* New York: R. E. Krieger, 1977.

[43] S. Amari, M. Gimersky, and J. Bornemann, "Imaginary part of antennas admittance from its real part using Bodes integrals," *IEEE Trans. Antennas Propag.*, vol. 43, no. 2, pp. 220–223, 1995.

[44] F. M. Tesche, "On the use of the Hilbert transform for processing measured CW data," *IEEE Trans. Electromagn. Compat.*, vol. 34, no. 3, 1, pp. 259–266, 1992.

[45] L. Knockaert and T. Dhaene, "Causality determination and time delay extraction by means of the eigenfunctions of the Hilbert transform," in *2008 IEEE Workshop on Signal Propagation on Interconnects*, 2008, pp. 19–22, 12th IEEE Workshop on Signal Propagation on Interconnects, Avignon, France, May 12-15, 2008.

[46] S. Narayana, G. Rao, R. Adve, T. Sarker, V. Vannicola, M. Wicks, and S. Scott, "Interpolation/extrapolation of frequency domain responses using the Hilbert transform," *IEEE Trans. Microw. Theory Techn.*, vol. 44, no. 10, 1, pp. 1621–1627, 1996.

[47] S. P. Luo and Z. Z. Chen, "Iterative methods for extracting causal time-domain parameters," *IEEE Trans. Microw. Theory Techn.*, vol. 53, no. 3, 1, pp. 969–976, 2005.

[48] B. Young, "Bandwidth and density reduction of tabulated data using causality checking," in *2010 IEEE Electrical Design of Advanced Packaging and Systems Symposium (EDAPS 2010)*, 2010, pp. 1–4.

[49] P. Triverio and S. Grivet-Talocia, "A robust causality verification tool for tabulated frequency data," in *10th IEEE Workshop On Signal Propagation On Interconnects,*

Proceedings, 2006, pp. 65–68, 10th IEEE Workshop on Signal Propagation on Interconnects, Berlin, Germany, May 09–12, 2006.

[50] ——, "On checking causality of bandlimited sampled frequency responses," in *PRIME 2006: 2nd Conference on Ph.D. Research In Microelectronic and Electronics, Proceedings*, Malcovati, P. and Baschirotto, A., Ed., 2006, pp. 501–504, 2nd Conference on Ph.D. Research in MicroElectronics and Electronics, Otranto, Italy, June 12-15, 2006.

[51] ——, "Robust causality characterization via generalized dispersion relations," *IEEE Trans. Adv. Packag.*, vol. 31, no. 3, pp. 579–593, 2008.

[52] R. Mandrekar and M. Swaminathan, "Causality enforcement in transient simulation of passive networks through delay extraction," in *Signal Propagation on Interconnects, Proceedings*, 2005, pp. 25–28, 9th IEEE Workshop on Signal Propagation on Interconnects, Garmisch Partenkirchen, Germany, May 10-13, 2005.

[53] ——, "Delay extraction from frequency domain data for causal macro-modeling of passive networks," in *2005 IEEE INTERNATIONAL SYMPOSIUM ON CIRCUITS AND SYSTEMS (ISCAS), VOLS 1-6, CONFERENCE PROCEEDINGS*, ser. IEEE International Symposium on Circuits and Systems, 2005, pp. 5758–5761, IEEE International Symposium on Circuits and Systems (ISCAS), Kobe, JAPAN, MAY 23-26, 2005.

[54] R. Mandrekar, K. Srinivasan, E. Engin, and M. Swaminathan, "Causal transient simulation of passive networks with fast convolution," in *10th IEEE Workshop*

on Signal Propagation on Interconnects, Proceedings, 2006, pp. 61–64, 10th IEEE Workshop on Signal Propagation on Interconnects, Berlin, Germany, May 09-12, 2006.

[55] S. N. Lalgudi, K. Srinivasan, G. Casinovi, R. Mandrekar, E. Engin, M. Swaminathan, and Y. Kretchmer, "Causal transient simulation of systems characterized by frequency-domain data in a modified nodal analysis framework," in *Electrical Performance of Electronic Packaging*, 2006, pp. 123–126, 15th IEEE Topical Meeting on Electrical Performance of Electronic Packaging, Scottsdale, AZ, Oct 23-25, 2006.

[56] B. S. Xu, X. Y. Zeng, J. He, and D.-H. Han, "Checking causality of interconnects through minimum-phase and all-pass decomposition," in *2006 Conference on High Density Microsystem Design and Packaging and Component Failure Analysis (HDP '06), Proceedings*, 2006, pp. 271–273.

[57] A. Dienstfrey and L. Greengard, "Analytic continuation, singular-value expansions, and Kramers-Kronig analysis," *Inverse Problems*, vol. 17, no. 5, pp. 1307–1320, 2001.

[58] H. A. Aboutaleb, L. L. Barannyk, A. Elshabini, and F. Barlow, "Causality enforcement of DRAM package models using discrete Hilbert transforms," in *2013 IEEE Workshop on Microelectronics and Electron Devices, WMED 2013*, 2013, pp. 21–24.

[59] L. L. Barannyk, H. A. Aboutaleb, A. Elshabini, and F. Barlow, "Causality verification using polynomial periodic continuations," *J. Microelectron. Electron. Packag.*, vol. 11, no. 4, pp. 181–196, 2014.

[60] ——, "Causality Enforcement of High-Speed Interconnects via Periodic Continuations," in *The 47th International Symposium on Microelectronics, IMAPS 2014, October 14-16, 2014*, 2014.

[61] ——, "Spectrally accurate causality enforcement using SVD-based Fourier continuations," *IEEE Trans. Comp. Packag. Manuf. Techn.*, vol. 5, no. 7, pp. 991–1005, 2015.

[62] J. W. Cooley and J. W. Tukey, "An algorithm for machine calculation of complex Fourier series," *Math. Comp.*, vol. 19, no. 90, pp. 297–&, 1965.

[63] B. Gustavsen, "Time delay identification for transmission line modeling," in *Signal Propagation on Interconnects, Proceedings*, 2004, pp. 103–106, 8th IEEE Workshop on Signal Propagation on Interconnects, Heidelberg, GERMANY, MAY 09-12, 2004.

[64] S. N. Lalgudi, E. Engin, G. Casinovi, and M. Swaminathan, "Accurate transient simulation of interconnects characterized by band-limited data with propagation delay enforcement in a modified nodal analysis framework," *IEEE Trans. Electromagn. Compat.*, vol. 50, no. 3, 2, pp. 715–729, 2008.

[65] H. M. Nussenzveig, *Causality and Dispersion Relations*. Academic Press, 1972.

[66] J. C. Hassab and R. Boucher, "Probabilistic Analysis of Time-Delay Extraction by Cepstrum in Stationary Gaussian Noise ," *IEEE Trans Inf Theory*, vol. 22, no. 4, pp. 444–454, 1976.

[67] A. Charest, D. Saraswat, M. Nakhla, R. Achar, and N. Soveiko, "Compact macromodeling of high-speed circuits via delayed rational functions," *IEEE Microw. Compon. Lett.*, vol. 17, no. 12, pp. 828–830, 2007.

[68] L. L. Barannyk, H. H. Tran, L. V. Nguyen, A. Elshabini, and F. Barlow, "Time delay estimation using SVD-based causal Fourier continuations for high speed interconnects," in *2015 IEEE 24th Conference on Electrical Performance of Electronic Packaging and Systems, Oct. 25-28, 2015, in San Jose, California, USA*, 2015, p. accepted.

[69] K. Kurokawa, "Power waves and the scattering matrix," *IEEE Transactions on Microwave Theory and Techniques*, vol. MTT-13, no. 2, March 1965.

[70] C. Mead and L. Conway, *Introduction to VLSI systems.* Addison-Wesley., 1980.

[71] M. Sadiku, *Elements of Electromagnetics.* Oxford University Press, 2007.

[72] M. Kamon, N. Marques, L. Silveira, and W. J.K., "Automatic generation of accurate circuit models," *IEEE Trans. on Components, Packaging, and Manufact. Tech.*, August 1998.

[73] M. Kamon, N. Marques, and W. J.K., " FastPep: a fast parasitic extraction program for complex three-dimensional geometries," in *Proc. of the IEEE/ACM In-*

ternational Conference on Computer-Aided Design, San Jose, CA, November 1997, pp. 456–460.

[74] A. Technologies, "Advance Calibration Techniques for Vector Network Analyzers," 2006.

[75] D. M. Pozar, *Microwave Engineering.* Wiley, 2011.

[76] B. C. Wadell, *Transmission Line Design Handbook: Design Guide for High-Speed Controlled Impedance Circuit Boards.* Norwood: Artech House Inc., 1991.

[77] H. H. Tran, L. L. Barannyk, A. Elshabini, and F. Barlow, "A Study of Differential Signaling: Stable and Accurate Mixed-Mode Conversion and Extraction of Differential S-Parameters," in *2015 IEEE Workshop on Microelectronics and Electron Devices, WMED 2015*, 2015, pp. 24–27.

[78] L. L. Barannyk, H. H. Tran, A. Elshabini, and F. Barlow, "Preservation of causality during conversion from single-ended to mixed-mode s-parameters," *J. Microelectron. Electron. Packag.*, to be submitted.

[79] L. L. Barannyk, H. H. Tran, L. V. Nguyen, A. Elshabini, and F. Barlow, "Delay extraction from frequency domain data using SVD-based causal Fourier continuations," *J. Microelectron. Electron. Packag.*, to be submitted.